ANL-6199
Biology and Medicine
(TID-4500, 15th Ed.)
AEC Research and
Development Report

ARGONNE NATIONAL LABORATORY
9700 South Cass Avenue
Argonne, Illinois

RADIOLOGICAL PHYSICS DIVISION SEMIANNUAL REPORT

January through June, 1960

J. E. Rose, Division Director
L. D. Marinelli, Associate Division Director

August 1960

Preceding Report:
ANL-6104 July through December, 1959

Operated by The University of Chicago
under
Contract W-31-109-eng-38
with the
United States Atomic Energy Commission

DISCLAIMER

TABLE OF CONTENTS

TABLE OF CONTENTS

NONRADIATIVE ENERGY TRANSFER AND THE α/β RATIO IN A FLUORESCENT SOLUTION*

I. B. Berlman

From an analysis of pulse heights produced by α-particles, as a function of the solute concentration, the fraction of the excitation energy, ϵ, which is transferred to 2,5 diphenyloxazole (PPO) dissolved in para-xylene has been determined as $\epsilon = 2.43c/(1 + 2.43c)$, where c is the concentration of the solute in grams/liter.

The α/β ratio in the above solution varies with solute concentration. It is 0.035 at 0.1 gram/liter and 0.072 at 4 grams/liter.

Quenching of the excitation energy by oxygen has been found consistent with static and dynamic quenching of the solvent and dynamic quenching of the solute.

---

*Abstract of a paper which is being submitted to the Journal of Chemical Physics.

PROBABILITY OF IONIZATION IN ENERGY TRANSFER FROM EXCITED ATOMS TO MOLECULES*

Robert L. Platzman**

Abstract

The probability that a molecule is ionized when it acquires excitation energy in excess of its ionization potential in a collision with a metastable helium, neon, or argon atom is deduced for fourteen diatomic and polyatomic molecules from measurements of the total ionization by alpha particles in contaminated noble gases. In every case this ionization efficiency is smaller than unity, and in some it is much smaller. In a few instances the results can be compared with the corresponding probabilities in excitation by absorption of light, and the two ionization efficiencies are found to be equal, within the uncertainties of the data. Some of the implications of these results are discussed.

Transfer of the excitation energy from an excited atom to a second atom by a collision in a gaseous mixture is one of the oldest known[1] and best established[2,3] varieties of collision of the second kind. If the second atom, X, has ionization potential I_x smaller than the excitation energy E_* of the excited atom, A*, the result can be ionization of X:

$$A^* + X \longrightarrow A + X^+ + \epsilon^- \quad . \tag{1}$$

Such collateral ionization is particularly conspicuous if the excited atom is metastable, for then the longer lifetime of A* enables reaction (1) to occur even at low concentrations of the second atomic species. Many examples of process (1) have been studied, particularly with metastable noble-gas atoms. If the reaction is energetically possible (i.e., if $E_* \geq I_x$), the cross section[4,5] is usually large (comparable to the geometrical cross section) because the process is one of exact resonance - that is, appreciable change in the kinetic energies of the atoms themselves is not required. The kinetics of the competition between reaction (1) and processes destroying the metastable atoms in the pure parent gas follow the

---

*To be published in J. phys. radium.

**Fulbright Professor, Faculté des Sciences, Université de Paris, 1959-1960. on leave from Argonne National Laboratory, Argonne, Illinois, U.S.A.

simple law deduced in 1919 by Stern and Volmer [5,6] This collateral ionization plays an important role in many fields, among them electrical discharges in gases[7] and ionization of gases by high-energy particles.[8,9 10]

If X is a molecule, the act of energy transfer need not ionize it, even though $E_* > I_X$. The reason is that there can be formed an excited state of X which, although certainly susceptible to pre-ionization, may also have the possibility of undergoing dissociation (or predissociation) at a competitive rate Large molecules have a second possibility of escaping pre-ionization, namely, internal coversion to a lower electronic state. Thus every molecule will have a certain probability of ionization, η, which will depend upon the excitation energy, E, as well as upon the character of the molecule It is necessary that $\eta = 0$ for $E - I_X < 0$, and expected that $\eta = 1$ for $E - I_X >> I_X$. For $(E - I_X)$ between zero and a few Rydbergs, $\eta(E)$ may lie anywhere between zero and unity, the value depending upon the competition described above.

Direct determination of η has been accomplished in a series of investigations by Weissler and collaborators,[11] by measurement in the vacuum-ultraviolet region of both the absorption of light and the concomitant ionization, in gases at low pressure. The results exhibit remarkable variations between zero and unity and substantiate the assertion above that reorganization of nuclear positions in high electronic states of both diatomic and polyatomic molecules is competitive with pre-ionization. Weissler has termed η the ionization efficiency.

The ionization efficiency η_p, corresponding to excitation by absorption of a photon having energy $h\nu$ need not be equal to the value η_c corresponding to energy transfer in a collision with an excited atom having excitatior energy $E_* = h\nu$ There are at least three possible reasons for a difference:

A. The ionization following photon absorption may be viewed as comprising contributions from two alternative paths, direct ejection of the photoelectron by the electric field of the electromagnetic wave:

$$BC + h\nu \longrightarrow BC^+ + \epsilon^-; \tag{2}$$

and formation of a quasi-stationary excited state followed by subsequent pre-ionization:

$$BC + h\nu \longrightarrow BC^* \tag{3}$$

$$BC^* \longrightarrow BC^+ + \epsilon^- \tag{4a}$$

$$\searrow B + C \tag{4b}$$

(Pre-ionization may occur instead in one of the fragments, following dissociation. This rarer occurrence does not require special discussion.) The observed photoionization efficiency, η_p, will therefore be greater than the intrinsic probability of pre-ionization of the excited state, to an extent dependent upon the relative contribution of (2) and (3). Ionization by collisional energy transfer may likewise occur by the analogous alternatives. However, because the electric field of an excited atom differs from that of an electromagnetic wave, the relative probabilities of (2) and (3) may be different when the energy $E = h\nu$ is transferred in a collision, rather than in an act of photon absorption.

B. In a collision, the nature of the transient excited state (if there are several states of equal energy that combine poorly) may differ from that formed by photon absorption. Thus collisional excitation need not comply with dipole selection-rules. For a given energy-transfer, E, the nature of the excited state of the molecule will vary with other factors; for example, it will depend upon the spin of the original excited atom (Wigner spin-conservation rule[3]).

C. The relative probabilities of pre-ionization and atomic reorganization (processes 4a and 4b) may be affected by the interaction during impact. Two facts should be noted: the duration of a collision ($\sim 10^{-13}$ sec) is of the same order of magnitude as the minimum characteristic times required for pre-ionization and for atomic reorganization; and the cross sections for energy transfer [process (1)], if the excited atom is metastable, are never much greater than geometrical cross sections because the electric field about the metastable atom is not a dipole field (it has a comparatively short range). Among other consequences, the interaction can lead to small energy-exchanges between electronic and nuclear motions.

On the other hand, the value of η_c or η_p will not be affected by subsequent collisions with other atoms or molecules since the time required for processes like (4a) and (4b) is much shorter than the mean interval between encounters at atmospheric pressure or below.

Some values of η_c will now be deduced from experimental data and compared, insofar as is possible, with values of η_p.

The possibility of obtaining η_c stems from the discovery by Jesse[8] that the total ionization in helium, neon, or argon produced by absorption of high-energy atomic particles is extremely sensitive to the presence of small quantities of impurities. If E_* of the noble-gas atom exceeds I_x of the impurity atom or molecule, the ionization in the impure gas is always greater than in the pure gas. This collateral ionization arises mainly (but not exclusively) from reaction (1) with metastable noble-gas atoms. The total ionization is customarily measured by the ratio $W = T_0/N_i$, where T_0 is the initial kinetic energy of the particle and N_i is the (average) total number of ion pairs formed by its complete absorption.[9,10] All of the results to be used here pertain to the case of alpha particles, for which the most accurate data on the Jesse effect are available; but similar behavior is expected with all types of high-energy radiation and has been observed with gamma rays[8] and beta rays.[5] By adding known increments of a known contaminant to the pure gas, the value of W is found to decline progressively and to reach a plateau at contaminant concentration of a few-tenths of one per cent. The diminished value of W in this plateau corresponds to a certain number of collateral ion-pairs (ΔN_i) per particle.

The number of metastable atoms produced by the alpha particle and the secondary electrons which it generates will be unaffected by the presence of the contaminant at concentrations smaller than about one per cent. In the plateau region, where all of the metastable noble-gas atoms have been deactivated by process (1), it is therefore expected that $\Delta N_i = 0$ if $I_x > E_*$, and ΔN_i = constant for each noble gas if $I_x \leq E_*$. If the contaminant is itself a noble gas, this is indeed observed, although not exactly. In fact, for contaminants with I_x smaller than E_*, ΔN_i slowly increases with declining I_x because the free electrons having kinetic energy ϵ in the range $I_x < \epsilon \leq E_0$ (E_0 is the lowest electronic excitation energy of the atoms of the main component) can themselves cause additional ionization. Such electrons are called subexcitation electrons; their contribution to the collateral ionization has already been treated.[12] However, if the contaminant is a molecular gas, ΔN_i is always smaller, and often much smaller, than expected on the basis of the behavior of atomic contaminants. This effect has been explained as arising from an ionization efficiency smaller than unity for energy transfer from a metastable atom to the molecule.[9,10] It is particularly arresting in the studies of the Jesse effect in dilute argon-mixtures by Melton et al.,[13] for here the additives are all polyatomic molecules and are diverse in nature.

The difference in behavior of atomic and molecular contaminants is now exploited to calculate values of η_c. A first approximation is

$$\eta_c = \Delta N_i / \Delta N_i^a \quad , \tag{5}$$

where ΔN_i is the observed increment in ionization for a given molecular contaminant, in the plateau region, and ΔN_i^a is the increment corresponding

to an atomic contaminant of the same ionization potential. This equation takes account of the subexcitation electrons, but only approximately: it disregards the fact that their contribution to ΔN_i includes a range of E-values from E_0 down to I_x and may, therefore, correspond to a mean value of η slightly different from η_c.* Correction for this effect, which is a small one, is deferred to a later time.

In the case of helium and neon as principal gases, values of ΔN_i^a are readily obtained from a curve drawn through the observed ΔN_i for argon, krypton, and xenon as contaminants. This is not possible for argon, with which even xenon has $I_x > E_*$. It is therefore assumed that $\Delta N_i^a(I_x)$ for argon is the same function as for neon (or for helium: the two differ only slightly). This assumption is in harmony with the similar behavior of He, Ne, and A with respect to the energy balance of all primary products of absorption of the alpha particle.[9,10]

The results of the calculation of η_c are presented in Table 1. The value of $\bar{E}_*$ entered for neon and for argon is the average of the excitation energies of the two metastable states; the simple mean is taken because there is no knowledge of the relative populations of these two states following absorption of an alpha particle. In the case of helium, most of the metastable atoms are 2^1S_0, and the appropriate value of $\bar{E}_*$ is close to the energy of that state. References to the specific sources of ΔN_i-values are given in the table.

The ionization efficiencies are found to be smaller than unity in every case. It should be noted that the compounds are even-electron molecules composed, with one exception, of hydrogen and elements of the first row of the periodic system.

Values of η_p from the work of Weissler and collaborators are also presented in Table 1. For the few cases in which both η_p and η_c are available at the same excitation energy ($\bar{\lambda} = hc/\bar{E}_*$), the two are

---

*Indeed, η_ϵ for excitation by electron impact is a third type of ionization efficiency. For very fast electrons (kinetic energy greater than about 1 kev) $\eta_\epsilon = \eta_p$ for the same energy transfer because of the well-known equivalence of light absorption and energy transfer from swiftly-moving charged particles in glancing collisions. For slow electrons, however, it is entirely possible that the strong interaction between molecule and electron (which permits spin reversal, among other effects) leads to a value of η_ϵ different from both η_p and η_c. For this reason, no specific conclusion can be drawn on the implications of the results of this paper for the "threshold" law for ionization of molecules by electron impact although the fact that they have an important bearing is obvious.

approximately equal. Although the basis for inferring this equality is slender, and is qualified by uncertainties in both η_p and η_c, it is nevertheless significant. Thus η_c for N_2 and for CO_2 with He* is slightly but definitely smaller than unity; with A*, η_c of ethylene is much smaller than η_c of acetylene; and both statements apply equally well to the corresponding values of η_p.

Table 1

Values of the ionization efficiency for energy transfer in collision with a metastable noble-gas atom (η_c) and for absorption of light (η_p).

	He* $\overline{E}_* = 20.57$ ev $\overline{\lambda} = 603$ Å		Ne* $\overline{E}_* = 16.67$ ev $\overline{\lambda} = 744$ Å		A* $\overline{E}_* = 11.64$ ev $\overline{\lambda} = 1065$ Å	
	η_c	η_p	η_c	η_p	η_c	η_p
H_2	0.92[5]		0.83[5]	0.85[25]	0	0
N_2	0.89[5]	0.90[11,17]		0.75[11,17]	0	0
O_2	0.9[14]	0.93[11,17]		0.60[11,17]	0	0
CO_2	0.87[5]	0.80[11]		0.90[11]	0	0
CH_4	0.83[15]				0	0
C_3H_8					0.30[13]	
nC_4H_{10}					0.36[13]	
C_2H_4	0.73[5]			0.85[18]	0.26[5,13]	0.3[18]
C_2H_2	0.79[16]		0.77[16]	0.80[18]	0.76[13,16]	0.8[18]
C_6H_6					0.40[13,16]	
$(CH_3)C_6H_5$					0.39[13]	
C_2H_5OH					0.30[13,19]	
$(CH_3)_2CO$					0.18[13]	
CH_3I					0.52[13]	

(Note: the value $\eta = 0$ is entered for all cases in which $I_x > \overline{E}_*$. Although W of such gas mixtures often indicates collateral ionization, the augmentation in ionization is smaller and requires a greater concentration of additive than in the true Jesse effect; it is obviously not caused by reaction (1) with metastable atoms.)

It may be mentioned that experiments on W in contaminated noble gases are a potentially rich source of data on η_c. If, moreover, the suggestion that $\eta_p = \eta_c$ should be confirmed by further investigation, W-measurements will provide values of the ionization efficiency more easily and perhaps more accurately than contemporary optical measurements can - although, of course, only at a few restricted values of E_*. (The interesting structure of the $\eta(E)$ spectrum[11] can only be determined optically, at present.) Information on η_c may also be obtainable from certain studies in gaseous electronics - for example, from measurement of the

influence of contaminants on the breakdown potential and ionization coefficient for noble gases (Penning effect). Some pertinent data are indeed already available.[20] It will be of particular interest to discover whether η_c with helium atoms in the 2^3S state is the same as that with atoms in the 2^1S state.

Knowledge of $\eta(E)$ is obviously an essential element for the fundamental understanding of the nature of highly-excited electronic states of molecules. This is emphasized by the fact that the broad range of E in which $E > I$ and $\eta < 1$ is just that domain in which the major fraction of the total oscillator-strength is concentrated.

Because of the same fact, much of the excitation (as distinguished from ionization) resulting from absorption of high-energy radiation will lie at values of the excitation energy greater than the ionization potential. Since the ionization potentials of molecules are considerably larger than dissociation energies (D) of chemical bonds, the chemical activation in such excited states is very great indeed. In small molecules, which usually dissociate very soon after being excited, the excess energy (E - D) will appear as electronic excitation and as energy of atomic motion (translation, vibration, rotation), and will, in general, enhance the chemical reactivity of the fragments. Formation of such activated fragments, therefore, is not rare, as has heretofore been supposed, but on the contrary occurs in an appreciable, and perhaps in a major, fraction of excitation acts.

Applications of information on η are numerous and encompass diverse branches of physics and chemistry. For example, processes like those discussed here are common in the operation of Geiger counters, ionization chambers, and other devices for the detection and measurement of nuclear particles; in various types of electrical discharge in gases; and in the mechanisms of radiation chemistry. The importance of η_ϵ for the "threshold" law of ionization of molecules by electron impact has already been mentioned. Among theoretical consequences is the modification required in the interpretation of the optical data obtainable from ionization measurements. From the energy dependence of the "primary" ionization of molecules by high-energy (Mev) electrons[21] or of the ionization cross section with moderate-energy (kev) electrons[22] the quantity

$$M_i^2 = R\int_I^{\infty} \eta_p(E)\, E^{-1} df(E) \qquad (6)$$

can be determined. Here df/dE is the differential oscillator-strength and is proportional to the absorption coefficient for light of wavelengths $\lambda = hc/E$, and R is the Rydberg energy. The necessity of the factor $\eta_p(E)$ was not recognized previously; that is, it was thought that the ionization cross sections yield the quantity

$$M_I^2 = R\int_I^\infty E^{-1}df(E) \quad . \tag{7}$$

The two parameters are equal for atoms (assuming that radiation cannot compete favorably with pre-ionization) but are unequal for molecules. A direct and useful determination of the mean ionization-efficiency over the entire ionization-continuum is practicable by combining measurement of M_i^2 (energy dependence of ionization cross section) with that of M_I^2 (integration of equation (7), using light-absorption or electron-scattering data):

$$\bar{\eta}_p = M_i^2/M_I^2 \quad . \tag{8}$$

General conclusions which can be drawn from Table 1 and the foregoing discussion are as follows:

1. The validity of the explanation[9] of the seemingly erratic differences in W of various dilute argon-mixtures[13] on the basis that $\eta_c < 1$ is strongly supported.

2. The common, although usually implicit, assumption that energy transfer in excess of its ionization potential to a molecule must necessarily result in ionization is incorrect.

3. Many molecules of diverse nature (probably most and perhaps all molecules) possess excited electronic states lying within a few Rydbergs above their ionization potential in which disposal of the excitation energy by dissociation or internal conversion can compete favorably with pre-ionization.

4. Theories of the photoionization of molecules (in the energy domain under discussion) which are based upon matrix elements between ground state and "ion + free-electron" states are at best incomplete. It is feasible, and will be an important initial study, to obtain more detailed information on the spectrum of ionization efficiencies and to develop a satisfactory theory for the case of molecular hydrogen, for which spectroscopic information on pre-ionization is also available.[23,24]

5. There is a clear suggestion (although hardly more than that because of paucity and inaccuracy of presently-available data) that $\eta_p = \eta_c$, and, therefore, that the possible sources of a difference between them, which were discussed above, are inoperative. This conjecture, if confirmed, would have many

consequences. And if, in addition, detailed analysis of the character of the field about a metastable atom should prove that, as argued above, it does indeed differ essentially from that of a free wave, insofar as determining the probabilities of direct photoionization (process 2) and photoexcitation (process 3) is concerned, it would be established that the former is much smaller than the latter, and that the measured ionization efficiency is equal to the intrinsic probability of pre-ionization of the excited state. This conclusion would necessitate revision of many current ideas concerning the nature of ionization by light absorption, by electron impact, and by collisions of the second kind with excited atoms.

References

1. G. Cario and J. Franck, Z. Physik 17 202 (1923).

2. For the older literature, see E. J. B. Willey, "Collisions of the Second Kind," London: Edward Arnold and Co., 1937.

3. For the later literature, see H. S. W. Massey and E. H. S. Burhop, "Electronic and Ionic Impact Phenomena," Oxford: Clarendon Press, 1952.

4. M. A. Biondi, Phys. Rev. 88 660 (1952).

5. W. P. Jesse and J. Sadauskis, Phys. Rev. 100 1755 (1955).

6. O. Stern and M. Volmer, Physik. Z. 20 183 (1919).

7. M. J. Druyvesteyn and F. M. Penning, Revs. Mod. Phys. 12 87 (1940) (cf. Section 12).

8. W. P. Jesse and J. Sadauskis, Phys. Rev. 88 417 (1952).

9. For a review which emphasizes the features of W pertinent to this paper, see R. L. Platzman, Chapter 2 in "Radiation Biology and Medicine," W. D. Claus, ed. Reading, Mass: Addison-Wesley Publishing Co., 1958; and also ref. 10 below.

10. R. L. Platzman, in "Proceedings of the Conference on Penetration of Charged Particles in Matter." National Research Council Publication 752, Washington, D. C., 1960.

11. G. L. Weissler, in Handbuch der Physik, Berlin: Springer-Verlag, 1956. Vol. 21, p. 318.

12. R. L. Platzman, Radiation Research 2 1 (1955).

13. C. E. Melton, G. S. Hurst, and T. E. Bortner; Phys. Rev. 96 643 (1954).

14. W. Haeberli, P. Huber, and E. Baldinger, Helv. Phys. Acta 26 145 (1953).

15. T. E. Bortner and G. S. Hurst Phys. Rev. 93 1236 (1954).

16. H. J. Moe, T. E. Bortner, and G. S. Hurst, J. Phys. Chem. 61 422 (1957).

17. N. Wainfan, W. C. Walker, and G. L. Weissler, J. Appl. Phys. 24 1318 (1953).

18. W. C. Walker and G. L. Weissler, J. Chem. Phys. 23 1547 (1955).

19. G. Bertolini, M. Bettoni, and A. Bisi, Nuovo Cimento 11 458 (1954).

20. B. Klarfeld, Z. Physik 78 111 (1932).

21. U. Fano, Phys. Rev. 95 1198 (1954).

22. W. F. Miller and R. L. Platzman, Proc. Phys. Soc. A70 299 (1957).

23. H. Beutler and H. O. Jünger, Z. Physik 100 80 (1936).

24. H. Beutler and H. O. Jünger, Z. Physk 101 285 (1936).

25. N. Wainfan, W. C. Walker, and G. L. Weissler, Phys. Rev. 99 542 (1955).

MICROSCOPIC METABOLISM OF Ra^{226} IN CANINE BONE. PART II

R. E. Rowland

A study has been made of the distribution of radium in bones of a dog at two widely different times in order to estimate the loss of activity from bone by processes other than direct resorption. A 15-kg mongrel dog, one or two years of age, was given equal intravenous injections of Ra^{226} Cl_2 once a week for a period of eight weeks. Four weeks after the last injection the right humerus and radius-ulna were removed by amputation. The dog was sacrificed 353 days later, and the remaining bones were prepared for analysis.

The preliminary data obtained from the bones taken at the amputation have been previously described.(1) In this report a comparison will be made between the radium concentrations in the terminal bone samples and the amputation samples.

For the sake of completeness, the findings in the bones obtained at amputation are summarized as follows:

(1) The radium-to-calcium ratio measured in bone which was forming during the injection period, i.e., hot spots, was found to be identical (within 15%) to the average radium-to-calcium ratio existing in the blood plasma during that time. This is interpreted as indicating that there is no discrimination against radium in the transfer from blood to bone.

(2) The diffuse uptake of radium, which can be interpreted as an augmentation rate when compared to the radium concentration in the blood, was found to yield values very similar to the augmentation rate measured with Ca^{45}.(2) This is interpreted as indicating that radium is also a valid tracer for calcium in this process.

Gross Retention Measurements

The right radius, obtained at amputation, had been stored in ethyl alcohol until the opposite radius was obtained at sacrifice. After weighing (terminal radius 10.6 g, amputated radius 10.2 g), each bone was sealed in a glass vial and the radium content measured one month later by counting the gamma rays from RaC' with a NaI(Tl) crystal and multichannel analyzer. The ratio of the activity in the terminal sample to that of the amputated sample was found to be 0.77; the predicted ratio, based on the power function description of the retention of radium in the entire skeleton

of the beagle,[3] i.e., $R = 0.79t^{-0.20}$, was 0.66. For this calculation, the total retention at sacrifice and at amputation was calculated as the sum of eight individual retentions, each for a different time, t, corresponding to the time between each injection and sacrifice or amputation. However, the data from which this power function was derived show wide variations over this time interval,[3] so that this difference may not be significant.

Hot Spot Intensities

The primary purpose of this study was to measure by autoradiography the specific activity of the hot spots at two different times in the same animal in order to determine whether any loss of activity from these regions could be detected. The multi-injection technique was employed to provide bands of uniform activity in growing bone over which satisfactory alpha-track counts could be made.

The hot spots in two of the bones obtained at amputation, the humerus and the ulna, had previously been evaluated, and at sacrifice the opposite humerus and ulna, and also the tibia and femur, were analyzed. The maximum hot spot activity found in each bone is recorded in Table 2.

Table 2

Hotspot and diffuse levels per mg of bone

Bone	Hotspots			Diffuse			Hotspot-to-diffuse ratios	
	Terminal, $\mu\mu c/mg$	Amputated, $\mu\mu c/mg$	Ratio: $\frac{\text{Terminal}}{\text{Amputated}}$	Terminal, $\mu\mu c/mg$	Amputated, $\mu\mu c/mg$	Ratio: $\frac{\text{Terminal}}{\text{Amputated}}$	Terminal	Amputated
Humerus	242	366	0.66	11.5 ± 1.0	15.3 ± 1.5	0.75 ± 0.15	21	24
Ulna	230	350	0.66	8.1 ± 1.0	10.8 ± 1.0	0.75 ± 0.15	28	32
Femur	237	-	-	12.2 ± 1.0	-	-	19	-
Tibia	245	-	-	10.8 ± 1.0	-	-	23	-

Maximum hot spots have been employed in this study in the belief that most hot spots have the same specific activity but that some apparent differences result from the spreading of the alpha tracks on the autoradiograph over an area larger than the one from which they originate in the section. This spreading is the result of imperfect contact between the section and the emulsion. In uniformly labeled areas, this phenomenon is of little consequence, for the cross fire of alpha particles compensates outward losses at one point by the inward spreading from adjacent areas.

However, the area over which we count tracks is normally a square 80 microns on a side, and since new bone formation averages about 10 microns a week, the eight-week injection period produced hot spot bands of about the same width as our counting area. It is evident, therefore, that with a track length of the order of 30 microns spreading losses can be severe. To overcome this difficulty, the widest bands were searched for and counted, and by following this criteria in both sets of bone, the effect could be minimized. At least 100 hot spots were counted from each bone.

Table 2 shows clearly that a loss of activity has taken place from the hot spots over the one-year period between amputation and sacrifice, and that the ratio of terminal activity to activity at the time of amputation is remarkably close to the ratio predicted by the power function retention formula, namely 0.66. It is significant that the maximum activity found in each of the four bones analyzed at sacrifice is essentially constant, indicating that the loss is taking place in all of these bones at the same rate.

Diffuse Levels

The diffuse radium levels measured in several bones are also listed in Table 2. In the two bones in which a comparison can be made at one month and a year later, a decrease in the diffuse activity is evident. However, it is apparent that variations in the diffuse level among bones are greater in magnitude than the relative loss in activity over the one-year period.

The diffuse values listed in this table were all taken from the same type of bone, namely, bone characterized by secondary haversian systems. Furthermore, the comparison between amputation and terminal diffuse levels was made from bone sections cut from identical locations in the pair of bones.

During this investigation of diffuse levels, it was found that the radon retention of embedded and sectioned bone slices varied with the relative humidity. Sections kept under very dry conditions and exposed once a week for 17 hours over a two-month period showed a continual increase in the number of alpha tracks per unit area. This increase was reversible, and could be quickly returned to the original level by soaking the bone sections in water for several hours.

To minimize the consequences of this variability in radon retention, all of the values listed in Table 2 for humerus and ulna levels, hot spots as well as diffuse, were obtained as follows: anatomically matched pairs of sections, one from the terminal bone and the other from the amputated bone, were mounted together and a long series of autoradiographic exposures made under various conditions. The levels listed in the table were

those found after the bone sections had been water soaked or stored in an atmosphere of high relative humidity. In general, with dry storage and subsequent increased radon retention, while the total number of alpha tracks per unit area increased in each subsequent autoradiograph, the ratio between the number of alpha tracks over specific areas of the two sections stayed relatively constant. The Ra^{226} levels in Table 2 are calculated on the basis of 35% radon retention in the sections.

Discussion

It is evident that the hot spots as well as the diffuse distributions in this dog contained less radium at time of sacrifice than at the time of amputation. Over this period of one year, we would expect the total body burden of radium to decrease by a factor of 0.66, and this value is just that observed for the loss of activity from the hot spots, with, however, an uncertainty of at least 10%. The diffuse level during this interval has dropped to 0.75 of its original value, with an uncertainty of about 20% in this ratio.

It should be pointed out that under our experimental conditions, a larger loss is to be expected from the hot spots than from the diffuse distribution. Three days after the final radium injection, the blood specific activity is less than the specific activity of the hot spots and continues to fall rapidly, with the consequence that any exchange between new bone mineral and blood will lower the specific activity of these regions. Even the process of secondary mineralization, by which mineral is added to existing new bone, will result in a decrease in the net specific activity of the hot spots.

On the other hand, at the time of amputation, the diffuse specific activity is lower than the blood specific activity and thus should still be increasing in magnitude. About two and a half months after the amputation, the specific activity of the blood falls below the diffuse level, and from this time until sacrifice the exchange processes will be expected to lower the diffuse level. Thus, the diffuse distribution has a shorter time interval over which it may be expected to lose activity; this, plus the fact that the diffuse level is always closer in magnitude to the blood specific activity than the hot spots, results in less apparent loss from the diffuse distribution, even if the mechanisms responsible for the loss are the same in each location.

It must be kept in mind that, as in any study employing a radioactive isotope as a tracer, the dose delivered to the bone may be significantly changing the metabolism of the bone. Thus our results apply strictly to the behavior of radium in hot spots which received a terminal radiation dose of 160 rads per day to the osteocytes, or 80 rads per day

to the adjacent 10-micron thick layer of soft tissues, and to the diffuse distribution where the dose delivered was 1/30th of the hot spot dose. Since, however, the magnitude of the uptake of the diffuse distribution of radium is in essential agreement with the rate of loss of activity from both the hot spots and the diffuse distribution, it may well be that the results obtained from this study have not been significantly altered by these dose rates. This, in turn, implies that these processes may be physical and chemical in nature, rather than metabolic.

Conclusions

It has been clearly demonstrated that a loss of radium occurs from both hot spots and the diffuse distribution in canine bone at rates not greatly dissimilar. These losses, which take place by a mechanism we call long-term exchange, are in substantial agreement with the measured loss of Ca^{45} from the diffuse component, as previously reported by Marshall.[2] These findings, therefore, provide further evidence that in the long-term exchange process in canine bone, both radium and calcium behave with remarkable similarity.

Since the measured fractional loss from both hot spots and the diffuse is close to that prevailing in the entire skeleton, it would appear that within the observational period, loss of activity by resorption did not play a dominant role in the removal of radium from the adult dog.

We are indebted to Dr. Robert Flynn of the Division of Biology and Medicine for performing the amputation on this dog and to Durwood Banister for the injecting and blood sampling.

References

1. R. E. Rowland and J. H. Marshall. Microscopic Metabolism of Ra^{226} in Canine Bone. Radiological Physics Division Seminannual Report, ANL-5967 (May 1959).pp. 58-66.

2. J. H. Marshall, R. E. Rowland and J. Jowsey. Microscopic Metabolism of Calcium in Bone. V. The Paradox of Diffuse Activity and Long-Term Exchange. Radiation Research 10, 258-270 (1959).

3. M. A. Van Dilla, B. J. Stover, R. L. Floyd, D. R. Atherton, and D. H. Taysum. Radium (Ra^{226}) and Radon (Rn^{222}) Metabolism in Dogs. Radiation Research 8 417-437 (1958).

POINT-SOURCE BETA IRRADIATION OF BONE

J. Jowsey* and R. E. Rowland

The carcinogenic effects of irradiation of bone are well known; internal emitters, such as bone-deposited radioactive isotopes, and external sources, such as x rays or gamma rays, have been shown to be capable of inducing tumors in bone. Nevertheless, neither the location of the cells within bone which become neoplastic under the influence of such irradiations nor the actual dose to these cells which is required to produce the neoplastic change is known. Point-source beta irradiation of bone was, therefore, tested to determine whether a high dose to a small volume of bone would result in the induction of bone tumors within the irradiated volume.

A small peg of Sr^{90}-Y^{90} was used as the irradiation source. The site chosen to be irradiated was the tibial diaphysis and metaphysis of the adult rabbit.

Methods

Sr^{90} was precipitated as the oxalate from a strontium chloride solution; the precipitate was ashed at 600°C to form the carbonate and mixed with Scotchcast. This mixture was poured into holes drilled in paraffin wax with a drill that was later used to drill the holes in the bones of the rabbits. The mixture was left to harden for 24 hours and the wax removed with xylene, leaving cylindrical pegs approximately 1 mm in diameter and 1 mm in length. After waiting for the Y^{90} to attain equilibrium, the activity in each peg was measured with a thin end-window counter calibrated with an aliquot from the original solution. To eliminate partially the complications introduced by the source thickness, the Sr^{90} pegs and the calibration aliquot were compared by counting each through 690 mg/cm^2 of glass. Even so, there is probably a 20% uncertainty in the absolute values placed on the pegs.

The pegs were placed in the bone under Nembutal and ether anaesthesia; an incision was made longitudinally over the medial side of the tibia in the mid-diaphysis or over the anterior tuberosity, one to three holes drilled in the bone, and the pegs inserted. The hole space left above the tightly fitting peg was then filled with a mixture of bone wax and ashed bone,

*The work described here was performed between August 1956 and August 1958, while Dr. J. Jowsey was a Resident Research Associate with the Radiological Physics Division.

and the incision was closed. The legs of the rabbits were subsequently x-rayed at intervals thereafter, with the intention of sacrificing the animals at the first appearance of any bone abnormality associated with the pegs. A total of ten rabbits which survived for at least one month after the operation were subsequently followed to death or were sacrificed when bone changes were found.

Following the death of the animals their tibias were removed, fixed in neutralized formalin, and sawed into pieces that included about 1 cm of bone on either side of the peg holes. The bones destined for microradiography were embedded in methyl methacrylate and subsequently cut with an 800-micron thick saw into sections 100 to 150 microns thick. Other pieces of bone were decalcified and used for histological study.

Results

Three of the ten rabbits lived to show gross bony changes; (See Table 3). Of the other animals, two fractured their tibias across the peg holes and four developed pneumonia. In the seven rabbits that died before abnormalities could be seen by x ray, the microradiographs showed a completely normal bone structure except for two interesting features, probably associated with radiation from the pegs. Periosteal and endosteal new bone that formed as a result of drilling the hole grew around the radioactive peg but not right up to it, leaving a shallow, crater-like depression a fraction of a millimeter to several millimeters in diameter around the peg, the floor of this depression being the old periosteal or endosteal bone surface. In no instance did the new bone reach the radioactive peg, and in some the appearance of the new periosteal bone suggested death of the cells in the bone nearest the peg since there were no lacunae visible. The control animals (nonradioactive pegs) showed new bone forming all around the peg and pushing it out of the bone (Fig. 1).

There was no resorption around the inert control peg. The resorption of periosteal bone around the radioactive pegs, which increased in amount with time, eventually involved the new periosteal bone in the animal that lived 15 months postoperatively. This resorption always took place a little distance ($\sim$1 mm) from the peg itself.

The bone studied histologically showed extensive cell death in osteocytes, blood vessels and bone marrow adjacent to the peg. The demarcation between empty lacunae and areas with nuclei in the lacunae was surprisingly sharp (Fig. 2, a and b). In the longitudinal sections from rabbit No. 4 the bone between the two distal pegs in the right tibia was necrotic as was endosteal bone on the other side of cortex (See Fig. 3). Adjacent to the areas which contained the empty lacunae, dense rounded nuclei were visible in the lacunae, perhaps representing a phase before cell death.

Table 3

Rabbit No.	Days to death	Cause of death	Pegs		Examination	Findings
			Location	Activity, μc		
3	32	Pneumonia	RTD*	5.0	Microradiographic	No abnormality
			RTD	5.1	"	"
			RTD	5.1	"	"
			LTD	5.3	"	"
11	92	Pneumonia	RTD	7.3	Histological	Cross sections show cell death to a distance of 1.5 mm on either side of the peg. Formation of dense acellular fibrous tissue in marrow cavity adjacent to peg
			RTM	7.4	"	Cross sections show cell death to a distance of 1.9 mm on either side of peg. Three quarters of marrow has a very poor cell population Fibrous tissue in marrow cavity and endosteal marrow spaces adjacent to peg.
9	113	Pneumonia	RTD	9.1	Microradiographic	No abnormality
			RTM	9.2	"	"
			LTD	4.4	"	"
10	247	Sacrificed after vertebral fracture	RTD	9.4	"	"
			RTM	9.5	"	"
			LTD	4.4	"	"
4	257	Sacrificed after tibial fracture	RTD	5.0	"	"
			RTD	5.2	"	"
			RTD	5.5	Histological	Longitudinal sections show extensive cell death. Vessels empty of cells or else contain nuclear debris. New periosteal bone around peg has empty lacunae in area nearest peg. Marrow largely necrotic. (See Figure 3)
			LTD	5.2	Microradiographic	No abnormality
6	292	Pneumonia	RTD	2.1	"	"
			RTD	2.3	"	"
			RTD	2.2	"	"
2	369	Sacrificed after tibial fracture	RTD	4.5	"	"
			RTD	4.5	"	"
			RTD	4.3	"	"
			LTD	4.2	"	"
			LTD	0	"	"
7	415	Sacrificed with bony changes	RTD	12.1		Fracture through peg area. Not studied
			LTD	6.1	"	Extensive periosteal resorption and endosteal new bone formation apparent. A thickened cortex in gross x ray
12	413	Sacrificed, osteogenic sarcoma	RTD	7.3	"	*Osteogenic sarcoma, gross* (Figure 6)
			RTM	7.2	"	Plugged canals
			LTD	3.1	"	No change
			LTM	3.1	"	Plugged canals (Figure 7)
8	442	Sacrificed with bony changes	RTD	11.8	"	Abnormal bone formation in the marrow cavity. Osteogenic sarcoma? (Figures 8 and 9).
			LTD	6.2	"	No change

*Location code R - Right, L - Left T - Tibia, D - Diaphysis M - Metaphysis

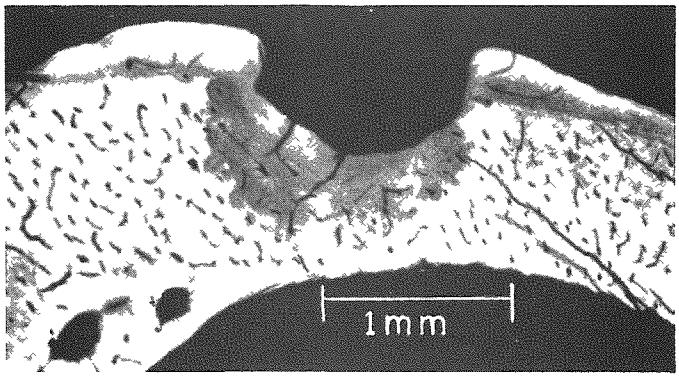

Fig. 1. A microradiograph of a bone section from the tibial diaphysis of rabbit No. 2. New bone is forming around the hole which had contained a nonradioactive peg.

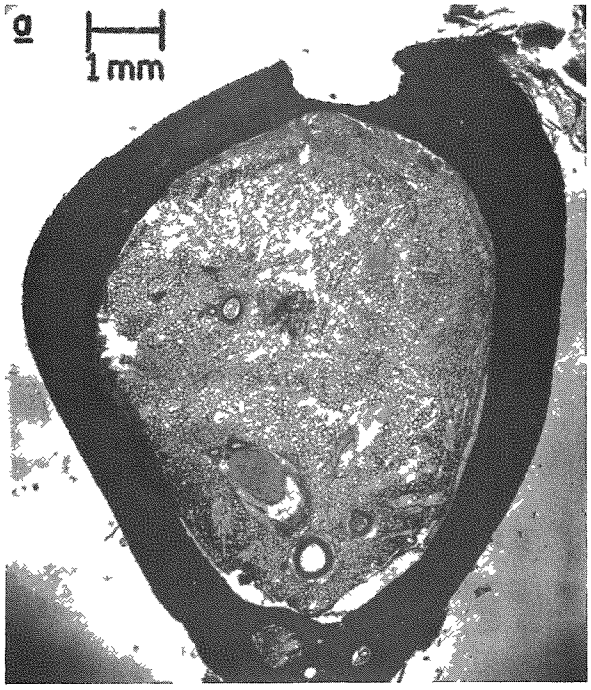

Fig. 2 (a). A histological cross section from the right tibial diaphysis of rabbit No. 11. Stained with haematoxylin and eosin. Beneath the peg-hole is extensive fibrous tissue formation.

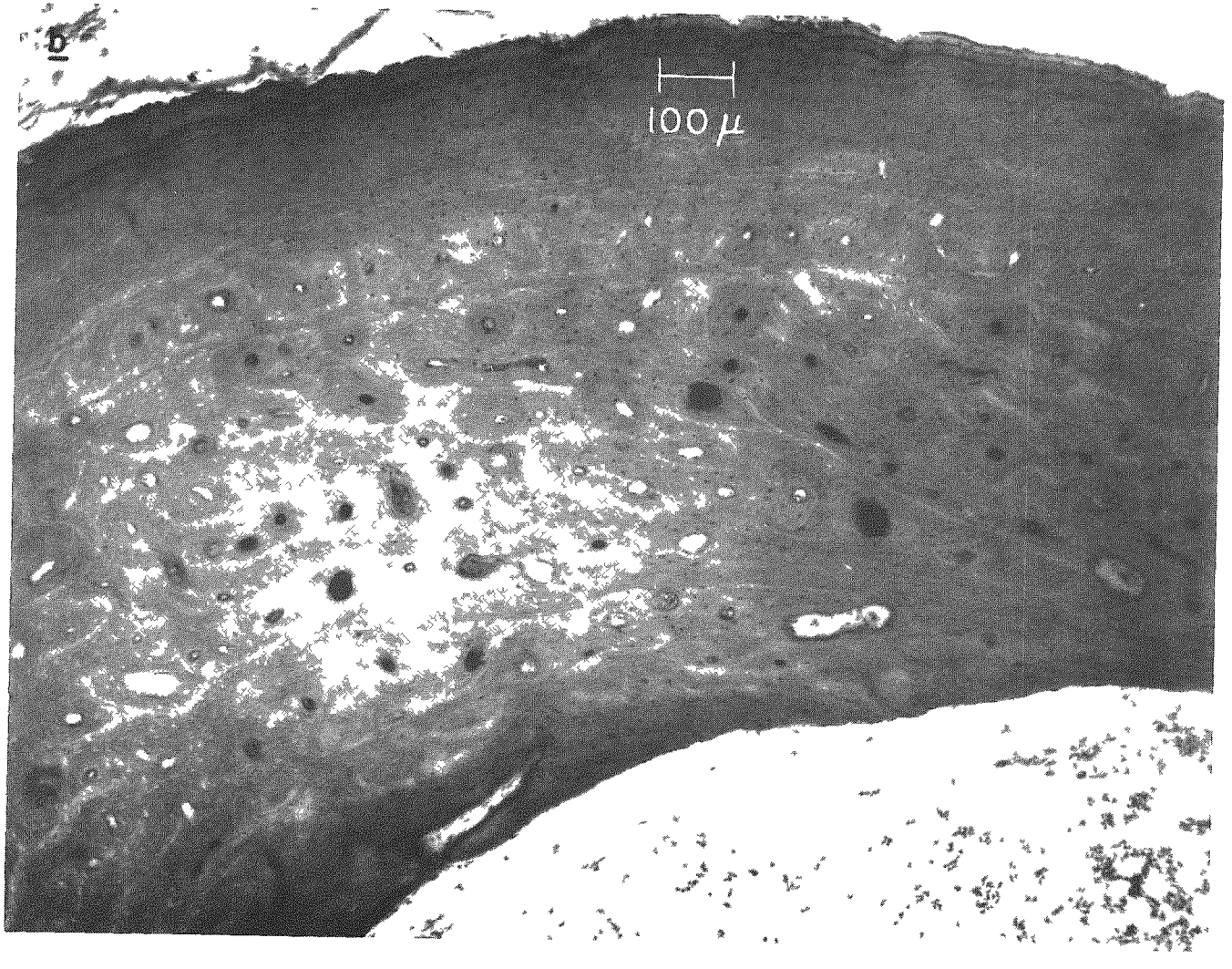

Fig. 2 (b). A detail from (a) showing the sharp demarcation between dead and living osteocytes and lack of cells in the blood vessels.

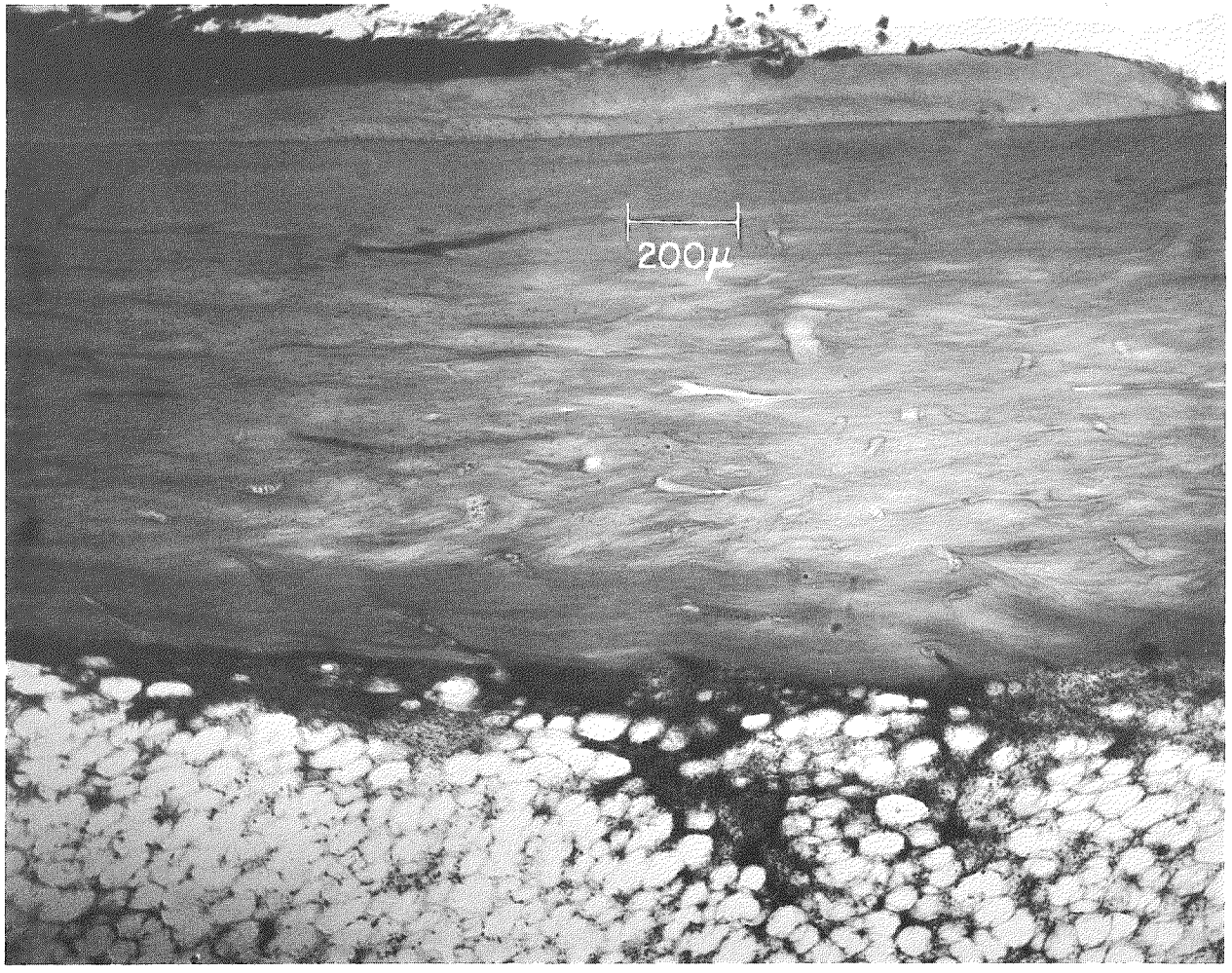

Fig. 3. A histological section cut longitudinally through the right tibial diaphysis of rabbit No. 4, and stained with haematoxylin and eosin. There is cell death in the new periosteal bone nearest the peg hole which is to the right of the section. There is extensive cell death both of the osteocytes and in the haversian canals. The soft tissue appearance is complicated by a fracture that occurred a day before the death of the animal.

Apart from cell death the histological preparations showed extensive fibrous tissue in the marrow cavity and in the endosteal marrow spaces near the pegs (Fig. 4).

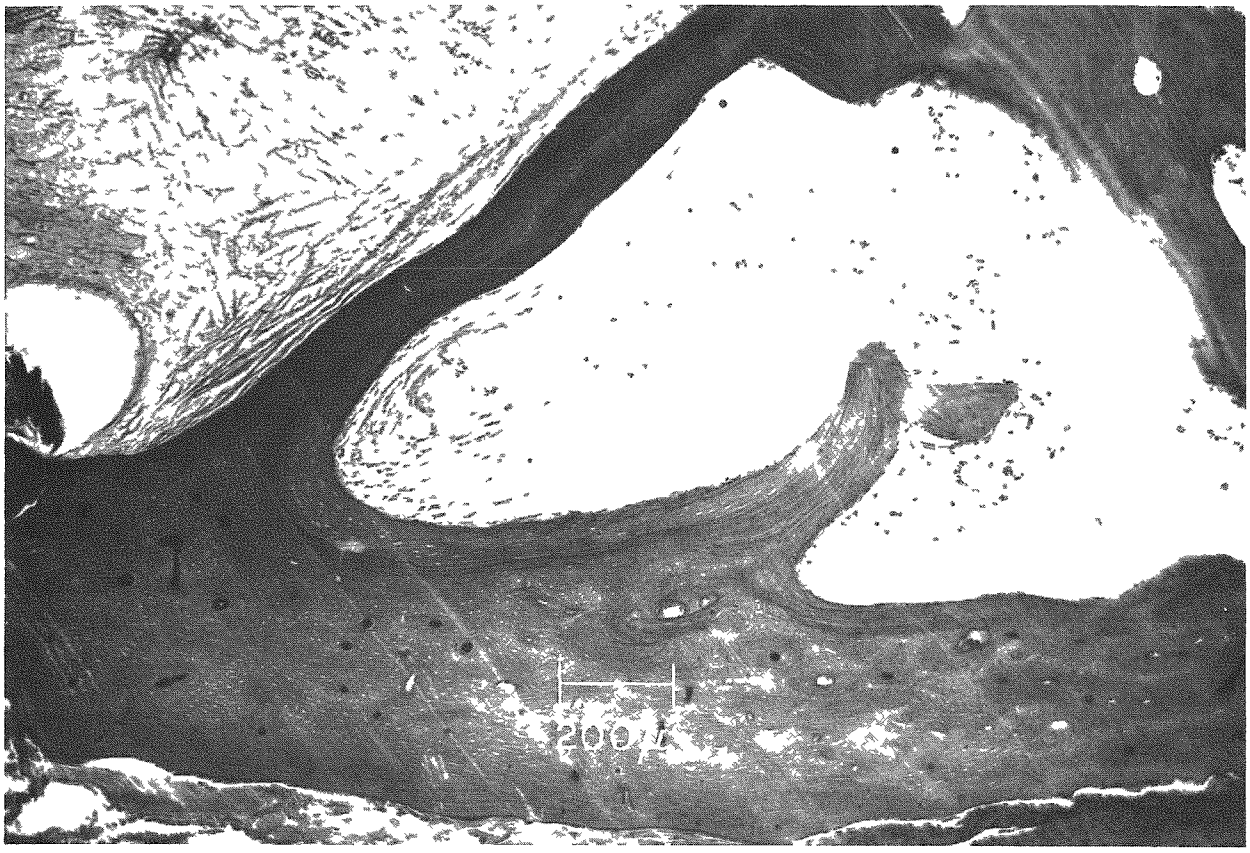

Fig. 4. A histological cross section from the right tibial metaphysis of rabbit No. 11 stained with haematoxylin and eosin. Extensive fibrous tissue, containing few cells, appears near the peg hole which is just visible at the lower left. The bone surrounding the endosteal marrow spaces is largely necrotic.

The three rabbits that lived at least 14 months postoperatively all showed bony abnormalities in the x rays which could be correlated with the microradiographic changes in the sections:

Rabbit No. 7 survived 415 days. The x rays showed thickening of the cortex in the area around the 6.1-μc peg, which was the result of extensive endosteal bone formation, but it is uncertain whether this is a consequence of the radiation. Periosteal resorption near this peg is illustrated in Fig. 5; some of these resorption cavities contained abnormal tissue similar to the material in plugged haversian canals.

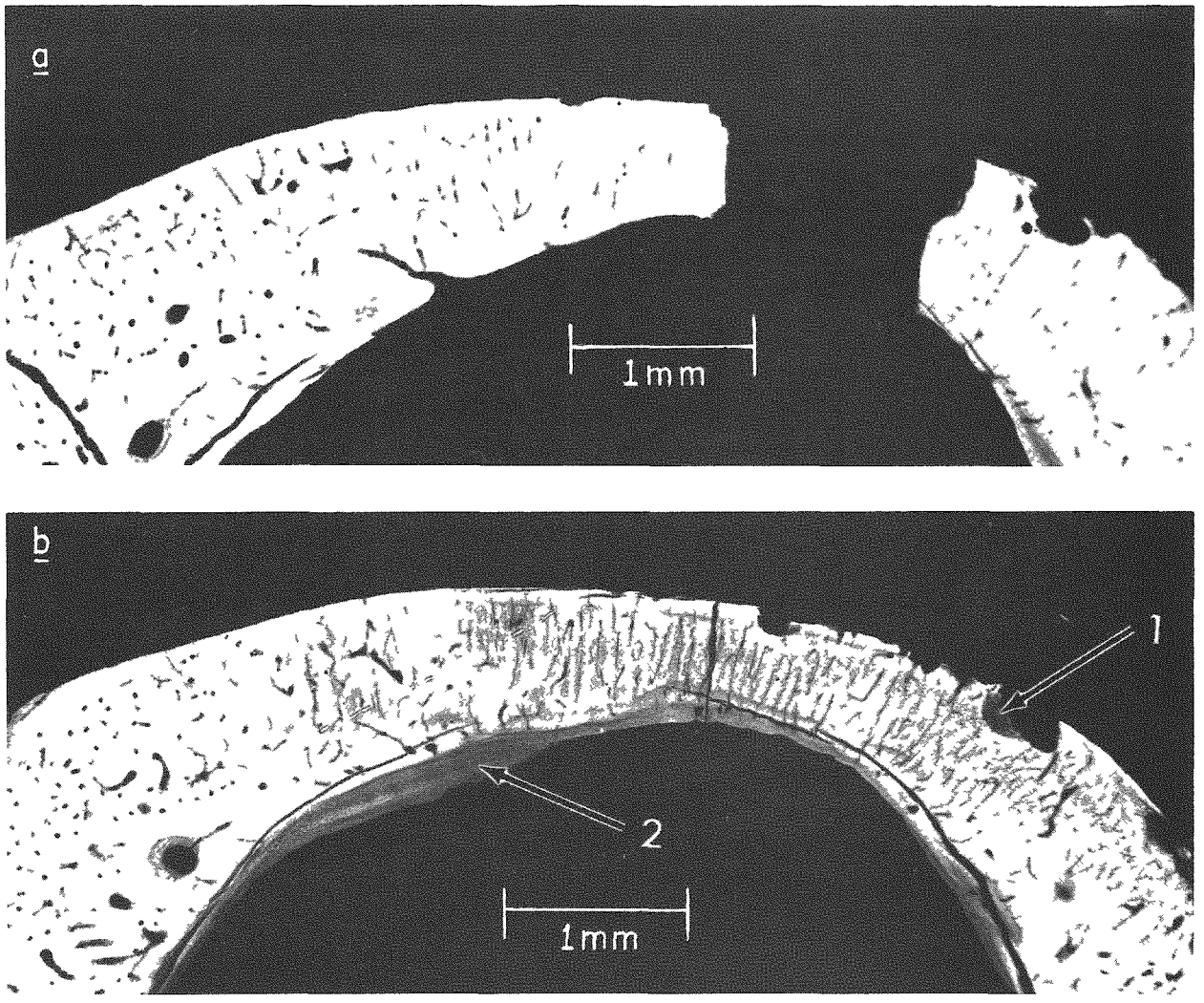

Fig. 5. A pair of microradiographs of bone sections from the left tibial diaphysis of rabbit No. 7. Section (a) shows the peg hole, with some adjacent periosteal resorption. Section (b), which was 1600μ away from (a), shows increased resorption (1) and new bone formation endosteally (2).

Rabbit No. 12 survived 413 days. The x rays showed changes around three of the pegs, the most striking of which is the advanced osteogenic sarcoma (x-ray diagnosis) illustrated in Fig. 6. Plugged haversian canals were found adjacent to the two pegs in metaphyseal bone; they often were observed in osteons of unusually low density (See Fig. 7). More of the plugs were found near the 3.1 - μc peg than around the 7.2 - μc peg.

Fig. 6. A contact print of the x ray of the right tibia of rabbit No. 12, showing an advanced osteogenic sarcoma.

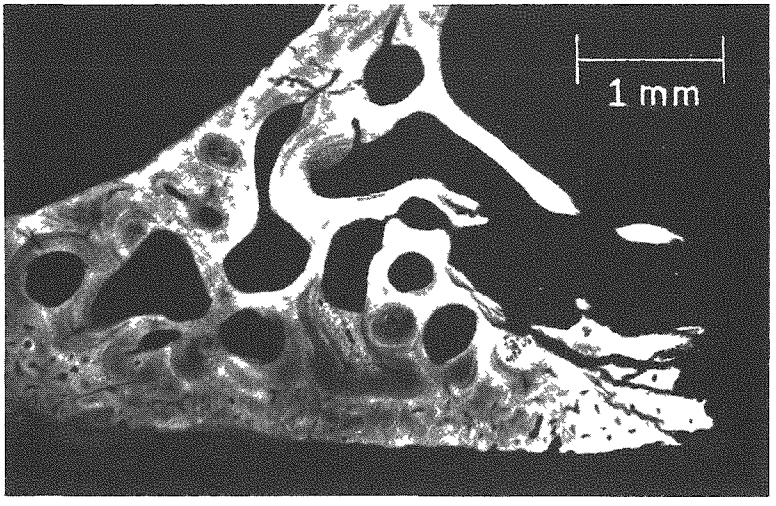

Fig. 7. A microradiograph of a tibial section from rabbit No. 12. Some osteons have enlarged lacunae and some have calcified or hypercalcified tissue in the central canal. The peg hole is at the lower right.

Rabbit No. 8 survived 442 days. The x rays showed increased density around the 11.6 - μc peg in the diaphysis of the right tibia (Fig. 8), which was seen on the microradiograph (Fig. 9) to be due to abnormal cancellous bone which half filled the marrow cavity.

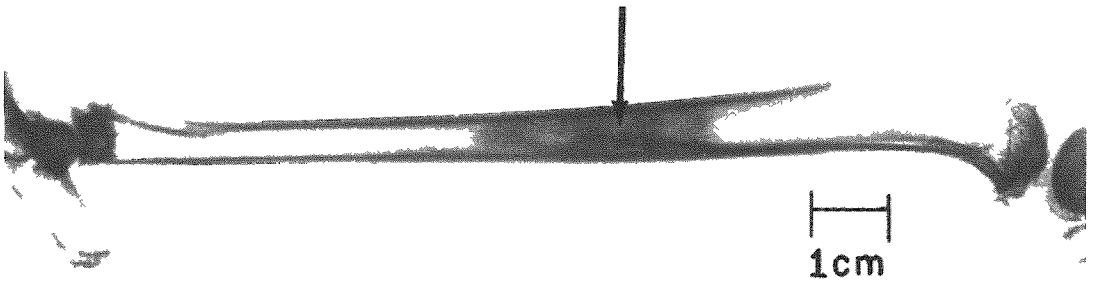

Fig. 8. A contact print of the x ray of the right tibia of rabbit No. 8, showing bone proliferation suspected to be an early osteogenic sarcoma. The location of the peg is indicated by the arrow.

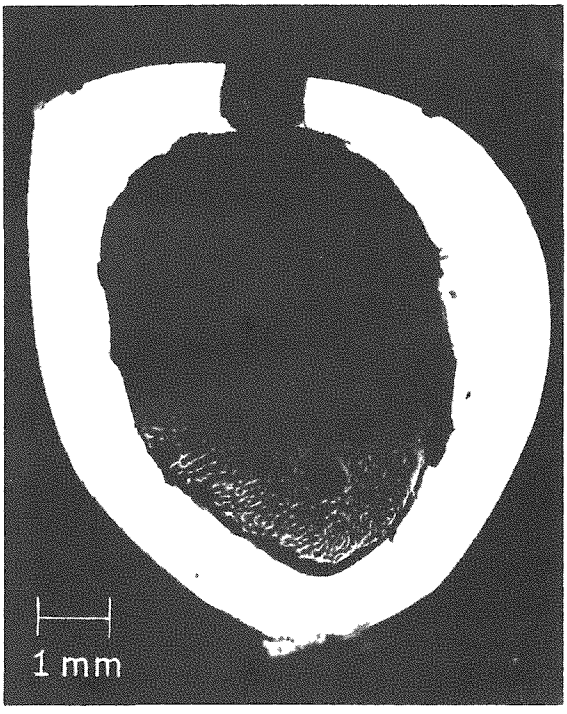

Fig. 9

An underexposed microradiograph of a section from the right tibia of rabbit No. 8. There is abnormal bone in the marrow cavity which appears to have developed from endosteal new bone on the side of the marrow cavity away from the peg.

Dosimetry

Loevinger's point-source dose function can be employed to describe the dose around a point source of a beta emitter[1] and, with suitable modifications, the dose distribution around a spherical beta source can be obtained from this function.[2] The dose rate to bone and to soft tissue around the Sr^{90} pegs were determined with Loevinger's function although several simplifying assumptions were required. First, the pegs were

assumed to be spheres 1 mm in diameter instead of cylinders. Second, it was assumed that the Sr^{90} was uniformly distributed throughout the peg, and that none was lost from the peg during its residence in bone.*

A more important assumption is required because Loevinger's function describes the dose distribution in a uniform medium: we have the isotope in a Scotchcast sphere (a density 1.3 g/cm^3) surrounded by bone (density assumed to be 2.0 g/cm^3) and soft tissues (density assumed to be 1.0 g/cm^3). Thus, our calculated values are to be considered as approximations to the true dose distributions, which are too complex to calculate (for all pegs employed).

The dose distributions outside a spherical Sr^{90}-Y^{90} source have been calculated for two cases, a uniform medium with density 1 g/cm^3, and again for a density of 2 g/cm^3. In each case the 1-mm bead was assumed to have the same density as its surroundings. These calculations are plotted in Fig. 10 in terms of the dose rate as a function of distance from a 1-μc Sr^{90}-Y^{90} source.

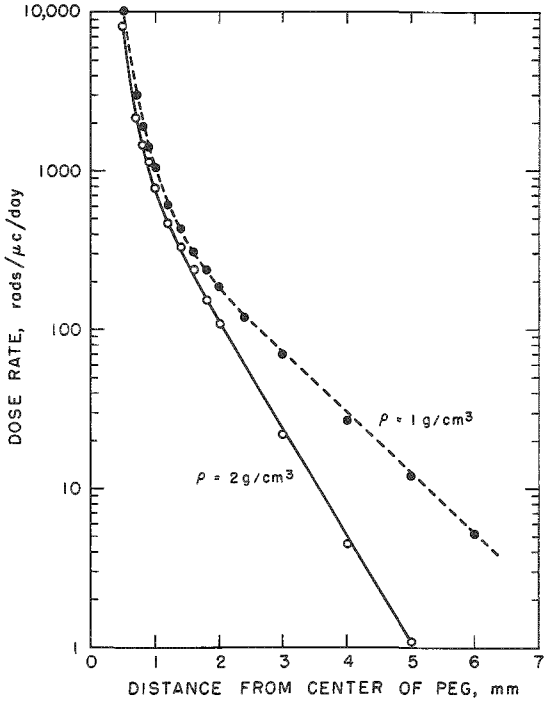

Fig. 10

The dose-rate distribution, in rads/μc/day, around a spherical source (1 mm in diameter) of Sr^{90}-Y^{90} for two values of density. These calculations assume that the spherical source has the same density as the surrounding materials.

*A measurement of the whole femur of rabbit No. 6 was made, after it had been dissolved in HNO_3, but no Sr^{90} was detected. The limit of sensitivity of this measurement was such that we can state that no more than 0.5% of the total Sr^{90} in the pegs in this rabbit was lost from the pegs, if 25% of the lost Sr^{90} was subsequently deposited with the rabbit's skeleton.

Considering the uncertainties in the absolute Sr^{90}-Y^{90} content of the pegs and the assumptions inherent in the dose calculations it is evident that an appreciable uncertainty is present in the dose values. The parameters employed in Loevinger's dose function and the beta energies and ranges are listed in Table 4.

Table 4

Beta energies and ranges

	Sr^{90}	Y^{90}
E_{max}	0.536 Mev	2.24 Mev
E_{av}	0.198 Mev	0.90 Mev
Range: when density $\cong$ 1 g/cm^3	2.16 mm	10.95 mm
Range: when density $\cong$ 2 g/cm^3	1.08 mm	5.48 mm

Parameters employed with the point-source function

c (a dimensionless parameter)	1.5	1.0
v (apparent absorption coefficient)	39.9 g/cm^2	6.2 g/cm^2

The calculated dose at the bead surface is dependent upon the density assigned to the bead itself. In Table 5 are listed the calculated surface doses for the two assigned densities 1 and 2 g/cm^3. For comparison, the calculated dose for the actual bead density, 1.3 g/cm^3, is included.

Table 5

Bead surface dose

Density, g/cm^3	Dose rads/μc/day
1	10330
2	8290
1.3	9500

Figure 11 is a microradiograph of a tibia cross section from rabbit 8, on which isodose contours have been indicated. Many of the drill holes were found to have pierced the marrow cavity, such as in this case,

but in every case the peg was found to have remained in the cortex. This simplifies the dose interpretation in that the dose to the marrow cavity is dependent only on a two component system, peg and soft tissue, rather than a three component system, of peg-bone-soft tissue.

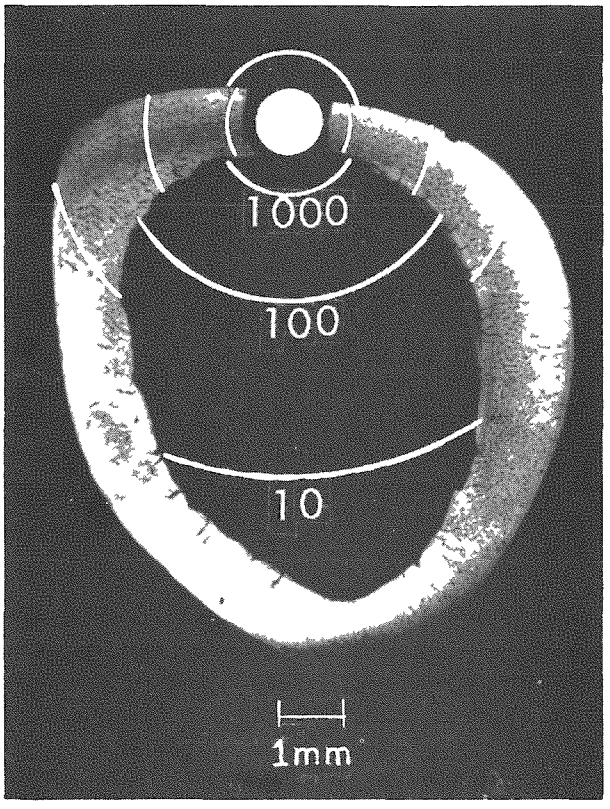

Fig. 11

The microradiograph of the tibia cross section from rabbit No. 8 shown in Fig. 9, on which contours of equal dose rate have been drawn. The units are rads/day/μc; contours for 1000, 100 and 10 rads/day/μc are shown in the marrow cavity (density = 1 g/cm^3) and in bone (density = 2 g/cm^3).

The contours in Fig. 11 are labeled in units of rads/day/μc Sr^{90}. (The peg employed in Rabbit 8 contained 11.8 μc, so the labeled contours are to be multiplied by 11.8 to obtain the actual dose rates.)

With the dose rate distribution known, one can correlate dose and dose-rate levels with the visible signs of damage. For example, in Figs. 2a and 2b, a line of demarcation which corresponds to a dose rate contour of 50 rads per μc per day, between the dark staining osteocytes and the empty lacunae is found to be close to the circumference of a circle with its center in the peg hole and with a radius of 2.4 mm. Since this peg contained 7.3 μc Sr^{90}, and this rabbit survived 92 days, this contour represents an accumulated dose of 34,000 rads.

In Fig. 3 we see the same type of demarcation between dark staining osteocytes and empty lacunae, occurring at a distance of 2.3 mm from the peg center. This distance corresponds to a dose-rate contour of 70 rads/μc/day, and an accumulated dose of 47,000 rads.

In the case where we have visible abnormal bone proliferation (Fig. 8, suspected osteogenic sarcoma), the locus of growth seems to be the endosteal surface opposite the peg. The dose rate here is of the order of 60 rads/day, which accumulated to 26,500 rads at time of sacrifice, or 25,000 rads when the proliferation was first seen by x ray. This accumulated dose is much greater than the average skeletal dose usually associated with a high probability of bone tumor induction, namely values of the order of a few thousand rads to soft tissue.[3] However, in this experiment only a small fraction of the total skeleton received the radiation dose, so that the fraction of the cells at risk is very much less than in the case of complete skeleton deposition. Since it is not unlikely that the probability of a tumor appearing in a given animal is dependent both on the number of cells at risk and on the dose received by the cells, the tumor probability per rad should be low in this type of experiment. Thus the occurrence of two (?) tumors in the nine animals surviving longer than 140 days is perhaps quite remarkable.

Conclusions

Cell death and tumor induction are two significant responses of bone to the intense local dose delivered by the point sources of beta irradiation.

The sharp demarcation between the dark staining osteocytes and the empty lacunae was found to correspond to an accumulated dose of the order of 35,000 to 45,000 rads. Actual cell death may have occurred at lower doses, for the change in the histological appearance of a cell may lag in time after its death; but the fact remains that this technique, with lower dose rates, should provide a method of determining the dose required to kill these cells in vivo. In addition, since normal bone growth was evident around control pegs, indicative that the vascular supply was not permanently damaged by the process of inserting the peg, it would then appear that the cell death around radioactive pegs was the result of direct beta irradiation, not disruption of the vascular supply.

Since the site of origin of the tumors could not be determined, other than that they seemed to arise from within the irradiated volumes, we cannot determine either the dose delivered to the site, or the cells directly involved. It is noteworthy, however, that two tumors were induced within the diaphysis, and none within the metaphysis, although the number of tumors induced is obviously too low to be truly significant. Tumors, when induced in the long bones by means of bone-deposited isotopes, are often found in the metaphyseal region; however, this region is also the site of the largest uptake of these isotopes, even in the adult animal. Thus, with such experiments one cannot determine whether the high tumor incidence in this location is due to an increased sensitivity of the cells in this region, or to the increased number of cells that are irradiated here, or to the higher radiation dose delivered by the isotope in this region. The

point-source technique, by eliminating the inequalities of dose and volume irradiated, may clarify some of the perplexing problems involved in tumor induction studies and complement studies of partial skeletal irradiation by x rays, which, however, also irradiate adjacent soft tissues with doses comparable to those received by the bone.

We are grateful to C. H. Williams for aid in inserting the radioactive pegs in these animals, to Dr. M. P. Finkel for providing the continual x-ray service required, and to D. Banister for the care of the animals.

References

1. Loevinger, R. The Dosimetry of Beta Sources in Tissue. The Point Source Function. Radiology 66 55 (1956).

2. Loevinger, R., Japha, E. M., and Brownell, G. L. Discrete Radioisotope Sources, in Radiation Dosimetry, ed. G. J. Hine and G. L. Brownell. New York: Academic Press, (1956).

3. Cater, D. B., Baserga, R., and Lisco, H. Studies on the Induction of Bone and Soft Tissue Tumors in Rats by Gamma Irradiation and the Effect of Growth Hormone and Thyroxine. Brit. J. Cancer 12 214 (1959).

PLUGGED HAVERSIAN CANALS IN A RADIUM CASE

R. E. Rowland

Microradiographic examination of bone sections from individuals who have carried at least a microcurie of radium for many years has shown that occlusion of the haversian canals is the most frequent change which has taken place. A plug of mineral with a microscopic density greater than that of the surrounding bone fills many of the canals. Previous studies[1] have shown that these plugs are relatively short, their estimated length being only 500 microns. They do not seem to be directly correlated with the radium hotspots in the bone sections examined, but the number of plugs does seem to be related to the total skeletal content of radium. A study of the extent of these plugged canals has now been made in order to determine in greater detail the length of the occlusions, their relative number, and thus the degree to which they might reduce the blood flow in the capillaries in bone.

A half-inch length of cortical bone from the tibia of case 302*[1] was cut into 49 successive sections, each 100 microns thick, with a rotary saw 150 microns thick. Each section was microradiographed and subsequently covered with a stripping film to produce a high resolution alpha-track autoradiograph.

A group of osteons which contained a large number of plugs and partial plugs was selected for study. These osteons are those included within the outlined area on the microradiograph of the first bone section, Fig. 12a. These systems were traced from section to section and coded as to whether they were plugged, partially plugged, or apparently normal; in addition, they were examined to see whether or not they were intensely radium-labeled, i.e., could be called radium hotspots. There were 52 osteons included within the defined area on the first section. This number subsequently increased as some systems branched to form two systems, or when a new system migrated within the area defined by the original osteon set. On the other hand, the total number was decreased when some

---

*Case 302 painted watch dials for a two-month period at age 15 and died at age 47 with an osteogenic sarcoma. The terminal body burden is reported to be 3.8 μc although the radium diffuse level is characteristic of a higher level.[2] The ratio of Ra^{228} to Ra^{226} at time of acquisition was determined to be 0.12 ± 0.01 by Wallace et al.,[3] which is one of the highest Ra^{228} levels these authors have found to date. The terminal dose rates were measured and found to be 16 rads/day in the maximum hotspots and 0.43 rads/day in the diffuse distribution.[2]

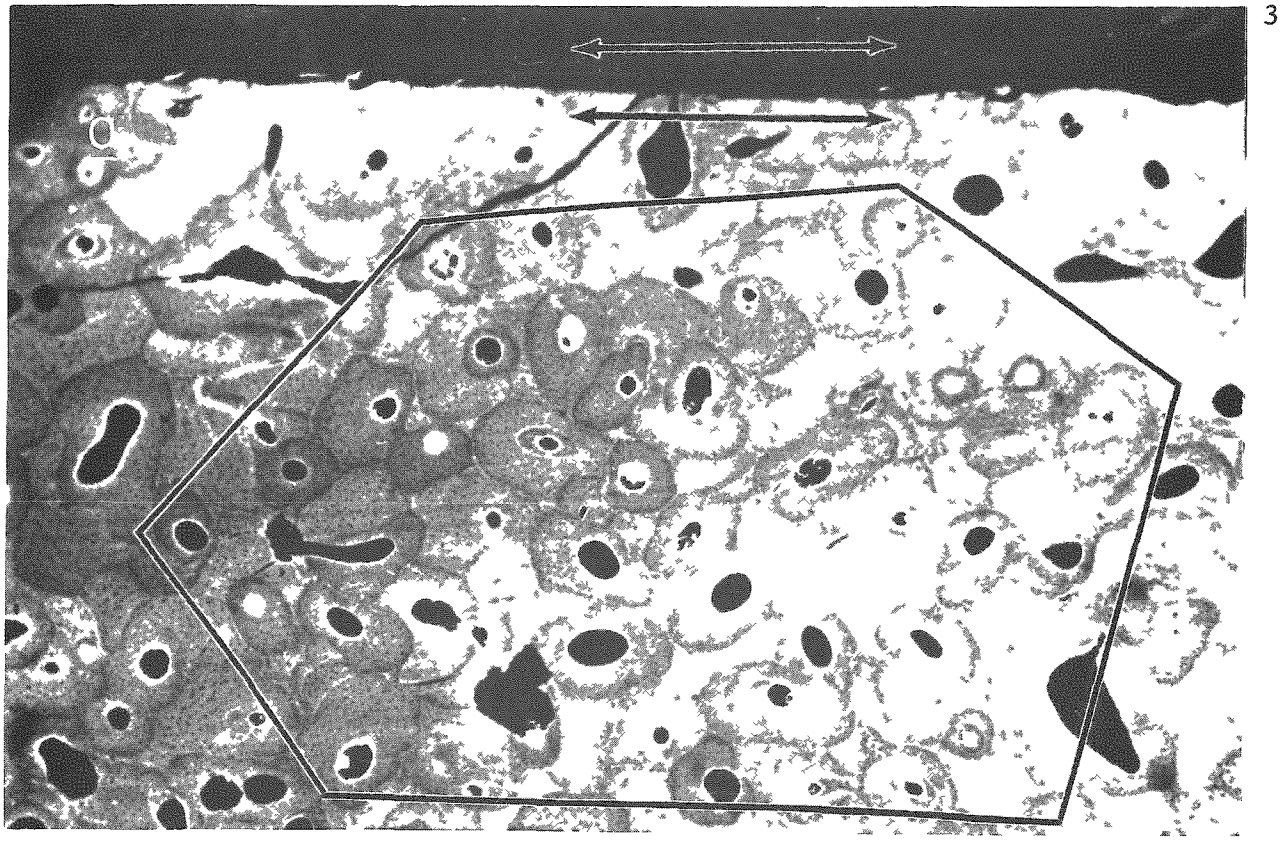

Fig. 12a. The microradiograph of the first of 49 sections cut from the tibia of case 302. The osteons traced are those included within the outlined area. The scale arrow is 1 mm long.

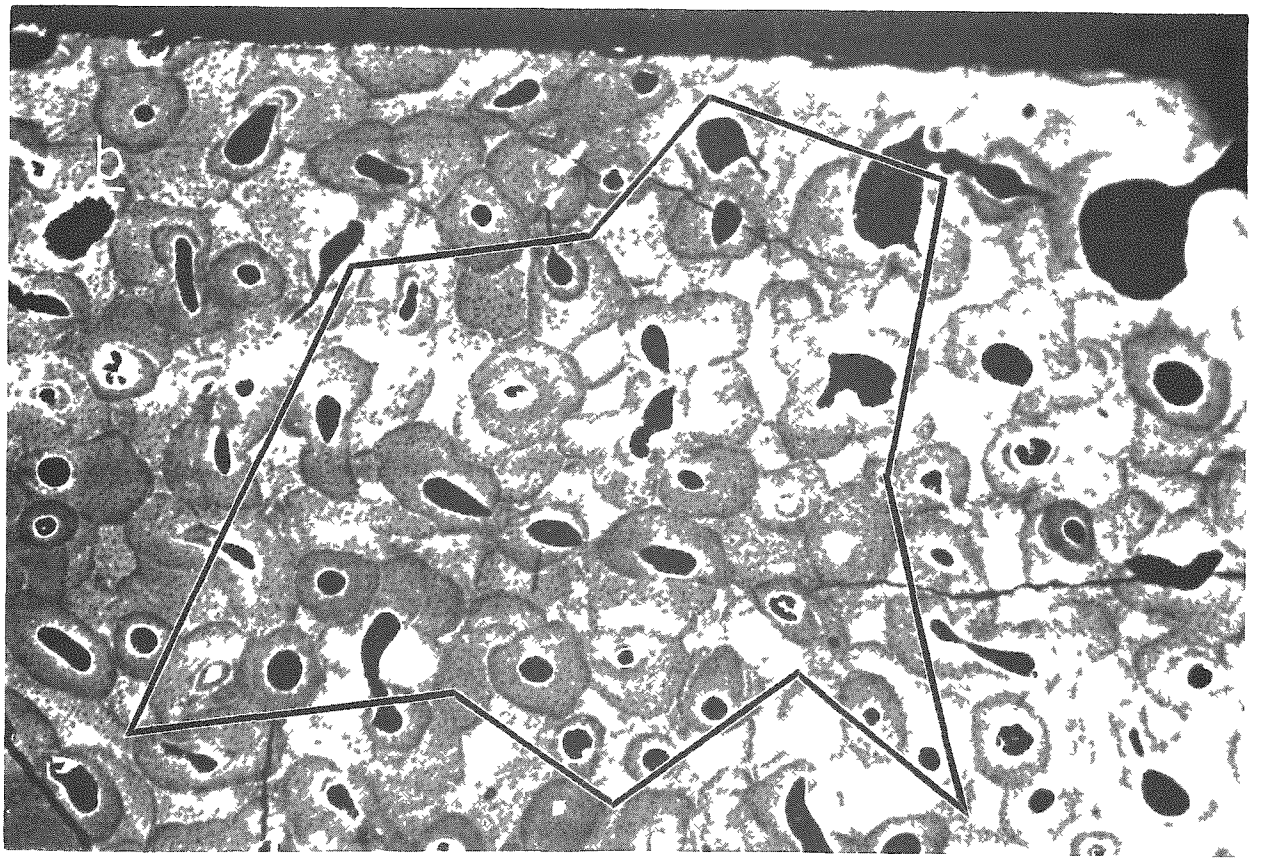

Fig. 12b. The microradiograph of the 49th section, the osteons still included in the survey are within the outlined area. The scale is the same as in 12a.

Fig. 13. A microradiograph of four plugged or partially-plugged haversian canals. These are taken from the 4th section in the series. The scale arrow is 100 microns long.

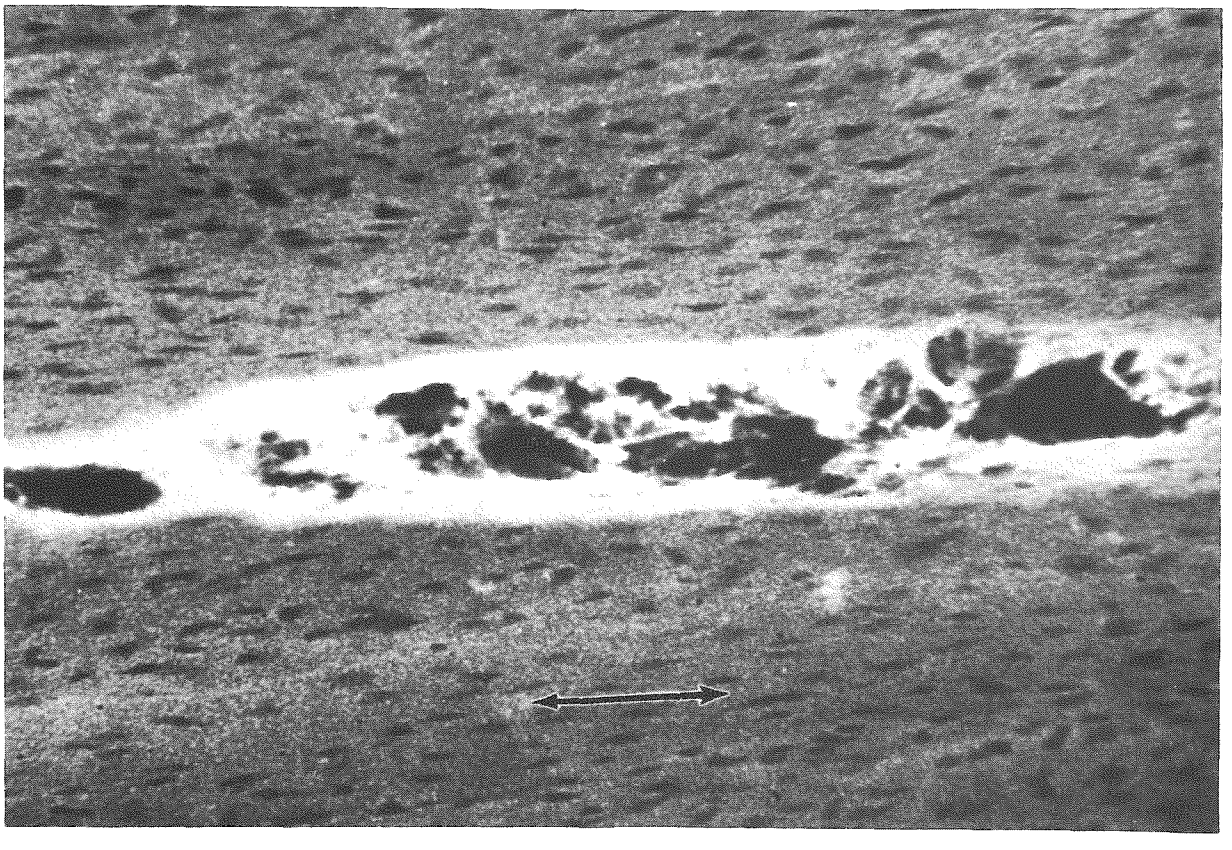

Fig. 14. A microradiograph of a 100-micron thick bone section cut longitudinally to show the change from complete plugging to partial plugging of the canal. The bone was from case 302. The scale arrow is 100 microns long.

systems combined, or when a system migrated far from its neighbors. As far as possible, the systems followed were part of a contiguous volume; from the outline of this area in Fig. 12b, the microradiograph of the last section, it can be seen that the total number of systems included terminally is somewhat less than the number originally followed.

It can be seen from Fig. 13 that a haversian canal can be completely or partially filled with mineral, or can just contain hypercalcified material around the edges. In analyzing such systems, they were classified as either plugged or partially plugged. The distinction between the two classifications is completely arbitrary; in Fig. 13 the canal in the upper left hand corner is an example of a borderline case. The distinction is probably unnecessary, for as is shown in Fig. 14, a microradiograph of a bone section cut longitudinally, the mineral in the canal sometimes completely fills the opening, yet a short distance away it may do so only in part. In some locations, the occluding material seems to be fibrous in nature, yet if these are thin fibers rather than edge views of a thin sheet, the implication is that the material is very dense in order to be so distinctly visible on the microradiograph.

In order to aid in the visualization of the information obtained, the haversian canal system has been diagrammed in a very formalized manner in Fig. 15. Here no concern has been shown regarding size of the systems or their spatial arrangement; rather the diagram may be considered to be a map of the canals and their cross connections with each other. Since a cylindrical column of bone has here been reduced to a diagram on a plain surface, systems immediately adjacent to each other in the bone may well have been plotted far removed from each other on the map. Branches are indicated between the canals as horizontal connections. Where a branch leads to a canal not included in this analysis this is indicated simply by an opening in the side wall of the system. In some cases where the cross connections were numerous and the required number of horizontal branches would be confusing, a connection between two systems was indicated by an opening in the side of the wall, with the canal to which the branch connected being indicated by placing the canal number within this opening.

In Fig. 15, the vertical space assigned to each section can be visualized by the size of the gaps left for the three missing sections. Actually, between adjacent sections there is missing a space of 150 microns, the thickness of the saw blade, while the sections themselves are only 100 microns thick. In the diagram each section has been considered to be 250 microns thick, a convenience adopted in order to eliminate the 48 spaces between the 49 sections.

From a cursory examination of Fig. 15, it is evident that the solid plugs are not very long; their average length has been determined from this figure, making the important assumption that the minimum length of

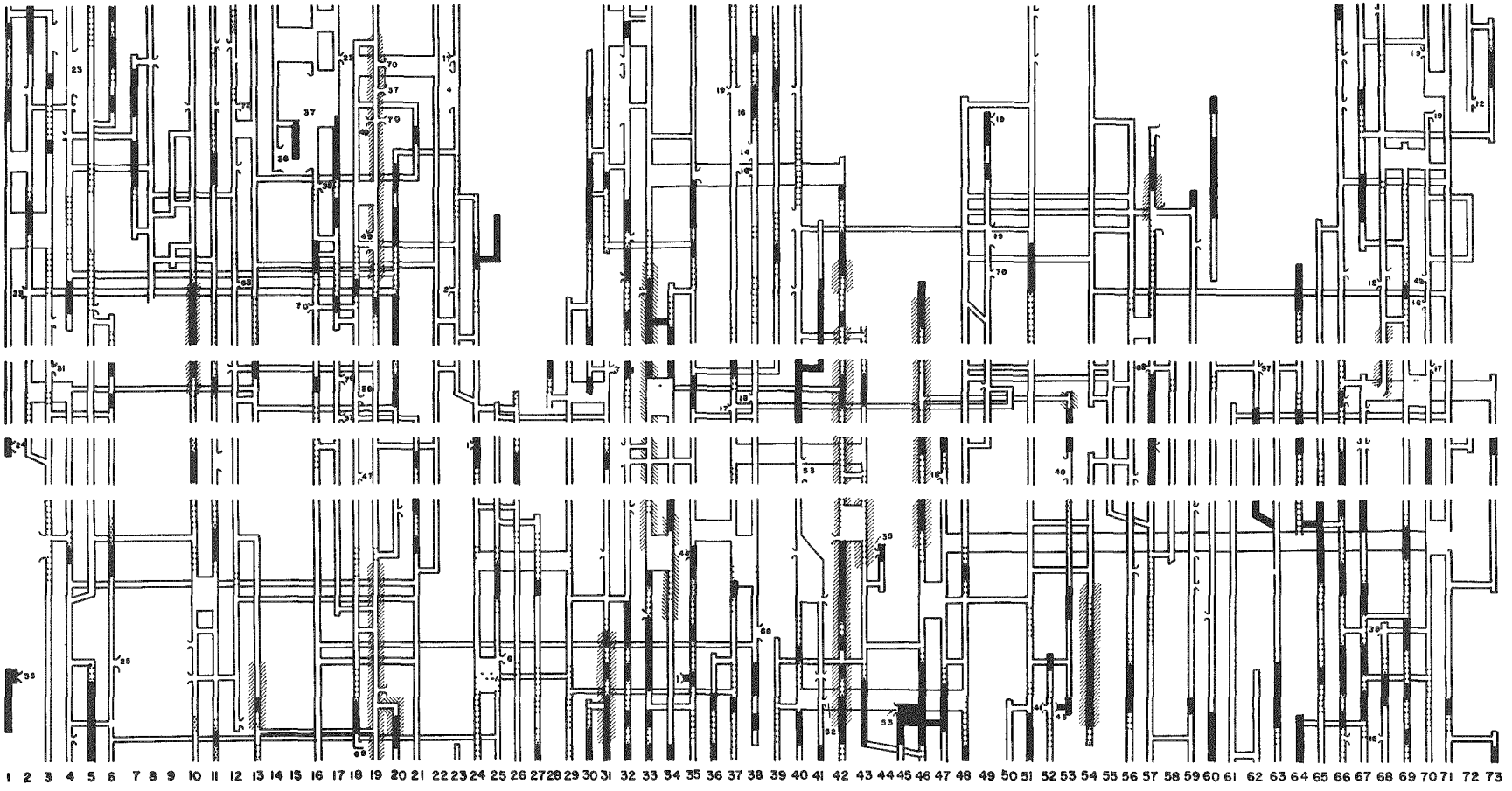

Fig. 15. A diagram of the haversian systems traced through 49 sections of bone from the tibia of case 302. The first section is on the bottom and the 49th at the top. The three gaps indicate the location of three missing sections, 18, 22, and 27. The presence of hypercalcified material within the canals is represented as follows: the solid black areas with the canals indicate that the canal was plugged; the dotted areas were those regions partially plugged. The hatched lines outside of the canals indicate haversian containing a high concentration of Ra^{226}, or hotspots.

the plug is 250 microns. That is, if the 100-micron thick section showed a plug, then it was assumed that the 150 microns of kerf were plugged also. Likewise, if the sections on both sides of a missing section showed solid plugs, the missing section was assumed to have a solid plug in that particular osteon. The average length of the solid plugs, as defined above, was found to be 480 microns, ranging from only one section thickness in length, (in 49% of the plugs) to as many as seven sections, namely 1750 microns.

A closer examination of Fig. 15 reveals that adjacent to the solid plugs in a given osteon there are often found partial plugs. It is perhaps of greater significance to determine the average length of a region which is either partially or completely plugged, particularly in light of the longitudinal appearance of a plug, as shown in Fig. 14, where we see the transition from solid to partial plug. Using the same approximation mentioned above, the average length of a plugged canal was determined to be 900 microns. In this case 30% of the plugs were only one section thickness in length, whereas the longest such region extended for 20 sections, or 5000 microns.

If the data are examined statistically, the number of solid plugs per osteon per bone section is found to be 0.16. Considering both solid and partial plugs, this number increases to 0.32. That is, in these areas examined on these 49 sections, on the average 32% of the osteons in each section contained a partial or a complete plug. The actual range was from a low of 14% (section 44) to a high of 40% (section 3). From a previously published study[1] bone from this patient was found to have 29% of several thousand osteons occluded, the maximum number found in any of the patients studied.

Is there complete stoppage of all blood flow as a result of these many plugs occurring in almost all osteons? With the microradiographic technique alone we cannot tell, but if we examine the number of interconnections between osteons, it becomes evident that whereas the plugs must certainly reduce the blood flow, there are sufficient alternate routes to permit some blood flow. From Fig. 15 the number of interconnections per osteon per 250-micron length was found to be 0.30, so that 30% of the canals have an interconnection in each bone section examined. This seems like a large number of branches for each 250-micron length of osteon. Indeed, it might be high as a result of a need for many branches to counteract the effects of the plugs. However, before arriving at this conclusion, it would be wise to examine the number of branch canals found in similar volumes of normal adult human bone. A similar study in a suitable control bone has not been made, but there is an interesting study on the haversian systems in canine bone with which we can compare some of our results.[4]

Before quoting the results of this study by Cohen and Harris,[4] it is well to consider the differences that may exist between canine and human bone. As was shown by Jowsey et al.,[5] the average diameter of

secondary haversian systems in human beings is twice that for similar systems in the dog. Likewise, it is also true that the haversian canal itself is larger in human bone than in canine bone. These differences in size are impressive and may indicate that quantities that are measured in respect to size, like the number of branches per unit osteon length, cannot be compared directly between the two species.

With these thoughts in mind, we find that, while Cohen and Harris did not explicitly state the number of branches per unit length, we can calculate this quantity from their Fig. 7 and obtain the value 1.1 branches per 250-micron length of osteon. This is greater than the number we found; but, considering the species differences, the variance is perhaps not of significance in comparison of radiation damage to bone.

It should be mentioned that, while our study was undertaken for a completely different purpose than that of Cohen and Harris, and utilized different techniques, in both studies a group of osteons was followed through a considerable length of compact cortical bone. In one marked respect, different results were obtained. In the canine femur, the osteons were found to migrate from the periosteal lamellae to endosteum in a length of approximately one centimeter, and at the same time, to describe a gentle spiral around the axis of the bone. These phenomena were not observed in our study through a half inch of human cortical tibia.

Turning our attention to the radium-labeled haversian systems, or hotspots, we wish to know if there is any correlation between the hotspots and the hypercalcified plugs. There are 17 hotspots indicated in the diagram (Fig. 15), with an average hotspot length of 2000 microns. The ratio of the number of hotspot osteons per section that contain a plug or partial plug to the total number of hotspot osteons is 0.60. This is twice as large as the value obtained for the number of osteons containing such plugs, 0.32. However, since the number of hotspots included in the analysis is small, we cannot state with certainty that there is a correlation between plugs and hotspots; but there is a suggestion that this may be the case. In fact if the hotspots are examined throughout their length, less than 25% show no occlusions of some sort.

Plugged canals are not limited to the radium-bearing human being. Dogs which have carried Ra^{226} for a number of years have shown plugged canals,[6] although perhaps not as many as we find in human radium cases. Indeed, we are not limited to the alpha-emitting radium isotope, for we have found these plugs in dogs which have been burdened with Sr^{90} for a number of years. In fact, a few plugged canals have been found in the bones of normal (i.e. no radioactive burden) human beings although the few such plugs we have seen have been located very close to the periosteum rather than throughout the compact bone.

In summary, the plugs in the canals of a radium dial painter have been studied in depth, and found to be relatively short, with an average length of only 480 microns for the solid plugs, and 900 microns for solid and partial plugs. The number of canals plugged in any bone section is relatively constant, for the plugs are not contained in a few osteons, but appear in almost all of them. Thus it would appear that blood flow must be severely limited, but since the number of interconnections between canals is quite large, there still exists the possibility of collateral circulation.

References

1. Rowland, R. E., Marshall, J. H., and Jowsey, J., Radium in Human Bone: The Microradiographic Appearance. Radiation Research 10 323-334 (1959).

2. Rowland, R. E., and Marshall, J. H., Radium in Human Bone: The Dose in Microscopic Volumes of Bone. Radiation Research 11 299-313 (1959).

3. Wallace, D. E., Stehney, A. F., and Ilcewicz, F. H., Th^{228}, Ra^{228}, and Ra^{226} in Bone. Radiological Physics Division Semiannual Report, ANL-5967 (May 1959) pp. 107-110.

4. Cohen, J., and Harris, W. H., The Three-Dimensional Anatomy of Haversian Systems. J. Bone and Joint Surg. 40-A 419-434 (1958).

5. Jowsey, J., Marshall, J. H., and Rowland, R. E., Variations in Haversian Systems Sizes. Radiological Physics Division Semiannual Report, ANL-5829 (February 1958). pp. 93-94.

6. Jee, W. S. S., and Arnold, J.S., The Effect of Internally Deposited Radioisotopes Upon the Blood Vessels of Cortical Bone. Annual Report, Radiobiology Division, University of Utah, COO-220 (March, 1960), pp. 150-165.

AUTORADIOGRAPHIC DOSIMETRY OF MOUSE BONES CONTAINING Ca^{45}, Sr^{90}, or Ra^{226}

II. The Sensitive Region in the Induction of Osteogenic Sarcomas

John H. Marshall and Miriam P. Finkel *

Dosimetric studies of mice injected with Ca^{45}, Sr^{90}, or Ra^{226} have suggested that Ca^{45} or Ra^{226} hotspots do not deliver much of their dose to the regions of bone that are sensitive to the carcinogenic effect of radiation.[1] This interpretation of the data is presented here in greater detail. In order to emphasize the steps in the reasoning, the following argument is given in underlined statements that can be read independently of the rest of the material. Discussion of the data and the assumptions involved are inserted after each statement.

The purpose of this argument is to attempt to construct one consistent explanation of the experimental results. The factors of dose distribution, target localization, dose rate versus accumulated dose, tumor location, time of tumor appearance, and shape of the dose-response curve are so interrelated that there can be no assurance that the present interpretation is unique. However, so many of these factors are so similar for Ca^{45} and Sr^{90} that the difference in tumor incidence for comparable doses can probably be ascribed almost solely to the effect of their different particle ranges. In essence, Sr^{90} produces a uniform dose distribution, and Ca^{45} both a uniform distribution, the diffuse component, and a very nonuniform distribution, the hotspots. By comparing the available dosimetric and tumor incidence information, one should be able to determine whether or not the Ca^{45} hotspots are located in sensitive regions.

Argument

1. The accumulated doses from Sr^{90} and Ca^{45} have an almost constant ratio from ten days to three hundred days after injection. Therefore, the following argument is not complicated by considerations of a time-intensity factor.

A plot of the accumulated dose in rads versus time after injection is shown in Fig. 16. The data refer specifically to the femurs of CF No. 1 female mice given a single intravenous injection of the amounts of Ca^{45}, Sr^{90}, or Ra^{226} listed in the figure. However, they also apply to other regions of the skeleton with minor changes.

---

*Biological and Medical Research Division

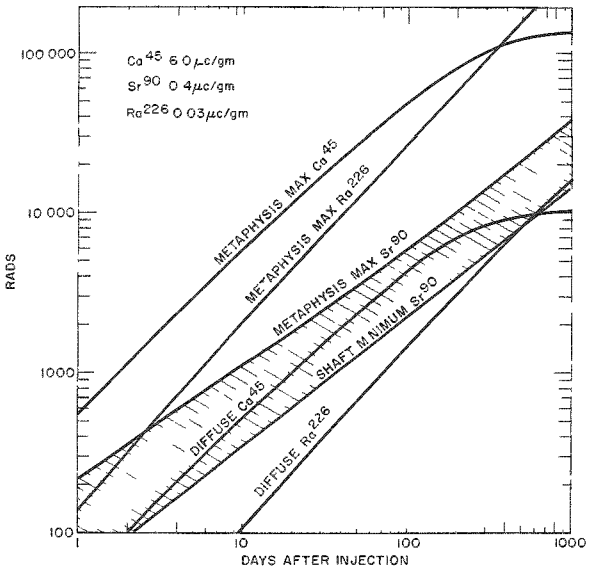

Fig. 16. Accumulated dose in rads to the femurs of 70-day old CF1 female mice given a single intravenous injection of the listed amount of Ca^{45}, Sr^{90}, or Ra^{226}. (μc/gm refers to injected activity per unit body weight.)

The accumulated dose from Sr^{90} increased less rapidly than that from Ca^{45} during the first 100 days after injection because Sr^{90} dose rates were decreasing. Since Sr^{90}-Y^{90} beta particles have a relatively long range, removal of the isotope anywhere within a small mouse bone during the normal processes of remodelling reduces the dose rate everywhere. In the case of Ca^{45}, on the other hand, resorption reduces the dose rate only in the immediate area because the particle range is short. In contrast to this situation, which tends to result in a greater rate of accumulation of dose from unresorbed Ca^{45}, radioactive decay limits accumulation; the halflife of Ca^{45} is 163 days. The combination of these two effects results in similar slopes for doses accumulated from Ca^{45} and from Sr^{90} between about 10 and 300 days after injection.

Dose accumulated after 200-300 days is probably not very important to the induction of osteogenic sarcomas in these mice for two reasons. First, the time of death of the median tumor-bearing animal ranges from about 220 days to 500-600 days (Fig. 17) and this includes a period between the induction of an osteogenic sarcoma and the death of the animal that bears it. Second, and more directly, the temporal distribution of tumor deaths is almost the same for Ca^{45} and Sr^{90}, even at the later times when there has been considerable radioactive decay of Ca^{45}. Therefore, it seems to be a reasonable assumption that any dose rate-versus-time factor in the production of osteogenic sarcomas affects the Ca^{45} mice and the Sr^{90} mice in about the same way.

One possibly important feature of the dosimetry does not appear in Fig. 16, namely, the high dose rate adjacent to the distal epiphyseal plate of the femur soon after injection. The dose rate measured in this location was about 50% higher than that found anywhere else. However, nearly all the activity was resorbed from this site by about 10 days after injection. By 100 days after injection, the accumulated dose in the metaphysis, which was still increasing, already was 3 to 4 times larger than the dose that had been accumulated adjacent to the plate.

2. The particle range of Sr^{90}-Y^{90} is so great that a region of the mouse skeleton several hundred microns across is almost uniformly irradiated. Therefore, an estimate of the dose that is actually effective for tumor induction by Sr^{90} does not require knowledge of the microscopic location or size of the radiation-sensitive region.

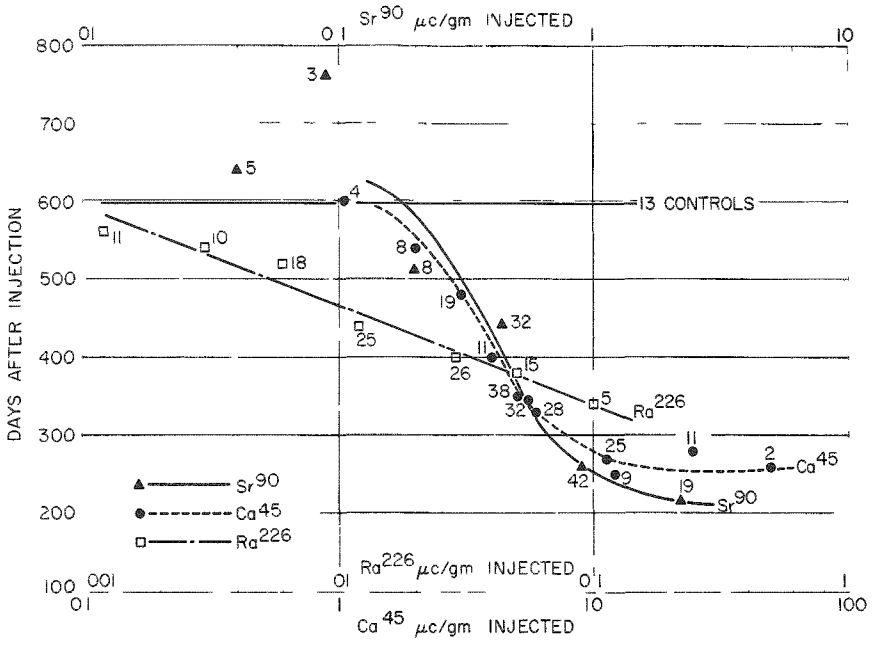

Fig. 17. The median time of death of the tumor animals as a function of the injected activity per unit body weight. (These median times of death are quite similar to those for the entire populations. They do not reflect a specific tumor effect).

A typical example of the dose distribution in a mouse skeleton is given in Fig. 18, which shows dose profiles across the midshaft of the femur three days after injection. The positions of the peak dose rates for Ra^{226} indicate the edges of the cortical bone. The Sr^{90} dose rate within and near cortical bone is quite uniform: the dose within the bone is comparable to the dose near the surface.

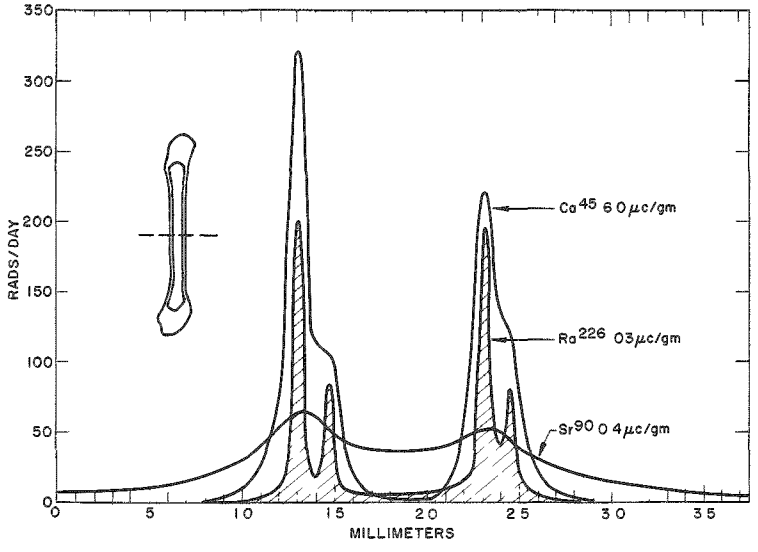

Fig. 18

The dose rate profiles across the midshaft of the femur three days after injection. The positions of the Ra^{226} peaks indicate the edges of the cortical bone. These profiles are typical of much of the skeleton.

3. On the basis of tumor data from the toxicity experiments,(2) injected levels of Ca^{45} and Sr^{90} were selected that yielded equal tumor incidences.

There is some uncertainty in establishing equal tumor incidences. First, there are differences in the location of tumors induced by the two materials. For example, 35% of the tumors produced by Sr^{90} appeared in the femur whereas only 19% of those produced by Ca^{45} appeared there. On the other hand, a larger proportion of the Ca^{45} tumors appeared in the small bones, such as the rib. This effect can be explained in terms of the respective doses. Limiting the comparison to one skeletal location would avoid this difficulty, but then tumor statistics would not be adequate. Second, although the shapes of the dose-response curves for Ca^{45} and Sr^{90} are very similar, they may not be exactly the same. Consequently, the injected levels that result in equal tumor incidences may depend somewhat upon tumor incidence. Third, the present comparison has been based upon the incidence of tumor-bearing animals rather than upon the incidence of tumors within the population. These two ways of computing incidence give somewhat different results, but the differences in this particular instance are not very great. Taken together, these three uncertainties in selecting carcinogenically comparable injection levels of Ca^{45} and Sr^{90} probably lead to less than a factor of two in dose.

4. Comparing the doses from these two carcinogenically comparable injection levels (Fig. 16) we find that the diffuse Ca^{45} dose lies between the maximum and minimum Sr^{90} dose, within which the effective dose must lie. (step 2).

This relationship seems to imply that the Ca^{45} hotspots do not contribute to tumor induction. (This conclusion would be correct if the volume rather than the surface of bone were the target. However, see below).

Why do the Ca^{45} hotspots appear to be ineffective?

5. A priori, there are four possible reasons why the effective Ca^{45} dose level corresponds to the level of the diffuse component:

A. The true dose-response relation in each microscopic region is less steep than linear. That is to say, the local probability of tumor induction depends on less than the first power of local dose. In this case, a non-uniform dose distribution in a uniformly sensitive bone would produce fewer tumors than a uniform distribution of the same average dose.

B. The hotspots do not irradiate a large enough volume of bone to increase the tumor incidence significantly. This is related to point (A), but it deals with the dose distribution rather than the shape of the dose-response relation.

C. The doses delivered by hotspots exceed carcinogenic levels. This is again related to point (A), but it deals with the possible change in slope, the saturation and decrease, of the dose-response curve rather than the slope itself.

D. The Ca^{45} hotspots do not deliver much of their dose to the regions of bone that are sensitive to the carcinogenic effect of radiation.

Most of the Ca^{45} hotspots do not remain at the growing bone surfaces very long after injection because they are buried by continuing growth. Therefore, proof of (D) would indicate that irradiation of the osteocytes and bone matrix does not contribute significantly to the induction of bone tumors.

It is conceivable that the irradiation of osteocytes might contribute significantly to carcinogenesis at a nearby bone surface. However, this possibility would be minimized by a proof of statement (D).

6. The first explanation (A) is not very probable. The slopes of the dose-response curves for Ca^{45} and Sr^{90} are steep, tumor incidence probably increasing as the square or the cube of injected activity over the 10% to 80% incidence range where statistics are adequate.

In Fig. 19 the number of animals with osteogenic sarcomas divided by the number of animals alive at 150 days has been plotted against injected activity per unit body weight. The tumor incidence of the control population has been subtracted from every value. The bars on each point represent the standard error calculated from the observed number of tumor animals in each group. The error due to the uncertainty in control incidence is included and a binomial distribution about the observed number is assumed. Similar plots of these data have been published previously.[2]

Kamb and Pauling,[4] in an analysis of these and other Sr^{90} data from reference (3), have left the impression that within statistical error the incidence of mouse tumors is strictly proportional to radiation exposure. Their formulation includes the effect of survival time, which decreased as the amount of Sr^{90} injected increased. However, any correction for the time during which dose can accumulate will make the tumor incidence versus total dose curves steeper than those shown in Fig. 19, since at high doses and high tumor incidences survival time was relatively short (Fig. 17).

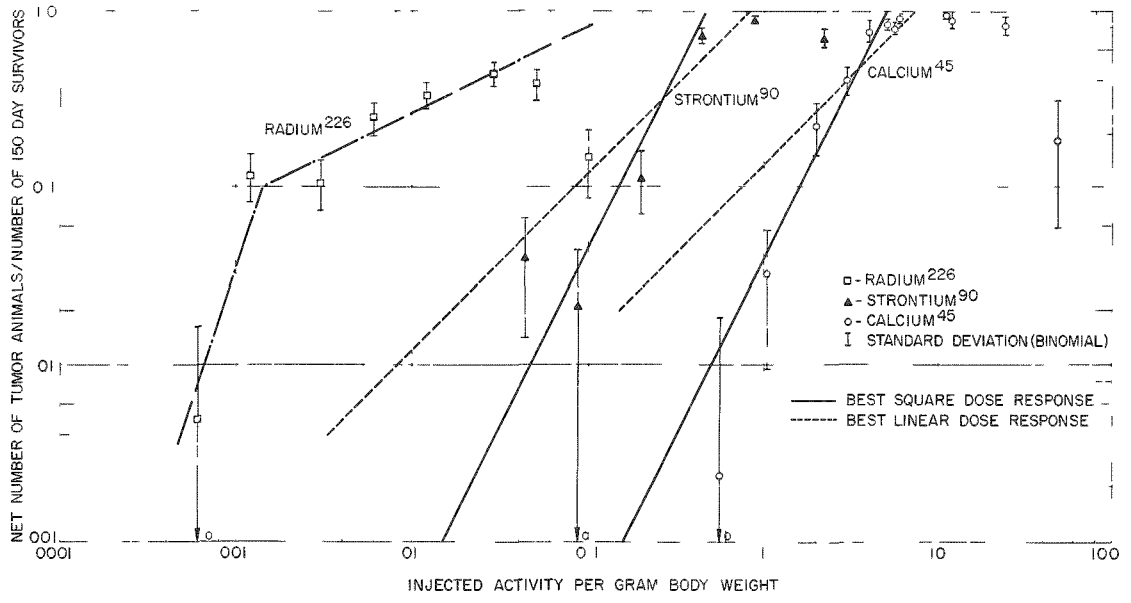

Fig. 19. The number of animals with osteogenic sarcomas divided by the number of animals alive at 150 days versus the injected activity per unit body weight. The tumor incidence among the control population has been subtracted from every value. The bars on each point represent standard error calculated from the observed number of tumor animals in each group. The error due to the uncertainty in control incidence is included, and a binomial distribution about the observed number is assumed. Similar plots of these data have been published previously. (2) However, some new Ca^{45} data are included.

Kamb and Pauling's demonstration of a linear dose relation for mouse tumors includes two errors. First, they show that the time to a 20% incidence of reticular tissue tumors could be described by a linear dose-response hypothesis. However, their formula implies that the incidence of reticular tissue tumors (corrected for survival time) will also be linearly dependent upon dose. This is not true: the total incidence of reticular tissue tumors is nearly independent of radiation dose throughout the entire experiment.(5) In other words, although large amounts of radiation cause these tumors to be manifest earlier, their induction does not seem to require any radiation at all. The linear hypothesis fits only part of the reticular tumor data, not all of it.

Second, Kamb and Pauling have incorrectly labeled their Fig. 3 "bone tumors" while it actually refers to the reticular tissue tumors. Although the same mistake is not made in their text, this error gives the false impression that they analyzed the bone tumor data. In Fig. 3

of M. Finkel's paper,[3] there is a striking difference between the slope of curve B, which represents the osteogenic sarcoma data, and curve C, which Kamb and Pauling analyzed.

Archer and Carroll[6] have also analyzed the Sr^{90} data in search of a linear relationship. They have lumped the reticular tumors with the osteogenic sarcomas, epidermoid carcinomas, and a few miscellaneous sarcomas. In view of the independence of the reticular tissue tumor incidence from dose, and the large number of these tumors at all levels, it is not surprising that an approximately linear dose-response curve results.

The present Sr^{90} data on the incidence of osteogenic sarcomas do not give unequivocal evidence for either a linear or a steeper dependence upon dose. From one point of view, the high incidence at 0.04 $\mu c/g$ might be regarded as a wild point, without which the fit to a square or cubic dose-response relation would be very good. However, with so few available points, eliminating a "wild" point cannot be justified. If all the Sr^{90} points are included except those for the two highest doses in Fig. 19, the least squares fit to a linear dose-response relation yields a chi square P value of 0.01. For a square dose-response relation, the best fit yields a P value of 0.03.

The Ca^{45} dose response curve is more complete, and previously unpublished results are included in Fig. 19. When the six highest dose points are omitted, the least squares fit to a linear dose-response relation yields a chi square P value of 0.03, while a square response gives a P value of 0.68. When only the four highest dose points are omitted, the best linear fit has a P value of 0.06, while the best square fit has a P value of 0.27.

One hates to omit points on a curve in a statistical test, but on the other hand, points with incidences over 80% cannot properly be included without a correction for the fact that an incidence of 100% cannot be exceeded. For the present purpose such a correction is not necessary.

It appears quite probable, especially in view of the Ca^{45} dose-response data, that the dose-response relation for Ca^{45} and Sr^{90} is steeper than linear, and quite possibly square or cubic.

7. Calculations based upon the distribution of dose to the volume of bone mineral and upon a square or cubic dose-response relation yield an effective dose for Ca^{45} of about four times the diffuse dose. Therefore (B) above can be eliminated.

The calculation of the non-uniformity factor (effective dose divided by average dose) is given in another section of this report. If the dose-response curve were linear and if all regions of the bone were equally

sensitive, then the effective dose would equal the average dose independently of the distribution. With a steep dose-response curve, the effective dose for Ca^{45} becomes about twice the average dose or four times the diffuse dose.

Note that this calculation is based on the assumption that bone volume (osteocytes and bone matrix) is the sensitive region. The factor of four between the result (step 7) and the observation (step 4) is the basis for rejecting explanation (B).

8. Because the dose-response curves for Ca^{45} and Sr^{90} have almost the same shape, the relationship in step 4 holds both at high injection levels and at low injection levels. The maximum Ca^{45} doses at low injection levels were comparable to the Sr^{90} doses at high injection levels. Therefore, the Ca^{45} hotspots at low injection levels do not exceed carcinogenic levels of radiation and (C) cannot be the explanation.

The elimination of possibility (C) would be difficult in any other fashion. One must be able to compare the effects of a uniform distribution and of a non-uniform distribution at injection levels so low that hotspot efficiency could not be impaired. In Fig. 19 it can be seen that an increase in the uniformly-distributed Sr^{90} dose, at least up to 1 $\mu c/g$, is associated with an increase in tumor incidence. It can be calculated from Fig. 16 that the dose accumulated by 100 days from 1 μc Sr^{90}/g is about 10,000 rads. An injection of 0.5 μc Ca^{45}/g would result in a tumor incidence of about 1% and and would yield a maximum accumulated dose from hotspots at 100 days of 10,000 rads. We may conclude that the Ca^{45} hotspots at the 1% incidence level do not deliver doses exceeding carcinogenic amounts.

9. With the elimination of possibilities (A), (B), and (C) the remaining alternative is that Ca^{45} (and Ra^{226}) hotspots do not deliver much of their dose to the regions that are sensitive to the carcinogenic effect of radiation.

10. The first corollary to this conclusion is that the osteocytes and the bone matrix are not the radiation-sensitive regions for the induction of osteogenic sarcomas. Radiation to these tissues is "wasted." Instead, it is the radiation escaping from the microscopic mineral surfaces that is primarily responsible for tumor induction.

Microscopic mineral surfaces are meant to include the endosteum and periosteum of cortical bone, the surfaces of trabeculae, and the walls of haversian canals, where haversian systems are present. Supporting evidence is provided by the carcinogenic effectiveness of plutonium,[7] which may remain at bone surfaces for long periods of time because the mechanism of deposition does not require the concurrent growth of the surface.

Note that step 10 is carefully worded so as to avoid the conclusion that it is solely the surface of bone that is sensitive. This argument does not determine the depth of the sensitive region.

11. The second corollary to step 9 is that the Ca^{45} hotspots, most of which are formed by calcium accretion at growing bone surfaces, are buried so rapidly that the dose at the bone surface remains low.

Direct calculation shows that such rapid burial is reasonable. If one assumes a constant surface growth rate of any suitable physiological magnitude, the accumulated dose at the bone surface from the Ca^{45} concentration resulting from a single injection is comparable to the diffuse dose accumulated for about 200 days. This dose is practically independent of hotspot intensity since more rapid growth results both in a more intense hotspot and in more rapid burial. Because of this process of hotspot burial one can understand how the effective dose could be equal only to the diffuse dose.* The calculations basic to this conclusion are the subject of a separate report.

Discussion

The lowest dose level in bone from a single injection of Ca^{45} is the surface dose arising from the diffuse component. This diffuse surface dose* is about one-half the diffuse volume dose because of the decrease in beta-radiation intensity at the surface of a thick source. The average dose for any part of the skeleton is about twice the diffuse volume dose, and hence, four times the diffuse surface dose. If the volume rather than the surface of bone were the target, the effective dose from both the hotspots and the diffuse component would be about twice the average skeletal dose, four times the diffuse volume dose, and eight times the diffuse surface dose. The present study indicates that the effective dose is comparable to the diffuse volume dose. Therefore, there is a discrepancy of a factor of 4 between observation and prediction assuming bone volume to be the target. The observations correspond more closely to prediction assuming a surface target. The uncertainties in the comparison, however, may amount to as much as a factor of 2.

If the diffuse volume dose were exactly equal to the effective dose for Ca^{45}, then under the present interpretation it would not be the diffuse component which is producing most of the tumors. This effective dose is twice the dose delivered to bone surfaces by the diffuse component. About half of the bone surfaces in these young mice were growing at the time of

*In the foregoing "the diffuse dose" has referred to the dose delivered to the volume of bone by the diffuse component. In considering a surface target, we must distinguish between diffuse surface dose and diffuse volume dose.

injection and thus hotspots were formed. With a square dose-response curve, it can be concluded that one-eighth of the observed tumors have been induced by the diffuse component, so that most of the tumors have been induced by the hotspots during the burial process.

If it is true that the dose delivered by the Ca^{45} hotspots during the burial process is responsible for most of the osteogenic sarcomas, then our argument is not completely independent of a time-intensity factor, as outlined in step 1. The argument of step 1 would still apply if the bone volume were the target, and hence its use in the preceding argument in order to eliminate the volume as the target is consistent.

Summary

Comparison of the Ca^{45} and Sr^{90} data suggests that dose to bone mineral and to osteocytes does not contribute significantly to the induction of osteogenic sarcomas. The sensitive region appears to be irradiated only by the particles that escape from microscopic bone surfaces. These include trabecular surfaces and the walls of haversian canals, where present. (The mouse skeleton does not have haversian systems.) The depth of this sensitive region has not been determined.

Because most Ca^{45} and Ra^{226} hotspots are formed at bone surfaces that are growing at the time of injection, most of them are covered by continuing growth. Consequently, the time during which they can irradiate the sensitive region is limited.

If the volume of bone (osteocytes and bone matrix) rather than the surface had been the region sensitive to the carcinogenic effect of radiation, the observed dose distribution together with the observed dose-response relation would have yielded an effective dose of roughly eight times, not twice, the diffuse surface dose. This discrepancy appears to be significant because the errors of the method probably do not exceed a factor of two.

One may speculate that the burial of Ra^{226} hotspots reduces the effective non-uniformity of Ra^{226} distributions in man.

The shape of the dose-response curves for Ca^{45} and Sr^{90} is discussed.

References

1. Marshall, John H. and Finkel, Miriam P. Autoradiographic Dosimetry of Mouse Bones Containing Ca^{45}, Sr^{90}, and Ra^{226}. Radiological Physics Division Semiannual Report, ANL-6104 (December 1959) pp. 48-66.

2. Finkel, Miriam P. and Biskis, B. O. Acta/Union Internationale Contre le Cancer 15 99 (1959).

3. Finkel, Miriam P. Science 128 637 (1958).

4. Kamb, B. and Pauling, L. Proceedings Natl. Acad. Sci 45 54-69 (1959).

5. Finkel, Miriam P. Radiation Research Supplement 1 265 (1959).

6. Archer, V. E. and Carroll, B. E. Science 131 1808 (1960).

7. Finkel, Miriam P. Proceedings Soc. Exptl. Biol. Med. 83 494-498 (1953).

SOME CALCULATIONS OF THE NON-UNIFORMITY FACTOR IN THE INDUCTION OF BONE CANCER BY INTERNAL EMITTERS

John H. Marshall

The non-uniformity factor may be defined as the ratio of the effective dose level to the average dose level for a given distribution of radioactivity in bone. By effective dose level is meant that level of a uniform dose distribution which would produce the same incidence of bone cancer as that produced by the given non-uniform dose distribution. The non-uniformity factor is a function of the shape of the dose-response curve for each local region of bone and a function of the maximum and minimum dose values and the shape of the dose distribution.

1. Let the term dose mean either dose rate or accumulated dose so that we may concentrate on the effect of the spatial rather than any temporal non-uniformity of dose: our result should apply equally well to a consideration of dose rate or accumulated dose.

2. Furthermore, let us assume that all regions of bone described by the given dose distribution are equally sensitive to radiation; then, different regions (e.g., volume targets or bone surface targets) can be considered by specifying the dose distribution that actually applies to the given regions.

3. For simplicity let us assume that the slope of the dose-response curve can be expressed as a single power of dose within the range of doses included by the given distribution:

$$T = k\, r^n \tag{1}$$

where

T = response (such as tumor incidence)

r = dose

k = constant

n = power of dose-response curve

4. Case I. Continuous Distribution

Let the dose distribution be described as follows:

$$dV = g\, r^{-m}\, dr \tag{2}$$

where

dV = the region (volume or area) of bone with dose between r and r + dr

g = constant

r = dose

m = power of dose distribution

By proper choice of m, expression (2) can be made to fit most dose distributions fairly well.

5. Let us also characterize the dose distribution by two ratios:

$$p = \frac{\text{Maximum dose}}{\text{Minimum dose}} = \frac{r_{max}}{r_{min}}$$

$$q = \frac{\text{Minimum dose}}{\text{Average dose}} = \frac{r_{min}}{r_{av}}$$

6. Then the effective response, T_{eff}, to a dose distribution given by p, q, and m, is

$$T_{eff} = \frac{\int_{r_{min}}^{r_{max}} T\,dV}{\int_{r_{min}}^{r_{max}} dV} \tag{3}$$

7. Substituting (1) and (2) into (3) and writing the limits of integration in terms of r_{av}:

$$T_{eff} = \frac{\int_{q\,r_{av}}^{p\,q\,r_{av}} k\,r^n\,g\,r^{-m}\,dr}{\int_{q\,r_{av}}^{p\,q\,r_{av}} g\,r^{-m}\,dr} \tag{4}$$

$$T_{eff} = \frac{kg\left[\frac{r^{n-m+1}}{n-m+1}\right]_{q\,r_{av}}^{p\,q\,r_{av}}}{g\left[\frac{r^{-m+1}}{-m+1}\right]_{q\,r_{av}}^{p\,q\,r_{av}}} \tag{5}$$

$$T_{eff} = \frac{(1 - m)\, k\, q^n\, r_{av}^n\, (p^{1 - m + n} - 1)}{(1 - m + n)(p^{1 - m} - 1)} \tag{6}$$

8. Now $T_{eff} = k\, r_{eff}^n$ (according to the meaning of effective dose). Substituting into (6) and solving for the non-uniformity factor, α:

$$\boxed{\alpha = \frac{r_{eff}}{r_{av}} = q \left[\frac{(1 - m)(p^{1 - m + n} - 1)}{(1 - m + n)(p^{1 - m} - 1)} \right]^{1/n}} \tag{7}$$

9. For the given continuous distribution p, q, and m are not independent parameters. Their relation is determined by the fact that

$$r_{av} = \frac{\int_{r_{min}}^{r_{max}} r\, dV}{\int_{r_{min}}^{r_{max}} dV} \tag{8}$$

$$r_{av} = \frac{\int_{q\, r_{av}}^{p\, q\, r_{av}} g\, r^{1-m}\, dr}{\int_{q\, r_{av}}^{p\, q\, r_{av}} g\, r^{-m}\, dr} \tag{9}$$

$$r_{av} = \left(\frac{1 - m}{2 - m} \right) \frac{(q\, r_{av})^{2-m}}{(q\, r_{av})^{1-m}} \frac{(p^{2 - m} - 1)}{(p^{1 - m} - 1)} \tag{10}$$

$$\boxed{q = \left(\frac{2 - m}{1 - m} \right) \left(\frac{p^{1 - m} - 1}{p^{2 - m} - 1} \right)} \tag{11}$$

10. Expression (11) is plotted in Figure 20. Expression (7), in terms of p, q, and n is plotted in Figures 21, 22 and 23 as the "continuous distribution," m having been eliminated through use of (11). Expressions (7) and (11) describe continuous functions even though certain integral values of the parameters lead to indeterminate results. These values have either been avoided by plotting non-integral values or solved by rewriting the integrals (4) and (9).

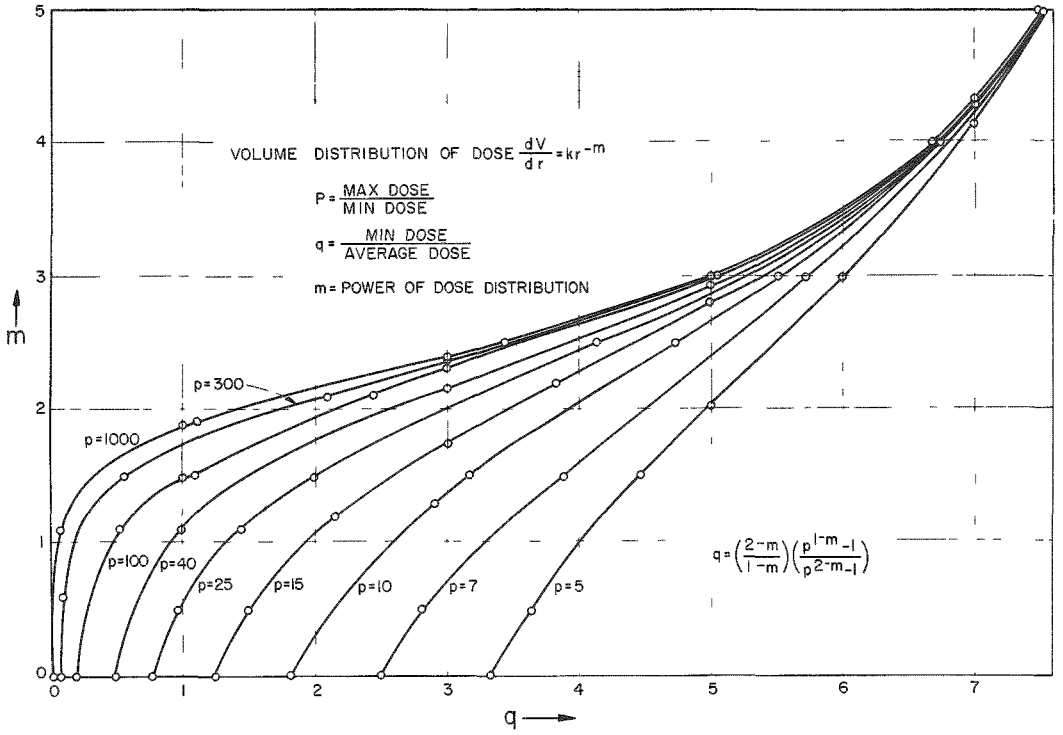

Fig. 20. Relation between parameters for a continuous dosage distribution.

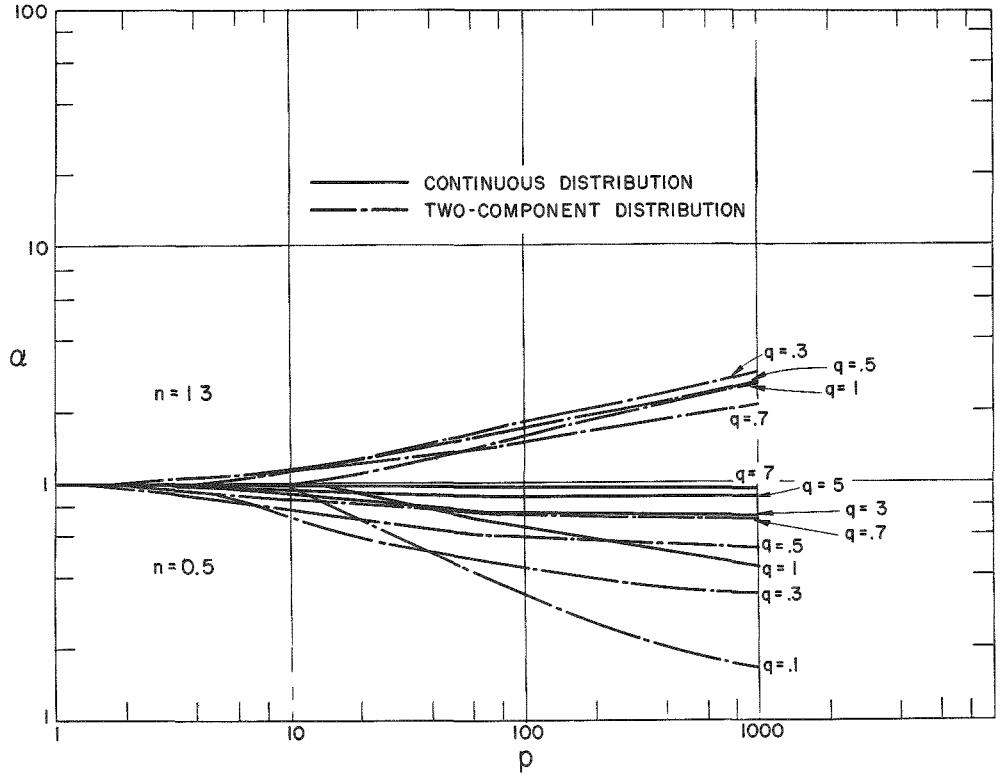

Fig. 21. Non-uniformity factor α versus maximum hotspot-to-diffuse ratio p.

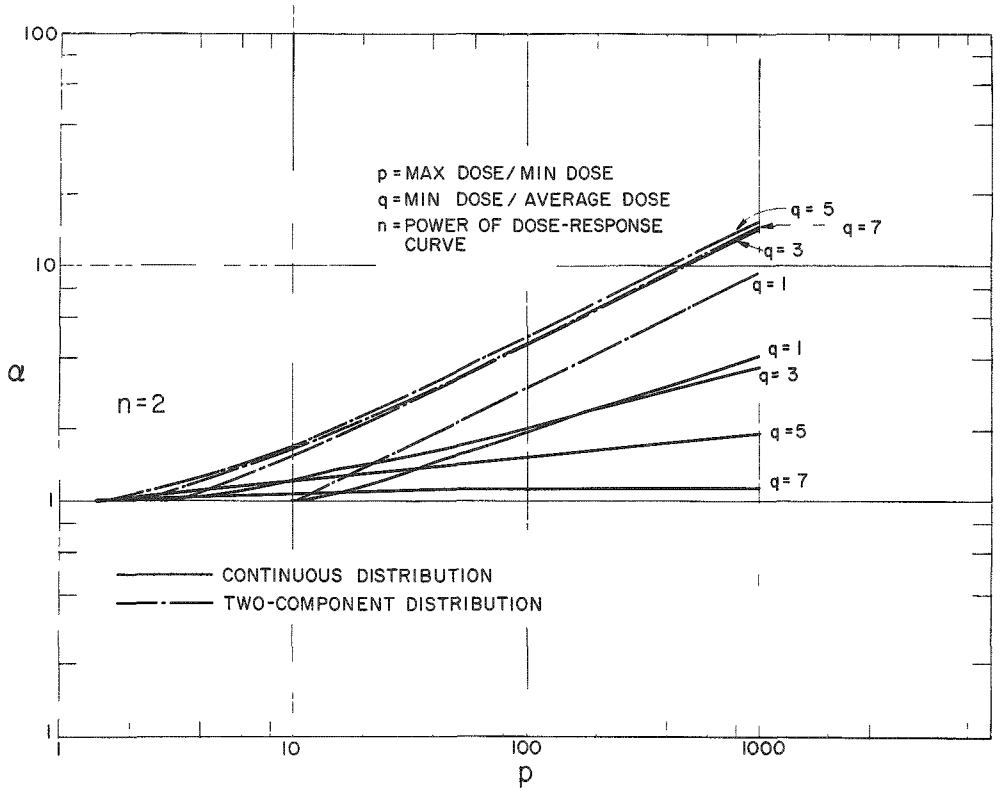

Fig. 22. Non-uniformity factor α versus maximum hotspot-to-diffuse ratio p.

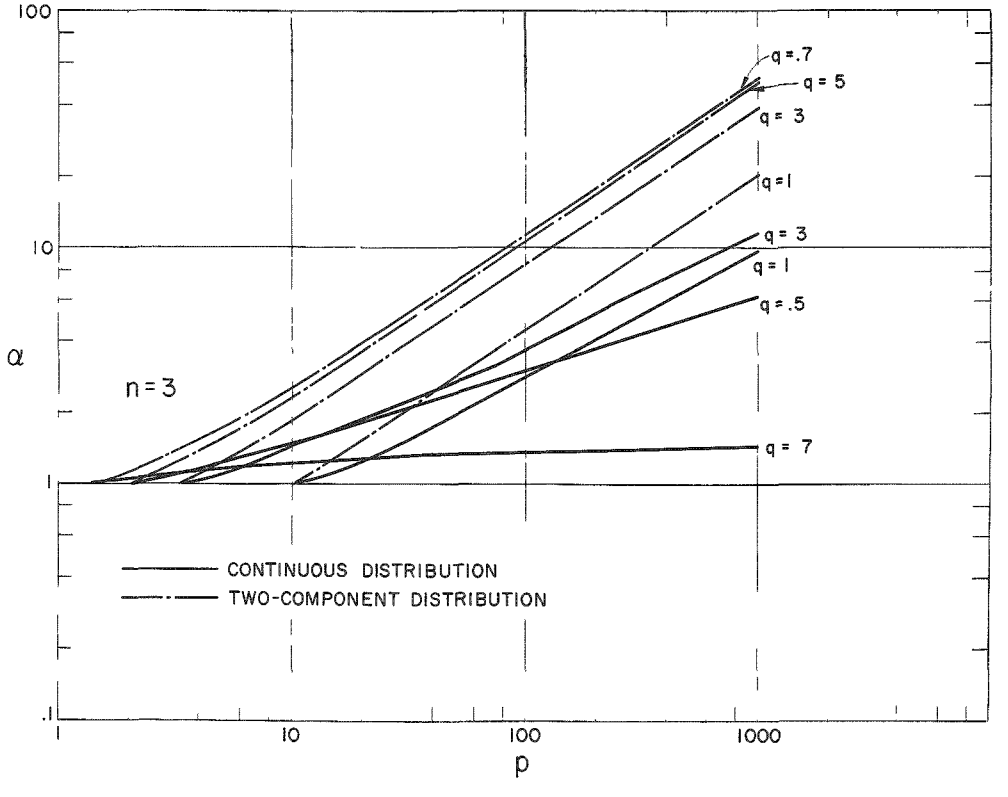

Fig. 23. Non-uniformity factor α versus maximum hotspot-to-diffuse ratio p.

11. Case II. Two-Component Distribution

The multiple-injection Elgin cases[1] show a dose distribution that is better described by just two components: a diffuse component and a hot-spot component, all the hotspots giving practically the same high dose. In this case, let a fraction x of the bone be irradiated by the diffuse component:

$$T_x = x\, k\, (q\, r_{av})^n \tag{12}$$

and the rest by the hotspots:

$$T_{1-x} = (1 - x)\, k\, (p\, q\, r_{av})^n \tag{13}$$

12. Then

$$T_{eff} = T_x + T_{1-x} = q^n\, (x + p^n - x\, p^n)\, k\, r_{av}^n \tag{14}$$

13. The relation for x in terms of p and q is given by

$$r_{av} = x\, q\, r_{av} + (1 - x)\, p\, q\, r_{av} \tag{15}$$

or

$$x = \frac{p\, q - 1}{q\, (p - 1)} \tag{16}$$

14. Substituting (16) in (14) and solving for α as before

$$\boxed{\alpha = \frac{r_{eff}}{r_{av}} \left\{ q^{n-1} \left[\frac{p^n\, (1 - q) + pq - 1}{p - 1} \right] \right\}^{1/n}} \tag{17}$$

Expression (17) is plotted in Figures 21, 22 and 23 and labelled "two-component distribution."

Discussion

The results for the non-uniformity factor α are shown as functions of p, q, and n for both continuous (r^{-m}) dose distributions and for the two-component distribution which ascribes the same dose to all hotspots. The latter distribution is interesting because it is a fairly good representation for the multiple injection radium cases, and because it yields the largest conceivable values for α with a given p, q, and n. However, no consideration of target region (bone surface or bone volume) has been included here, so that one must be careful not to use parameters p and q which have been measured for volume distributions of dose if the microscopic surfaces of bone are the sensitive regions.

The parameter q, the ratio of minimum dose to average dose, is found experimentally for volume distributions to be about 0.5. In other words, the diffuse component is usually half the uniform label.[1]

Notice that $\alpha = 1$ for $p\,q = 1$ because for these values $r_{max} = r_{av}$.

Values of n are given from 3 down to 0.5 to include the slopes shown by the mouse tumor dose-response curves. Note that $\alpha = 1$ for $n = 1$ independent of p and q, provided that (as we have assumed here) the regions of bone included within the dose distribution are equally sensitive to radiation.

Reference

1. Rowland, R. E., and Marshall, J. H., Radium in Human Bone: The Dose in Microscopic Volumes of Bone, Radiation Research 11 299 (1959).

FALLOUT TRANSPORT AS DEDUCED FROM MEASUREMENT OF GAMMA-EMITTING RADIOACTIVITY IN AIR

P. F. Gustafson* and M. A. Kerrigan*

Particulate radioactivity in air has been collected on HV-70 filters at flow rates of 25 to 30 m^3 per hour. Filters from a number of such collectors at the Argonne National Laboratory were grouped by calendar month, partially ashed, and then analyzed for gamma-emitting radioactivity by NaI scintillation spectrometry.(1)

Figure 24 shows the concentration of Cs^{137} in air from 1954 through 1957; the periodic variation in concentration is analogous to that seen in the case of Sr^{90},(2) peaking during test series and in the spring months. The spring maximum is attributed to a break in the tropopause occurring at the middle latitudes in the northern hemisphere at this time of year. Such variations tend to question the wisdom of speaking of a constant rate of fallout, at least during times of nuclear weapon tests. Figure 25 shows Cs^{137} data from January 1958 through May 1960. A spring maximum is evident in 1959 and again in 1960, truly indicating an increase in the rate of release of nuclear debris from the stratospheric reservoir at this time.

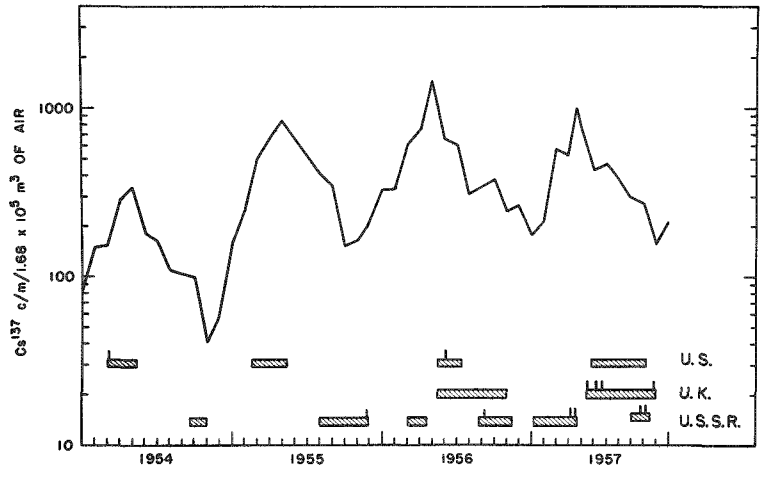

Fig. 24
Cs^{137} concentration in ground level air. Argonne National Laboratory

The time and place of origin of Cs^{137} and other nuclear debris may be determined through the use of tracers and activity ratios between the various fission products themselves. W^{181} and W^{185}, present in several shots of the United States Pacific series Hardtack I held during May through July 1958, serve to trace low-altitude stratospheric equatorial activity. Similarly Rh^{102} formed in a missile detonation at 100,000 feet over Johnston Island in August 1958 may be used to follow high altitude

*Biological and Medical Research Division.

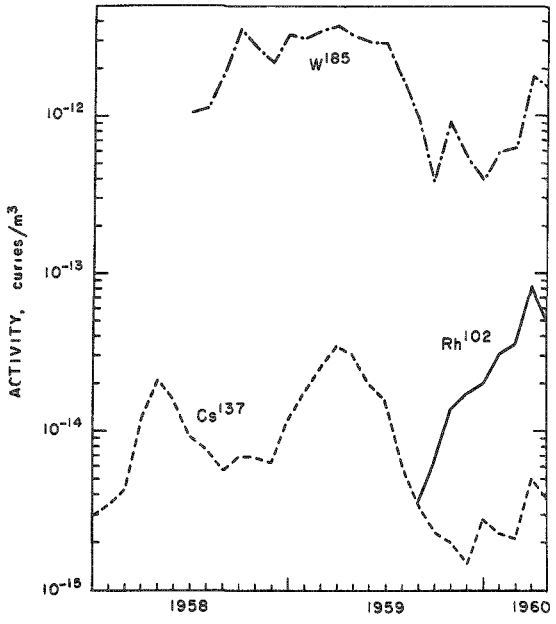

Fig. 25. Concentration of Cs^{137}, W^{185} and Rh^{102} in ground level air at Argonne National Laboratory

equatorial debris. Ground level concentration of W^{185} and Rh^{102} in air, corrected for decay back to time of production, are also illustrated in Fig. 25. Rh^{102} first became apparent at Argonne in September 1959, 13 months after production in the upper atmosphere in contrast with a delay of 1 to 2 months in the case of low-altitude W^{185}.

In the interval July to October 1958, the activity ratios of Cs^{137}, Zr^{95}, Ce^{144}, and Ru^{106} relative to W^{185} were found from the data, after first removing the activity component due to earlier tests. This was done by assuming similar shapes of air concentration curves in 1958 and 1959. The ratios thus obtained, modified for decay, were then used at subsequent times to derive the fraction of each isotope arising from Hardtack I.

An example of this procedure, showing the Zr^{95}/Cs^{137} ratio for Hardtack and non-Hardtack activity is shown in Fig. 26, covering observations from November 1958 to the present. The Hardtack ratio extrapolates to a time of origin in June 1958. That is, the Zr^{95}/Cs^{137} ratio was 140 to 1 at that time, which value is that expected at time of origin. The Zr^{95}/Cs^{137} activity ratio is quite insensitive to whether fast or thermal fission is involved and is an excellent pair to use for this reason. The non-Hardtack portion also follows a line of similar slope for a number of months, indicating essentially a single component, which extrapolates to October 1958 as time of origin and is presumably due to the large Soviet series conducted at that time. In the fall of 1959, the data depart from this line in a direction that suggests that older debris is also present. In fact, such departure coincides fairly well with the appearance of Rh^{102}.

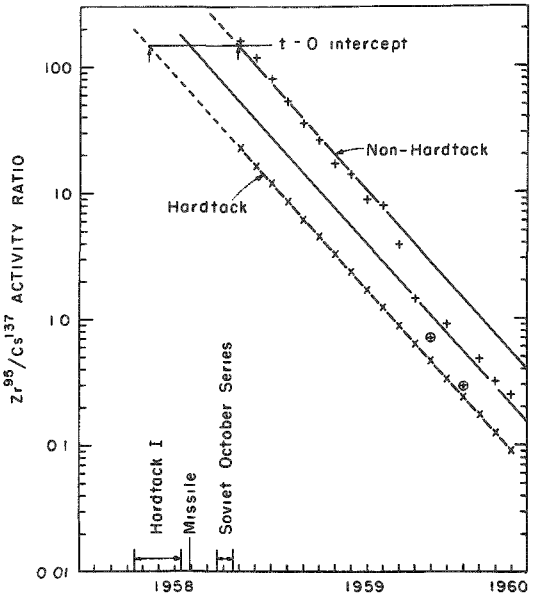

Fig. 26. Zr^{95}/Cs^{137} activity ratios. W^{185} tracer.

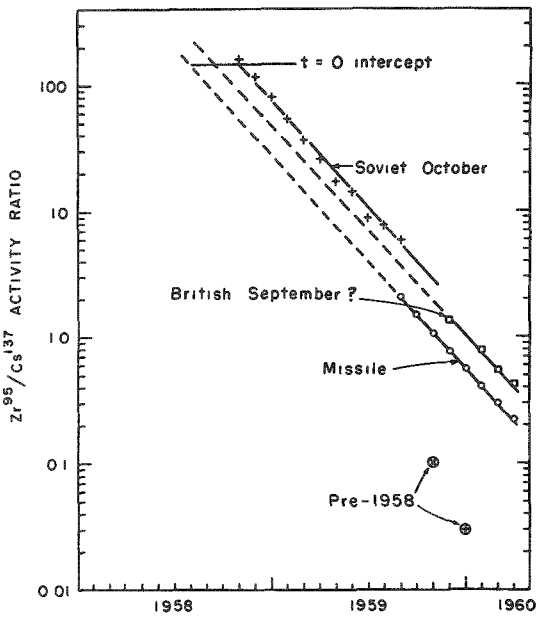

Fig. 27. Zr^{95}/Cs^{137} activity ratios. Rh^{102} tracer.

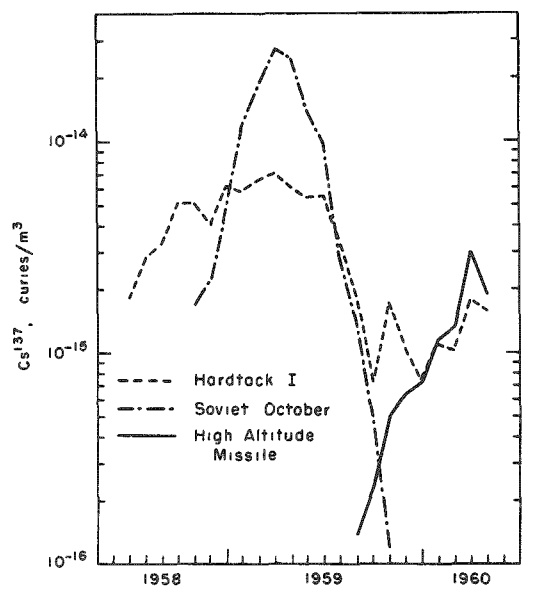

Fig. 28. Cs^{137} partition in ground level air. Argonne National Laboratory.

Obviously the thing to do is to resolve the non-Hardtack curve into Soviet and high-altitude contributions. This was done using ratios relative to Rh^{102}, analogous to the procedure employed with W^{185}. As a result, a third component becomes evident as shown in Fig. 27, presumably due to the British September 1958 tests as denoted by the extrapolation. Note also that in November 1959 and again in January 1960 debris of pre-1958 vintage was clearly evident.

We may now partition Cs^{137}, for example, into Hardtack, Soviet, and high-altitude components as shown in Fig. 28. The initial broadening of the Hardtack Cs^{137} peak may be due to tropospheric fallout from different altitudes. In the spring of 1959, 75 to 80 per cent of the air-borne Cs^{137} came from the Soviet October tests.

To the degree that ground level air is in equilibrium with the reservoir, it appears that most of the Soviet fission products released north of the Arctic Circle have been deposited within one year. From comparison of the magnitudes of the peaks of Hardtack Cs^{137} that took place in 1959 and 1960, a rough half-time for residence of 8 to 9 months, can be computed. At this time little can be said of the high-altitude debris other than that its residence time is longer than 21 months. Note the similarity in the rate of decrease shown by both Hardtack and non-Hardtack Cs^{137} following the spring break in 1959, indicating similar, if not identical pathways; since the rate of decrease is similar to that for tropospheric clearance, this tends to imply an abrupt end to large-scale dumping of stratospheric debris into the lower atmosphere.

In summary, the spring maximum in stratospheric fallout rate seems to be a real phenomenon. This causes the rate of fallout to vary seasonally. In addition, debris from different geographic locations and altitudes manifest different residence times. That from polar latitudes has the shortest residence time, and equatorial high-altitude fallout has the longest residence time.

Continued studies on fallout characteristics can be of great importance in clarifying the influence of latitude and altitude in dispersing debris if in the intervening years abstention from further testing is observed.

References

1. Gustafson, P. F., Marinelli, L. D., and Brar, S. S., Measurement of Gamma Ray-Emitting Elements Present in Soil. Radiological Physics Division Semiannual Report, ANL-5829 (February 1958) p. 136.

2. Stewart, N. G., Osmond, R. G. D., Crooks, R. N., and Fisher, E. M., The World-Wide Deposition of Long-Lived Fission Products from Nuclear Test Explosions. AERE HP/R-2354 (1957).

GAMMA-RAY STUDIES ON RADIOACTIVE FALLOUT IN SOIL

P. F. Gustafson*, S. S. Brar*, and M. A. Kerrigan*

The gross fission product radioactivity in soils from December 1959 through June 1960 has continued to decrease since the time of last reporting (November 1959).[1] Sampling, as in the past, was done in Argonne Park and west of D-202, two samples from each location, taken to a depth of 6 inches.

The Zr^{95}-Nb^{95}, Cs^{137}, Ru^{106}, and Ce^{144} activities expressed in mc/mi^2 for the period November 1959 through June 1960 are presented in Table 6. Within experimental error the concentrations of Zr^{95}, Ru^{106}, and Ce^{144} are decreasing at a rate in accord with their respective half-lives. There is an indication in March and April of short-lived fission products being present, namely Ce^{141}. Cs^{137} is remaining essentially constant within the errors of measurement. Taken at face value, these findings suggest that little or no deposition of new debris has occurred. This in turn implies that the maximum accumulated deposition of Cs^{137} (and concurrently that of Sr^{90}) has already been reached.

Table 6

Gamma ray-emitting fallout radioactivity on the ground at Argonne National Laboratory in mc/mi^2

Isotope	1959		1960				
	November	December	February	March	April	May	June
Zr^{95}-Nb^{95}*	264	200	150	112	90	80	45
Cs^{137}	186	186	198	195	197	187	191
Ru^{106}	996	1010	989	950	915	890	830
Ce^{144}	1846	1720	1590	1610	1650	1200	1280
Totals**	3556	3322	3077	2979	2942	2437	2391

*Assuming Zr^{95}-Nb^{95} to be in equilibrium

**Totals include activity due to both Zr^{95} and Nb^{95}.

*Biological and Medical Research Division.

The dose rates accompanying such fission product concentrations, computed for a point one meter above an infinite plane, and without weathering correction are given in Table 7. By June 1960, the dose rate had fallen to 1.71 μrad/hr which is 20% of the maximum dose rate of 8.46 μrad/hr computed to exist in May 1959.

Table 7

Dose rate due to fallout at Argonne National Laboratory in μrad/hr

Isotope	1959		1960				
	November	December	February	March	April	May	June
Zr^{95}-Nb^{95}*	1.68	1.27	0.95	0.71	0.57	0.51	0.29
Cs^{137}	0.47	0.47	0.50	0.49	0.50	0.48	0.48
Ru^{106}	0.85	0.86	0.84	0.81	0.78	0.76	0.71
Ce^{144}	0.34	0.32	0.29	0.30	0.30	0.22	0.23
Totals**	3.33	2.92	2.58	2.31	2.14	1.97	1.71

*Assuming Zr^{95}-Nb^{95} to be in equilibrium

**Totals include activity due to both Zr^{95} and Nb^{95}.

Reference

1. Gustafson, P. F., Brar, S. S. and Kerrigan, M. A., Radiological Physics Division Semiannual Report, ANL-6104 (December 1959). pp. 69-77.

ESTIMATION OF RADIUM BODY CONTENT OF EXPOSED HUMANS FROM THE ACTIVITY OF EXTRACTED TEETH

Charles E. Miller and J. B. Corcoran

The uncertainty in the estimate of the total body content of radium in the human skeleton by extrapolation of the radium/calcium ratio present in teeth has been investigated in a number of exposed individuals whose total body contents of radium have been measured with the Human Spectrometer and whose teeth were available for study.

The Ra(B + C) in each set of teeth from five subjects was measured by γ-ray spectroscopy after having been sealed in glass for at least 30 days. Their calcium content was estimated by weighing the teeth without fillings and by assuming that calcium constituted 28% of the total weight. The resultant specific activity (microcuries of radium per gram of calcium) was multiplied by 1,000 (the weight of calcium in the average skeleton) to determine the total body content. These data, as well as the total body content as measured with the Human Spectrometer, are shown in Table 8.

The data obtained from the first five subjects listed in the table will be discussed first. It will be seen from the table that the body contents thus calculated may differ by a factor of as large as five from that obtained by precise whole body measurements. The spread drops to a factor of two if the fourth and fifth subjects are disregarded.

The circumstances surrounding these two subjects which yield the largest errors are probably indicative of the conditions which must be investigated when evaluating such data from teeth. The tooth obtained from subject 03-473 was a third molar (wisdom tooth) which was growing during the time that she was painting watches, namely at 19 to 21 years. This fact is substantiated by an autoradiograph made by R. E. Rowland[1] who found that a hot band in the dentine contained a concentration of radium to calcium 176 times as high as the concentration present in the rest of the dentine. Hence teeth which are forming during the period of radium ingestion will probably yield total body values which are abnormally high. Subject 03-559, on the other hand, was occasionally given radium as a child. This tooth yields a value which is low by a factor of 3.2 indicating that there was remodeling in the tooth, or that the tooth was very small at the time the radium was accumulated. It should be noted that the teeth measured in the first three cases were incisors and molars which were probably formed before these individuals acquired radium at ages which varied from 15 years to 24 years of age.

TABLE 8

Estimated radium body content from the activity of extracted teeth

Subject	Route of intake and type of exposure	Age during exposure, years	Number of teeth assayed	Type of teeth	Weight of teeth, g	Amount of Ra^{226}, curies	Radon Retention, %	Ra^{226} body content calculated from teeth activity, curies	Measured Ra^{226} body content, curies	Radium-calcium ratio body/teeth
03-487*	Oral, dial painter	17-19, 21-25, 27-30 (17-18)	1	molar	1.67	2.1×10^{-10}	0.44	4.5×10^{-7}	3.3×10^{-7}	0.69
03-594	Oral, dial painter	24-29	7	5 incisors 2 molars	9.87	4.6×10^{-10}	0.66	1.64×10^{-7}	1.13×10^{-7}	0.69
03-571	Oral, dial painter	15	1	incisor	0.708	1.13×10^{-10}	0.34	5.7×10^{-7}	1.1×10^{-6}	1.93
03-473	Oral, dial painter	19-21	1	third molar (wisdom tooth)	1.2	2.1×10^{-9}	0.75	6.3×10^{-6}	1.2×10^{-6}	0.2
03-559	Unknown (not a dial painter	unknown	1	premolar	0.77	2.15×10^{-10}	0.32	1×10^{-6}	3.2×10^{-6}	3.2
03-532	Oral, dial painter	16-20	4	1 premolar 2 incisors 1 canine	3.646	2.5×10^{-11} Ra(B + C)	0.35 (assumed)	7×10^{-8}	9.7×10^{-8}	≤ 1.39
03-595	Oral and bronchial (radium chemist)	22-37	1	premolar	1.02	4.7×10^{-11} Ra(B + C)	0.35 (assumed)	4.7×10^{-7}	5×10^{-7}	≤ 1.06
03-516*	Oral, dial painter	14-18, 21-23 (14-15)	11	9 incisors and canine 1 premolar 1 molar	8.27	3.1×10^{-11} Ra(B + C)	0.35 (assumed)	3.8×10^{-8}	1.8×10^{-8}	≤ 0.47
03-588*	Oral, dial painter	18-20 (18)	1	incisor	0.63	not detectable		$<10^{-8}$	5.6×10^{-8}	<0.47

*Although this individual was employed for several years, information available demonstrates that radium was ingested mainly during the years shown in parentheses.

The fact that the radon retention of these teeth varied from 32% to 75% is surprising. The measurements on the tooth which yielded 75% retention were repeated, resealing and all, and identical results obtained. The cause of this unusual retention is unknown.

On the teeth from four other subjects only a single measurement was made shortly after sealing without attaining equilibrium radon growth. The Ra(B + C) content has been multiplied by 0.285 (on the assumption that 35% of the radon is retained in the tooth) to obtain the Ra^{226} content. The body contents thus calculated for three of these subjects, (lines 6, 7, and 8) fall within a factor of 2 of the measured values. The Ra(B + C) content of the tooth from the ninth subject was below the detection sensitivity of the gamma-ray spectrometer.

In general, these findings are in agreement with the experience at Massachusetts Institute of Technology. It is believed that most of the discrepancy is due to differences between dental and skeletal metabolic rates, and only in minor part to differences in the calcium contents in the two mineral systems.

Conclusions

Teeth alone should not be used to determine total body content of radium in humans acutely exposed when specimens of bone are available; the data from teeth should be used only within limits if no more suitable material is at hand. The body content calculated from teeth will possibly fall within a factor or two of the correct value if the teeth which are analyzed had already completed growth at the time the radium was acquired. Since radon retention may vary substantially and add to the uncertainty, assumptions as to its value should be avoided.

Reference

1. Rowland, R. E. The Radium Distribution in the Tooth of a Dial Painter. Radiological Physics Division Semiannual Report, ANL-6104 (July through December, 1959). pp. 30-33.

FACTORS DETERMINING THE ULTIMATE DETECTION SENSITIVITY OF GAMMA SCINTILLATION SPECTROMETRY*

Harold A. May and L. D. Marinelli

Introduction

The choice of the crystal size in gamma-ray spectrometry has frequently been made on the basis of intuition, advice of more knowledgeable friends or acquaintances, availability or cost, and only rarely on a rational evaluation of the physical factors involved and the empirical data or theoretical helps available. We shall attempt, in this paper, to outline a semi-analytic approach to the choice of optimum crystal size as a function of gamma energy in the range of 200 kev to 2.6 Mev. Empirical data relative to a practical system will be reviewed, and the maximum sensitivity for a typical situation will be calculated.

Optimum Crystal Size

Calculation of the pulse-height spectrum of sodium iodide crystals by Monte Carlo methods was first reported by Berger and Doggett.[1] A more complete consideration of all the physical processes involved, in a computer program developed by Miller and Snow at Argonne National Laboratory,[2] results in agreement of calculated with available experimental spectra within a few percent. This program evaluates the interaction ratio, F, defined as the fraction of gamma rays striking the crystal face which interact, with the release of an electron, and thus produce a pulse; one also obtains the photofraction, denoted by γ, which is that fraction of the interactions in which all of the energy of the incident gamma ray is expended within the crystal, with the result that the pulses fall in a single energy peak denoted - though inaccurately - as the photopeak. For a fixed crystal size and a given γ-ray energy, the interaction ratio is found to depend markedly upon source placement, as illustrated in the upper part of Fig. 29; the photofraction (shown below in the figure) is essentially independent of geometry.

For our purposes the computed pulse height distribution may be represented, to a rather good approximation by two rectangular areas, as shown in Fig. 30. The width of the area S can be taken as:

$$\Delta E_\gamma = \eta E_\gamma \qquad (1)$$

---

* To be published in Proceedings of the Total Absorption Gamma-Ray Spectrometry Symposium, Gatlinburg, Tenn. May 10-11, 1960.

where η is the "resolution" as commonly defined; S represents the total counting rate in the whole energy peak, not that observed within a channel width of $\Delta E\gamma$ at $E\gamma$. The latter, assuming a Gaussian distribution, would be only 0.76 S.

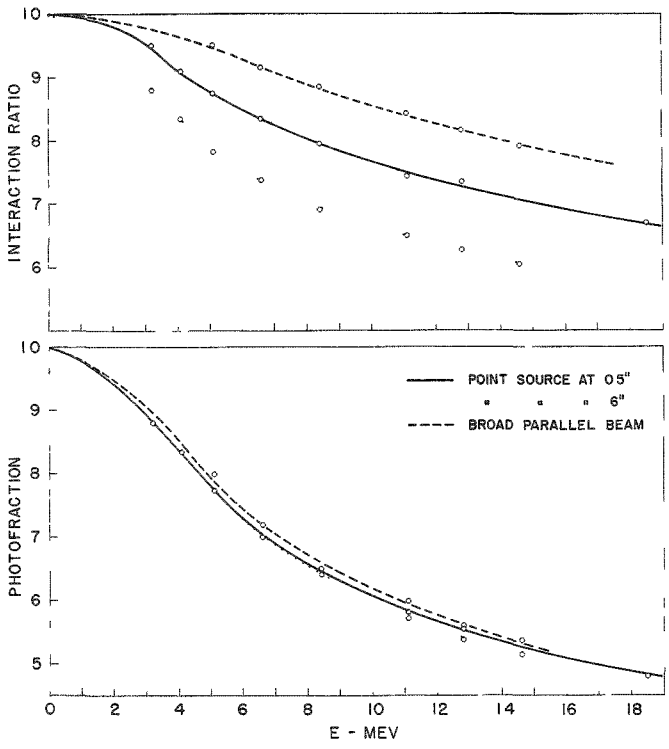

Fig. 29.
Interaction ratio (F) and photofraction (γ) as a function of source geometry.

Fig. 30.

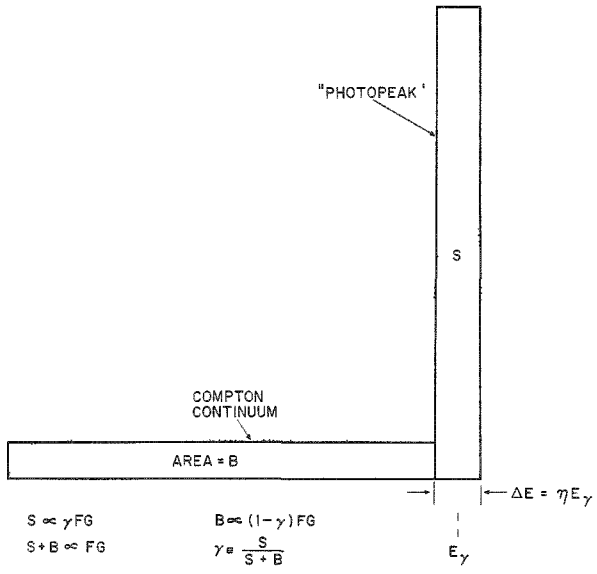

We now express the counting rates of S and B in terms of the calculated crystal parameters as follows:

$$\gamma = S/S + B \tag{2}$$

$$S + B = \epsilon F G \tag{3}$$

$$S = \epsilon F \gamma G \tag{4}$$

$$B = (1-\gamma) \epsilon F G \tag{5}$$

The correction factor ϵ accounts for absorption and scattering in the crystal can, back scattering from the phototube, and other departures from the idealized crystal assumed in the computer program. The constant G is a geometrical factor expressing the ratio of gamma rays emitted to those actually striking the crystal.

Calculations have been made for crystal diameters of 2, 4, 6, 8, 12 and 16 inches and thickness ranging from 1 to 8 inches, at energies of 0.279, 0.661, 1.33 and 2.62 Mev. The geometry chosen was a point source 18 inches from the crystal face, this being the average distance to the median line of a subject seated in the standard chair position of our whole body counter.[3] Thus

$$G = \Omega/4\pi = \tfrac{1}{2}\left[1 - \frac{18^2}{18^2 + r^2}\right] \tag{6}$$

(Ω = solid angle subtended by the crystal, r = the crystal radius), and the factor ϵ was taken to be unity. The point source is a poor approximation for our particular case, and the numerical values given below are for this particular geometry only. Yet, they represent a fairly typical case, and the conclusions reached are believed to be applicable to most single crystal counting situations.

Figure 31 depicts the fraction of gamma rays emitted into 4π solid angle, which strike the crystal and produce counts in the photopeak, as given by the product $S = F \gamma G$. The additional parameter is energy in Mev. The increase in the value of S as the crystal diameter is increased from 2 inches to 12 inches reflects mostly the increased solid angle. The curves readily show, as one could rather easily deduce from known interaction cross sections, that little is to be gained in absolute counts under the photopeak beyond a two-inch-thick crystal at 279 kev, and 6 inches at 2.62 Mev.

For an economic figure of merit, since price is sensibly proportional to the amount of sodium iodide, the numbers used above were divided by r^2h (the constant factor π being neglected for convenience), thus normalizing to unit volume of NaI. The resulting variation in S/r^2h with thickness is shown in Figure 32.

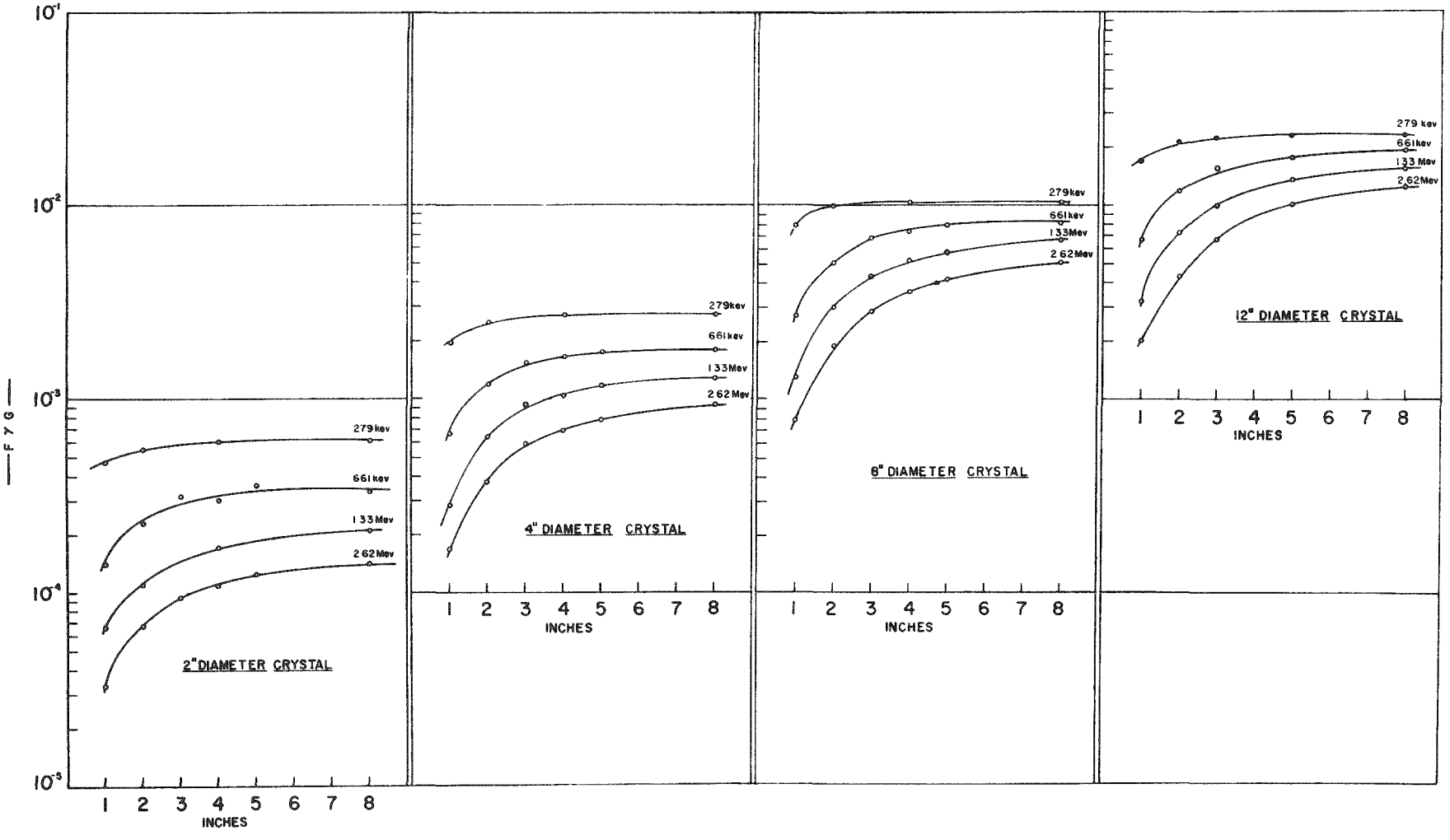

Fig. 31. Fraction of gamma rays emitted which are detected in "Photopeak" vs thickness in inches.

GEOMETRY: Point source at 18"

The optimum thickness is three inches at 2.62 Mev, two inches at 1.33 Mev, and less than one inch at the lower energies. Judged solely by this criterion, any mass of sodium iodide beyond these thicknesses might better be utilized to increase the crystal diameter, and hence the geometrical factor.

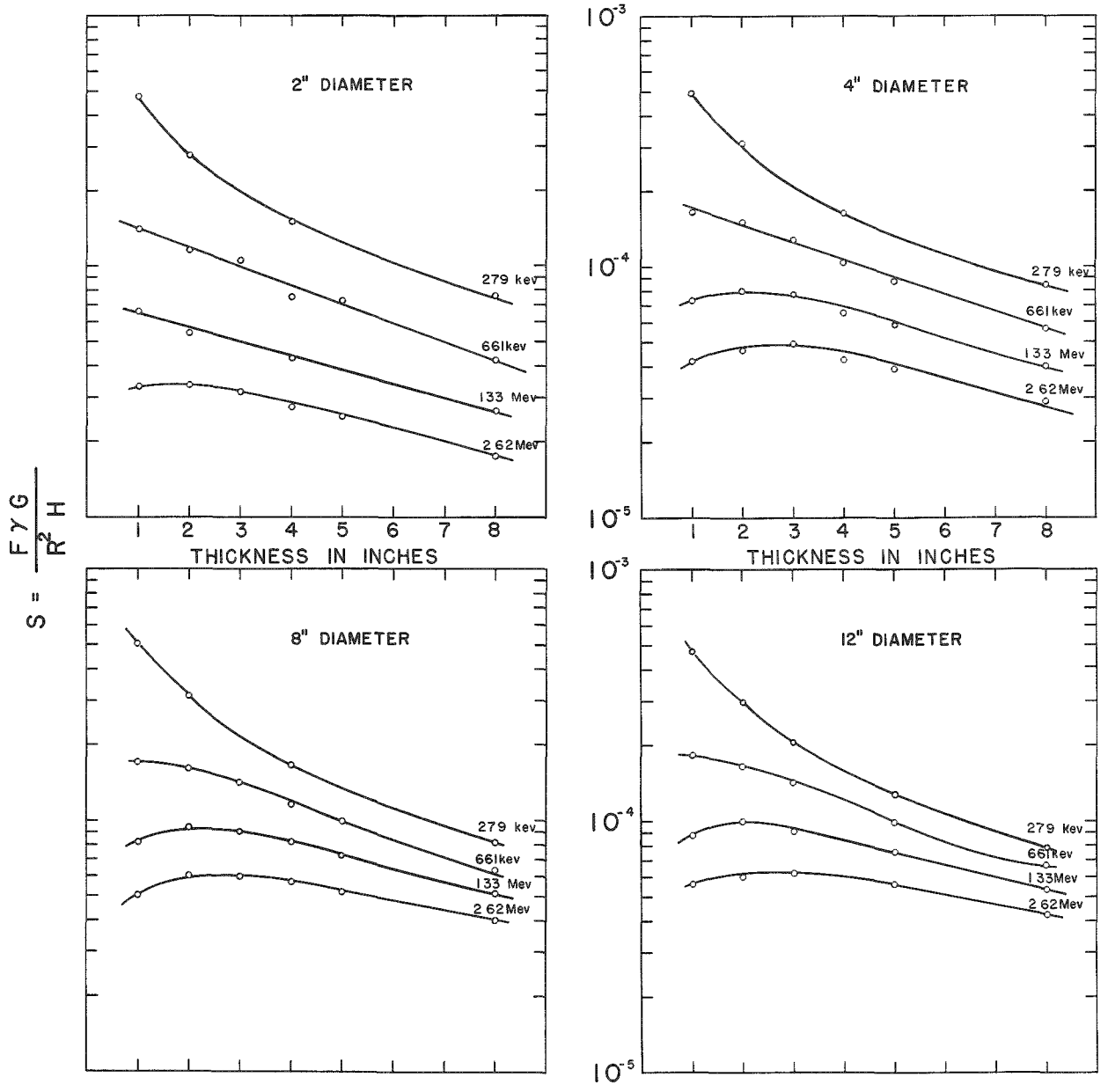

Fig. 32. Fraction of gamma rays emitted which are detected in "Photopeak," per unit volume vs thickness in inches.

However, other considerations also affect the selection of optimum size, principally the poorer resolution of the thinner large diameter phosphors. As has been pointed out by P. R. Bell,[4] the rear portion of a crystal, i.e., that thickness in excess of the optimum dimensions determined by energy, acts principally as a light pipe, smoothing out the statistical fluctuations in light collection and transfer, and minimizing the effects of the photocathode non-uniformity. On the other hand, use of a Lucite or Vycor light pipe should be considered, for it results in savings in cost and in background counts since a clean light pipe could absorb radiation emitted by the phototube. Multiple tube operation becomes necessary if best resolution is to be attained, and up to seven three-inch tubes have been employed on a $9\frac{1}{2}$-inch diameter crystal, with which resolutions slightly better than 10% at the Cs^{137} line have been routinely observed. However, since phototube contribution to the natural background is roughly proportional to the number of tubes employed, the use of large crystals is not without inherent difficulties, and frequently some compromise between these conflicting demands must be made.

Next let us consider the ability of a spectrometer to detect one gamma energy in the presence of another, more intense line. Such is the case of measuring mixed fission products in living animals in the ubiquitous presence of the normal K^{40}, or in the analysis of other complex spectra. We may consider a typical situation as in Figure 33, where S_1 and B_1 are the photopeak and continuum of the gamma ray, of energy E_1, to be measured in the presence of an interfering gamma line n times as strong, which contributes a background B_2.*

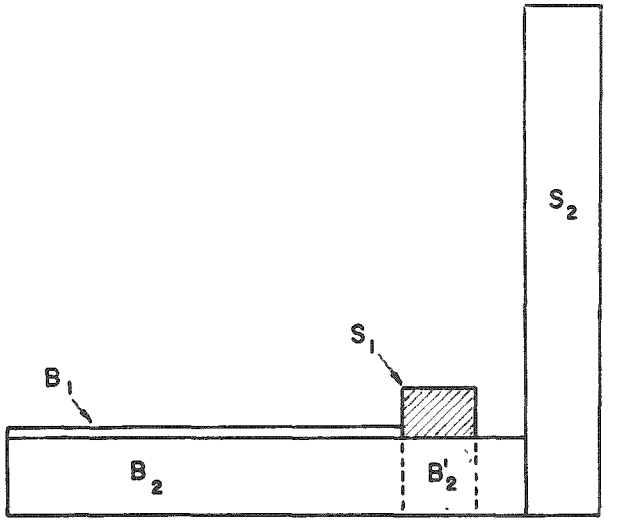

$$B_2' = \frac{\Delta E}{E - \Delta E/2} \cdot B_2 \simeq \frac{\Delta E}{E} \cdot B_2$$

$$S_2 = nS_1; \quad B_2 = nB_1 \text{ (i.e. } \gamma_2 = \gamma_1)$$

$$\frac{S_1^2}{2\,B_2' + S_1} \simeq \frac{S_1}{n\eta} \cdot \frac{\gamma}{2-\gamma}$$

Fig. 33

* It is assumed that no gamma rays are emitted in cascade, so that corrections for the sum peak spectrum, which can be extremely bothersome,[5] are not required.

In the comparison of counting systems, the reciprocal of the relative standard error attainable in a given counting time has been frequently used as a figure of merit (f.o.m.);[6] this may be expressed as $S^2/(2B+S)$. If one counts in a band of width ΔE_1 at E_1, then the interfering background from B_2, as indicated in the figure by the dotted portion B_2', is just

$$B_2' = \frac{\Delta E_1}{E_2 - \frac{1}{2}\Delta E_2} B_2 \cong \frac{\Delta E_1}{E_2} B_2 = \frac{\eta_1 E_1 B_2}{E_2} \tag{7}$$

from which, since

$$B_2 = \frac{n(1-\gamma_2) F_2}{(1-\gamma_1) F_1} B_1 \tag{8}$$

it follows [from equations (4) and (5)] that

$$\text{f.o.m.} = \frac{S_1^2}{2B_2' + S_1} = \frac{S_1 \gamma_1 F_1}{2n\eta_1 E_1/E_2 (1-\gamma_2) F_2 + \gamma_1 F_1} \tag{9}$$

This expression contains too many parameters to permit much insight into its meaning. One should note, however, that in principle it is possible to reduce this to a function of three independent variables, E_1, E_2, and n. A particularly simple case is that in which $E_1 = E_2$, so that equation (9) reduces to

$$\text{f.o.m.} \cong \frac{S_1 \gamma}{2n\eta(1-\gamma) + \gamma} \tag{10}$$

For the case $n \cong 1/\eta$ a further simplification is possible, namely:

$$\text{f.o.m.} \cong \frac{S_1 \gamma}{2 - \gamma} \tag{11}$$

This figure of merit is shown in Fig. 34., again normalized per unit volume of NaI. The curves are roughly similar to the previous ones, with definite maximum appearing in the 661-kev curve. The optimum thicknesses on the 1.33- and 2.62-Mev curves are approximately doubled. This is a quantitative indication of the well-known practical advantages resulting from improvement in photofraction obtained with increased crystal thickness. The optimum crystal thickness also depends upon the dimensionless quantity $n\eta$. At 1.33 Mev, it varies from 3 inches at $n\eta = 0.25$ to 4.5 inches at $n\eta = 4.0$. However, since the maxima in Fig. 34 are broad, it is apparent that this dependence has little practical significance.

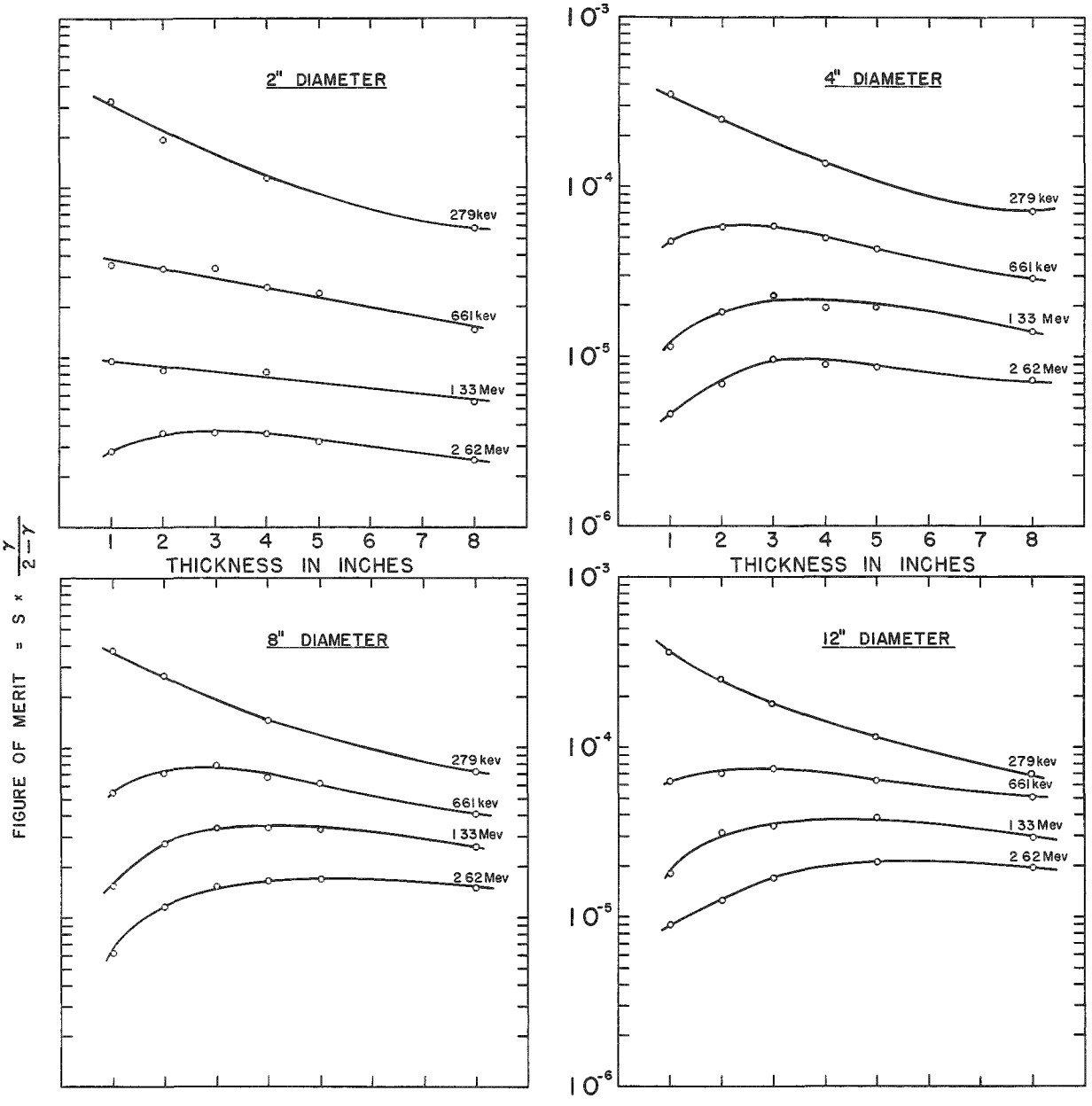

Fig. 34. Figure of merit for detection of one photopeak in the presence of another $= \frac{F\gamma G}{R^2 H} \cdot \frac{\gamma}{2-\gamma}$

Minimum Detectable Activity

In many situations it is the natural background which determines the minimum detectable signal. The sources of this background have been thoroughly discussed elsewhere,[3] and will not be dealt with in detail here. These sources will vary from one installation to another, depending upon

the amount of residual radioactivity in shielding materials, phototubes, crystal and package, and upon the altitude of the laboratory. Hence no general expression for the natural background, or its dependence upon crystal size, can be given. Instead, we consider a particular installation as typical of what may be achieved if reasonable care is taken in the selection of components.

A 7-inch diameter by $3\frac{1}{2}$- inch crystal in use at Argonne National Laboratory, when placed in an 8-inch thick Fe cave lined with $\frac{1}{8}$-inch Pb, having inside dimensions of 15" x 15" x 27", has an average integral background of 455 cpm between 25 kev and 1.57 Mev. It is estimated that the origin of about 82% of these counts may be accounted for, as follows:

Fe shielding	75 cpm	16%
Cosmic radiation	155 cpm	34%
P M tube	120 cpm	26%
Crystal assembly	30 cpm	6%

Total 380 cpm, or 82% of known origin.

The uncertainties in some of these values cannot be evaluated altogether by counting statistics, but are believed to be about ± 10%.

Pulse height spectra over this energy region are shown in Fig. 35 for the equipment located in our Laboratory (solid line), and in a tunnel 250 feet underground, where the cosmic-ray component was eliminated (dotted line).

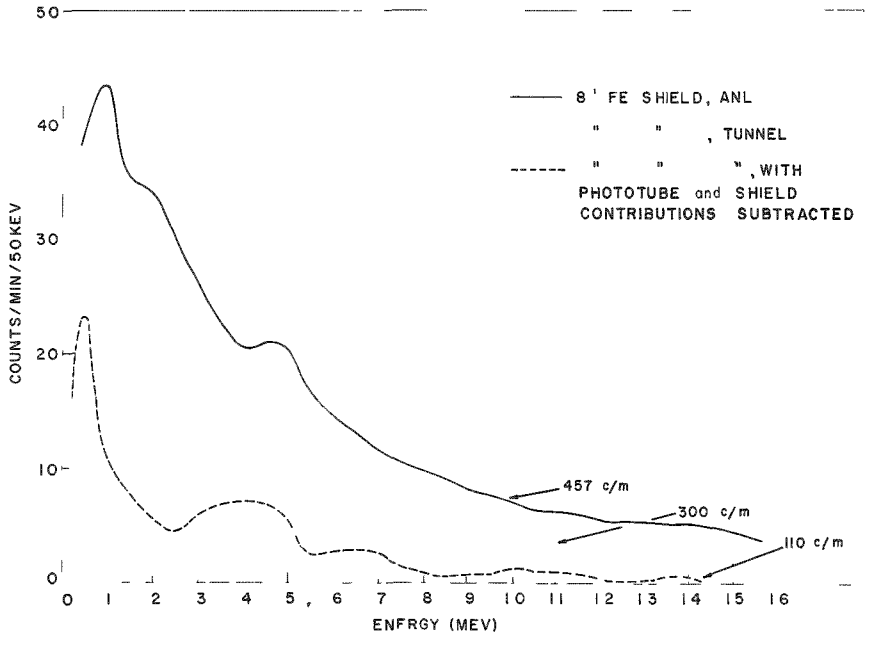

Fig. 35. Background spectra - 7" x $3\frac{1}{2}$" crystal; one 6364 tube

If the first three listed components are subtracted from the upper curve, the lowest spectrum results, representing an upper limit to what should be achievable with presently available techniques.

We now determine the minimum amount of activity which may be quantitatively measured with this system, assuming a point source on the crystal surface. If the rather arbitrary assumption is made that the net signal S(cpm) shall be known within ± 20%, i.e., $S = 5\sigma_s$, then

$$(S + B) - B = 5\sqrt{\frac{B}{t} + \frac{B + S}{t}} \tag{12}$$

which becomes

$$S = 5\sqrt{2B/t} \tag{13}$$

Since the background rate B and signal plus background S + B are nearly the same, we have assumed equal counting times. It follows that the measurable activity A, expressed in $\mu\mu$ curies, is given by

$$A = \frac{5\sqrt{2\,B/t}}{1.11\,F\gamma\epsilon g} \tag{14}$$

where g is the number of gamma rays of energy E which are emitted per disintegration, and the other symbols as already defined.

The variation of ϵ with energy was estimated from experimental data with three sources of known strength. It is, admittedly, the least well known of the factors in equation 14. We choose to count in a channel width $\Delta E = 1.7\,\eta\,E$, in order to include the entire photopeak, as determined by measurements of resolution versus energy. B was then determined from the solid curve of Fig. 35, namely from the background at our Laboratory. Values of A, as calculated for counting times of 30, 100, and 1000 minutes, are shown in Fig. 36. The curves are seen to be practically flat between 0.3 and 1.6 Mev, due to the fortuitous way in which the energy dependence of the several factors is combined. Similar calculations were also made for a "minimum attainable background," represented by the lowest curve in Fig. 35. The results were essentially one half the corresponding plotted values, as could have been anticipated roughly from the fact that the lowest attainable background with this crystal is about one fourth of that at ANL.

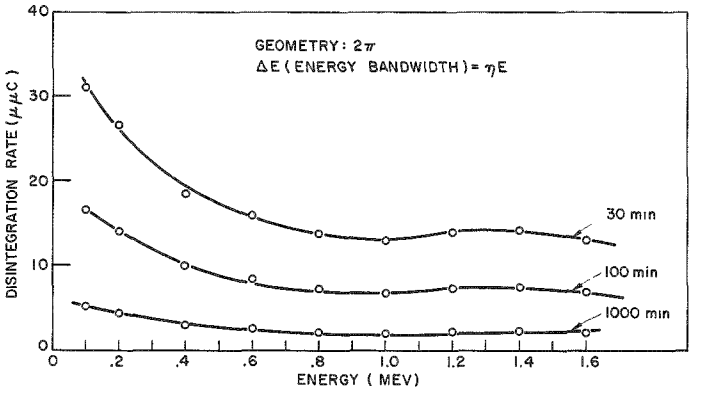

Fig. 36.
Minimum detectable activity of 7" x $3\frac{1}{2}$" crystal, in 8" Fe cave at Argonne

References

1. Berger, M. J. and Doggett, J., Rev. Sci. Instr. 27 269 (1956); see also J. Res. Natl. Bur. Stds. 56 355 (1956).

2. Miller, W. F., Reynolds, J., and Snow, W. J., Rev. Sci. Instr. 28 717 (1957); also Miller, W. F. and Snow, W. J., Rev. Sci. Instr. 31 39 (1960).

3. Marinelli, L. D., Miller, C. E., May, H. A., and Rose, J. E., in Advances in Biological and Medical Physics, Vol. 8, New York; Academic Press, in press.

4. Bell, P. R., in Beta and Gamma Ray Spectroscopy, K. Siegbahn, ed., New York: Interscience Press, 1955, p. 145.

5. Lazar, N. H., IRE Trans. Nucl. Sci. NS-5 (No. 3) 138 (1958).

6. Freedman, A. J., and Anderson, E. C., Nucleonics 10 (8) 57 (1952).

I. STUDY OF RADIUM-226 CONTENT OF MIDWEST WATER SUPPLIES

Henry F. Lucas, Jr.

In previous work, water from certain midwest municipal water systems was found to contain less than 0.03 to 37 $\mu\mu$g/l. of Ra^{226}, concentrations which correlate well with source type and method of softening. Water derived from surface sources such as rivers or lakes, wells penetrating unconsolidated sand or gravel deposits of glacial origin, limestone formations of Silurian or Devonian age were, with rare exception, found to contain less than 1 $\mu\mu$g/l. of Ra^{226}. In contrast, wells penetrating deep sandstone formations of Ordovician, Cambrian or Pre-Cambrian ages had Ra^{226} contents from 1 to 37 $\mu\mu$g/l.[1,2]

These deep sandstone formations are known to exist over an area not less than 300,000 square miles in extent.[3] In a portion of this area the quality and quantity of the water is suitable for drinking and other municipal purposes. The broken line in Fig. 37 outlines the two largest areas in the United States obtaining water from consolidated rock (limestone and deep sandstone) formations.[4] This area is seen to cover much of Wisconsin, Minnesota, Iowa, Illinois, and Missouri.

As part of an extensive study of the Ra^{226} content of municipal drinking waters in these and adjoining regions, the study of Illinois is complete, with at least one water sample collected and analyzed from 163 of the 165 communities comprising more than 99% of the total population suspected of consuming water with high radium content.

The distribution of the samples and the range of Ra^{226} content is shown in Fig. 37. On this map, the color of the pin corresponds to the range of Ra^{226} content in the drinking water. The grey, black, black with white dot, and black with white cross correspond to a range of Ra^{226} content of 0-1, 1-4, 4-10, and 10-37 $\mu\mu$g/l., respectively.

With two exceptions, concentrations of Ra^{226} in excess of 4 $\mu\mu$g/l. have been found thus far only in Illinois, Iowa, and Wisconsin. Cities having Ra^{226} content greater than 10 $\mu\mu$g/l. in their water supply have been found, thus far, only in Illinois, Iowa, and Missouri, and their total population is about 37,000 (1950 census). The total population identified to date consuming water in excess of 1 $\mu\mu$g/l. is 1,000,000. Of these, about one half or 480,000 consume water having a Ra^{226} content in excess of 4 $\mu\mu$g/l., a level leading to a whole-body radium content presently estimated to be at least 5 times that obtainable from normal food alone. The data are summarized in Table 9.

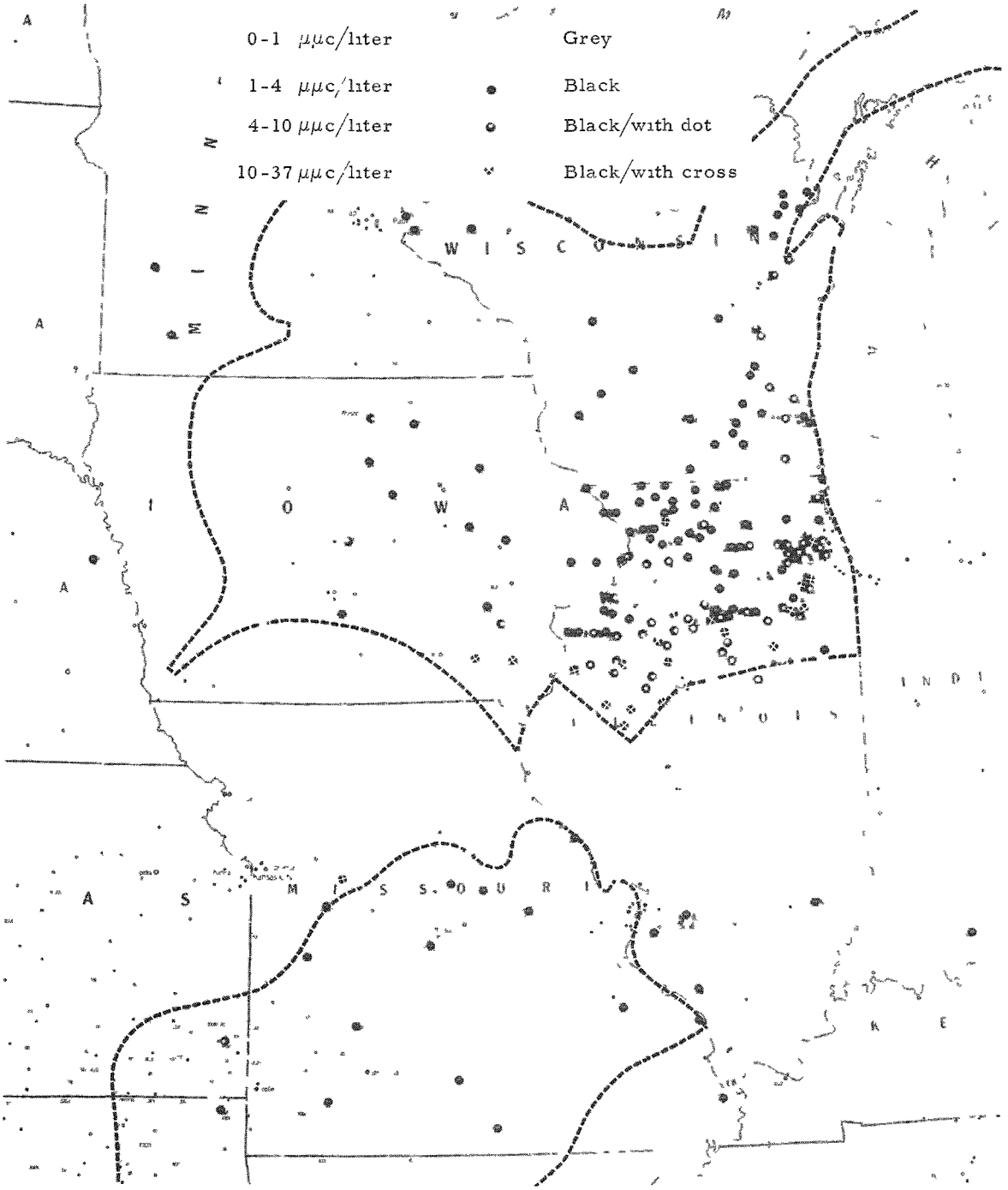

Fig. 37. Ra^{226} content of municipal drinking water

Table 9

Summary of populations consuming water at various ranges of Ra^{226} content

	Ra^{226} $\mu\mu g$/liter	Number of cities	Total population*
Illinois	0.0 - 0.9	131	1,035,414
	1.0 - 3.9	56	248,248
	4.0 - 9.9	41	320,508
	>10. <37	19	30,261
Iowa	0.0 - 0.9	16	156,914
	1.0 - 3.9	10	43,855
	4.0 - 9.9	4	38,716
	>10. <11.7	1	5,843
Missouri	0.0 - 0.9	32	155,830
	1.0 - 3.9	14	81,314
	4.0 - 9.9	0	0
	>10. <10.4	1	1,218
Wisconsin	0.0 - 0.9	28	196,722
	1.0 - 3.9	25	221,175
	4.0 - 9.9	8	81,740
	>10.	0	0
Total	0.0 - 0.9	207	1,544,880
	1.0 - 3.9	105	595,108
	4.0 - 9.9	53	440,964
	>10.	21	37,322
Grand total		386	2,617,418

*1950 Census

References

1. Lucas, H. F., Jr., and F. H. Ilcewicz. J. Am. Water Works Assoc. 50 1523-1532 (1958).

2. Lucas, H. F., Jr. Radiological Physics Division Semiannual Report, ANL-5919 (September 1958) pp. 58-60.

3. Meinzer, O. E. Occurrence of Ground Water in the United States. USGS, Water Supply Paper No. 489, Govt. Printing Office (1923).

4. McGuinness, C. L. The Water Situation in the United States with Special Reference to Ground Water, USGS Circular No. 114, Fig. 17, p. 90 (1950).

Ra^{228} (MESOTHORIUM I) IN MIDWEST WELL WATERS

Douglas P. Krause

Concurrent with the program to determine the Ra^{226} concentration levels in well waters from the midwestern states of Illinois, Wisconsin, Missouri, and Iowa, measurements of the Ra^{228} (mesothorium I) levels are also being made.(1-4) Waters were selected having Ra^{226} levels equal to or greater than 4 $\mu\mu$c/liter, and these, without exception, were obtained from wells penetrating deep sandstone formations. Although no definite pattern can be established, it appears that in Illinois certain areas yield reasonably constant ratios of Ra^{228}/Ra^{226}, but that throughout the state this ratio varies from 0.04 to 2.4 and is dependent upon the aquifer or aquifers from which the water is drawn.(5) Previous work on samples from other than deep sandstone wells has shown that the Ra^{226} and Ra^{228} concentrations are low or nearly equal, i.e., the Ra^{228}/Ra^{226} ratio approaches unity.(3)

The data for some Illinois deep sandstone wells are presented in Table 10 and are tabulated by ascending values of the Ra^{228}/Ra^{226} ratio. The table also classifies the wells as to the type of aquifer from which the principal supply is believed to be drawn. The information regarding the wells was taken primarily from Bulletin No. 40 of the Illinois State Water Survey and from the sampling record sheet completed by the local water department.(6)

It is evident from Table 10 that waters derived chiefly from St. Peters sandstone (Ordovician system) are generally low in Ra^{228} but high in Ra^{226}, whereas waters derived from the underlying Galesville sandstone formation (Cambrian system) have more nearly equal concentrations of the two isotopes. In each case, however, there are exceptions to these general statements, and for these no good explanation is available other than lack of information describing the well or local geological conditions.

To illustrate the latter point, the towns of Lostant, Toluca, Wenona, and Minonk may be cited. These four towns are located in an area which has a north-south dimension of about 15 miles and an east-west dimension of about 6 miles in a region where a geological fault is known to exist.(7) The information available indicates that the wells in these towns penetrate the St. Peters sandstone, but the average Ra^{228}/Ra^{226} ratio is 0.81 for the group in contrast with an average of 0.11 for the first 15 towns listed in Table 10.

Some deep sandstone wells in Wisconsin and Missouri have also been analyzed for both Ra^{228} and Ra^{226}. Table 11 is a summary of the data obtained thus far.

Table 10

Town	St. Peters sandstone	Galesville sandstone	Mt. Simon sandstone	Limestone	Other	Ra^{228}(a) $\mu\mu c/l.$	Ra^{226}(b) $\mu\mu c/l.$	$\frac{Ra^{228}}{Ra^{226}}$
Toulon	x					1.3	36.0	0.04
Ipava	x					1.9	25.0	0.07
Farmington	x					0.6	7.5	0.08
De Pue #1	x					.7	9.2	0.08
Viola	x					0.6	8.1	0.08
Glasford	x			x		1.1	11.6	0.09
De Pue #2-T	x					1.0	9.7	0.10
De Pue #2	x					1.1	9.6	0.11
Alpha	x			x		0.7	6.4	0.11
Woodhull	x			x		0.5	4.2	0.12
Shannon	x					2.1	17.0	0.12
Odell	x					1.5	11.2	0.13
Biggsville	x			x		2.4	16.0	0.15
Bushnell	x					3.4	18.0	0.19
Elmwood	x					1.8	8.2	0.22
Sterling	x	x				0.9	3.9	0.23
Galesburg	x	x				2.0	8.1	0.25
Monmouth	x	x				2.0	6.6	0.30
Chenoa	x			x	(c)	2.2	7.3	0.30
Fulton		x	x			1.5	4.8	0.31
Silvis				x	(c)	1.5	4.6	0.33
Ladd	x				x	2.6	7.4	0.35
Standard	x					2.4	6.6	0.36
Byron	x	x	x			1.8	4.7	0.38
Freeport	x				x	1.4	3.5	0.40
Lake Bluff	x(?)	x	x	x		2.2	5.8	0.42
Lombard	x	x				3.6	8.6	0.42
Wilmington	x	x		x		5.3	10.2	0.52
Elmhurst	x	x				2.7	5.1	0.53
Ottawa		x				3.8	6.4	0.59
De Kalb #6	x	x				2.9	4.9	0.59
Kewanee	x	x				4.9	8.1	0.60
Rockford		x	x		x	2.2	3.5	0.63
De Kalb #7	x	x				2.0	3.1	0.64
Lostant	x					6.5	9.9	0.66
Savanna			x			2.0	3.0	0.67
Plainfield	x	x				5.4	8.0	0.68
Lockport	x	x				7.9	11.2	0.70
Toluca	x					5.3	7.3	0.73
Villa Park	x	x	x	x		3.3	4.2	0.78
Morris #4		x				6.6	8.0	0.82
Oregon		x	x			2.7	3.1	0.87
Geneva		x	x			5.8	6.4	0.91
Braidwood	x	x		x		5.8	6.4	0.91
Minonk #2	x			x		7.1	7.8	0.91
Wenona	x					9.1	9.3	0.98
Argonne deep well	x	x	x	x		5.2	5.0	1.04
Joliet		x				7.0	6.7	1.04
Aurora	x(?)	x	x			8.0	6.8	1.18
Kinsman	x			x	x	5.4	4.4	1.23
Batavia		x	x			8.0	5.6	1.43
Morris	x					5.6	2.3	2.43

(a)Estimated error in Ra^{228} values is ± 10%.
(b)Statistical counting error equal to or less than 3%. (c)New Richmond sandstone.

Table 11

$\frac{Ra^{228}}{Ra^{226}}$ ratios on some deep sandstone wells in Wisconsin and Missouri

Town	Ra^{228}(a) $\mu\mu c/l.$	Ra^{226}(b) $\mu\mu c/l.$	Ratio $\frac{Ra^{228}}{Ra^{226}}$
Wisconsin			
Hartford	1.5	6.2	0.24
Fond du Lac	2.7	6.6	0.41
Burlington	2.0	4.2	0.47
Peshtigo	2.1	3.6	0.58
Kaukauna	2.7	4.0	0.67
Oconto	2.4	3.6	0.67
Menomenee Falls	5.0	4.7	1.06
Waukesha	8.8	4.2	2.09
Missouri			
Clinton #2	1.8	10.4	0.17
Clinton #1	1.9	9.0	0.21
Concordia	4.4	10.5	0.42

(a)Estimated error ± 10%.
(b)Statistical counting error equal to or less than 3%.

References

1. Krause, D. P. Radiological Physics Division Semiannual Report, ANL-5967 (May 1959) pp. 126-128.

2. Lucas, H. F., and Ilcewicz, F. H. J. Am. Water Works Assoc. 50 1523-1532 (1958).

3. Krause, D. P. Radiological Physics Division Semiannual Report, ANL-6049 (October 1959) pp. 51-52.

4. Lucas, H. F. This report, page 82.

5. Lucas, H. F., and Krause, D. P. Radiology 74 114 (1960).

6. Hanson, Ross. Public Ground-Water Supplies in Illinois, Illinois State Water Survey Bulletin No. 40 (1950).

7. Bretz, J. Harlan. Geology of the Chicago Region, Illinois State Geological Survey (Part I), Bulletin No. 65.

Ra^{226} IN BOVINE BONES AND TEETH

Elvira R. Di Ferrante

Twenty-five bovine jaw bones with teeth were collected from different states, through the help of the U. S. Army Veterinary Service who furnished data on age, breed, diet, place and time of pasture. The samples were identified by numbers according to the time they were received, but for this study they are listed according to the point of origin. They are assigned to three groups corresponding to the western, central, and eastern regions of the United States.

Toothless portions of the jaw bone and second or third premolars were used for the analyses unless these teeth were not available. The bones, ashed at 620°C, and the teeth at 1000°C, were dissolved in HNO_3 and analyzed for Ra^{226} content by the radon emanation technique.(1,2)

At least two determinations were made on each sample, and they agreed consistently to within ±3.0 percent. Since the value of blank determinations was of the order of 0.01 $\mu\mu$g Ra^{226}, an insignificant amount compared with that in the total sample, no blank correction has been made in the calculations.

The results of the analyses are shown in Tables 12, 13, 14, with the calculated ratio of the concentrations in bone and teeth. The average value for the radium content in bone is the highest in the eastern region (1.197 $\mu\mu$g/g ash) and the lowest is in the western region (0.250 $\mu\mu$g/g ash). The samples of the central region with an average value of 0.377 $\mu\mu$g/g ash, show the greatest uniformity of radium content. The average value for the eastern region does not include a horse sample (14C), which has a very low radium content. Results of additional analyses performed in order to check the data obtained previously, are shown in parentheses in Tables 12, 13, and 14. The agreement between the results is significantly higher for the bone analyses, with a maximum discrepancy of 16%.

Although final conclusions await the result of further analyses, it appears that the greater discrepancies noted in some teeth can be linked with placental discrimination against radium transfer to the newborn (affecting the radium content of teeth partially formed at birth) and subsequent dietary changes concomitant with tooth eruption and calcification.(3,4)

For the moment it is worth noting that, in general, the results of this study show agreement between Ra^{226} content of ashed bones and teeth formed after weaning age. The graphical representation of results in Fig. 38, shows points scattered around a straight line representing a ratio equal to 1; the average value of the ratios of Ra^{226} in bones and teeth, as given in Tables 12, 13, and 14 is 1.03 ± 0.2. It is evident that the ratio,

Table 12

Ra^{226} content of bovine bones and teeth, western region

No.	Location and age	$\mu\mu g\ Ra^{226}/g$ ash*		Ra^{226} ratios Bone/Tooth
		Bone	Tooth	
3C	Spokane, Wash. 4y 7m	0.380	P3** 0.380 (P2 0.341)	1.00
4C	Inland Emp., Wash. 3y	0.270	P2 0.220	1.23
1C	Elk Grove, Cal. 17y	0.185	P2 0.221	0.84
2C	Elk Grove, Cal. 17y	0.191	P3 0.244	0.78
22C	Salt Lake City, Utah 10y	0.232	P2 0.261	0.89
10C	Anthony, N. Mex. 6y	0.245	P2 0.286	0.86
		Av. contained in bone: 0.250 $\mu\mu g/g$ ash		

*Average value of two or more analyses; range of estimated error = $\pm$0.006-0.02 $\mu\mu g/g$ ash; results of additional analyses in parentheses.

**Code: DP2 = second deciduous premolar
DP3 = third deciduous premolar
I3 = third permanent incisor
I4c = 4 mm slice cut at the extremity of the crown
I4r = tip of the root (6 mm)
M1 = first molar
P2 = second permanent premolar
P3 = third permanent premolar

Table 13

Ra^{226} content of bovine bones and teeth, central region

No.	Location and age	$\mu\mu g\ Ra^{226}/g$ ash*		Ra^{226} ratios Bone/Tooth
		Bone	Tooth	
13C	Cogswell, N. Dak. 7y	0.327	P3* 0.370	0.88
8C	White Bear, Minn. 5y	(0.288) (0.247)	P3 0.266	1.08
12C	Glyndon, Minn. 3y	0.331	DP3 0.253	1.30
25C	Zumbro Valley, Minn. 7y	0.333	P3 0.370	0.90
9C	Omaha, Neb. aged cow	0.414 (0.398)	P3 0.467	0.88
7C	Lyndon, Kans. 6y	0.389	P2 0.340	1.14
17C	Lyndon, Kans. 5y	0.431 (0.430)	P3 0.485 (P2 0.621)	0.88
18C	Lyndon, Kans. 5y	0.483 (0.508)	P2 0.293 (M1 0.226)	1.60
11C	Wellston, Okla. 6y	0.333	P3 0.329 (P2 0.299)	1.01
19C	Shawnee, Okla. 5y	0.396 (0.386)	P3 0.449 (P2 0.563)	0.88
6C	Amarillo, Tex. 3y	0.405	P2 0.426	0.95
5C	Chicago, Ill.	0.395	P3 0.364 (not erupted molar 0.235)	1.08
		Av. contained in bone: 0.377 $\mu\mu g/g$ ash		

*See footnotes, Table 12.

Table 14

Ra^{226} content of bovine bones and teeth, eastern region

No.	Location and age	$\mu\mu g\ Ra^{226}/g$ ash*		Ra^{226} ratios Bone/Tooth
		Bone	Tooth	
15C	Columbus, Ohio 2y	0.511	DP3* 0.448 (DP2 0.429)	1.14
24C	Wapakoneta, Ohio 2y 6m	0.526	DP2 0.415 (DP3 0.488)	1.26
16C	Augusta, Ga. 8y	0.973	I3 0.865	1.12
23C**	Augusta, Ga. 5y	2.58	I3 2.16 (M1 0.800) (I4c 2.35; I4r 3.53)	1.19
20C	Fayetteville, N. C. 2y	1.345	DP2 1.20	1.11
21C	Fayetteville, N. C. 1y	1.25	M1 1.68	0.74
14C***	Charleston, S. C. 9y	0.136	0.141	0.96
		Av. contained in bone: 1.197 $\mu\mu g/g$ ash		

*See footnote, Table 12.

**The unusually high content in this sample has been verified and confirmed by gamma-spectrum scintillation counting.

***Horse sample.

constantly close to 1, is not a function of the radium concentration if analysis is confined to the second or third premolar tooth, even though the absolute concentration in bone varies by a factor of twenty. The fact that such good agreement exists between the radium content in teeth and bones indicates the potential usefulness of Ra^{226} analyses of teeth for the estimation of body burden; it must be noted, however, that this usefulness is predicated upon knowledge of animal history and proper selection of the tooth specimen.

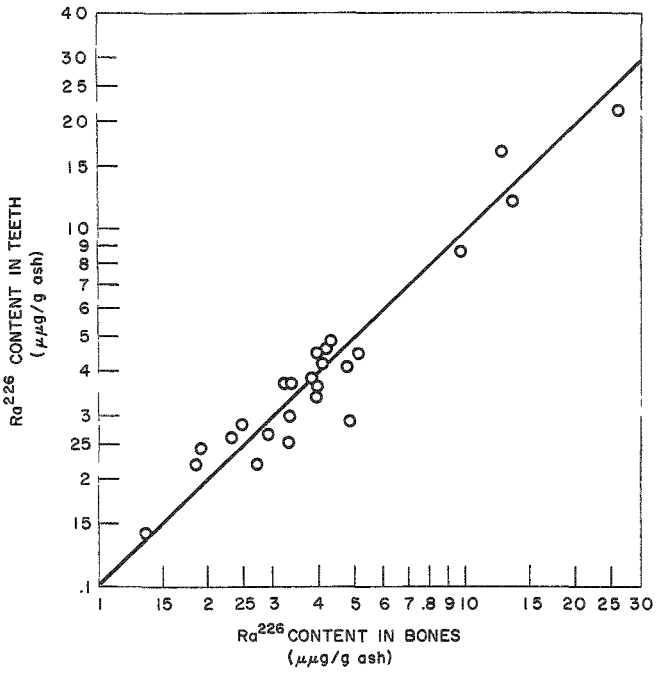

Fig. 38
Ra^{226} content of bovine bones and teeth

The results of analyses of other radioelements in such samples will be reported later.

I wish to express my gratitude to Dr. J. E. Rose and Mr. L. D. Marinelli for making possible my work and my study at ANL and my appreciation of the help from Mr. H. F. Lucas, Miss D. E. Wallace and other members of the Division.

References

1. Lucas, H. F., Jr., and Ilcewicz, F. H. Natural Ra^{226} Content of Illinois Water Supplies. J. Am. Water Works Assoc. 50 1523 (1958).

2. Lucas, H. F., Jr. Improved Low-Level Alpha Scintillation Counter for Radon. Rev. Sci. Instr. 28 680 (1957).

3. Marsden, E. Radioactivity of Soils, Plants Ashes and Animal Bones. Nature 183 924 (1959).

4. Comar, C. L., and Wasserman, R. H. Differential Behavior of Substances in Metabolic Pathways. Radioisotopes in the Biosphere, ed. R. S. Caldecott and L. A. Snyder. Minneapolis:University of Minn. Press, 1960. pp. 526-539.

SOME DETERMINATIONS OF THE RaD AND RaF CONCENTRATIONS IN HUMAN BONE

Richard B. Holtzman

I. Introduction

Full assessment of the natural radiation in the human environment necessitates the study of the internal natural radioactivity of the body concomitantly with that of external radiation. Considerable work has been done in this laboratory and elsewhere to determine the amount and variability of the concentration of Ra^{226} in the body and to correlate it with the environment, mainly drinking water.[1] This nuclide is a major source of radiation in the body, and methods have been developed to study it *in vivo*[2] as well as *in vitro*. Radium-228 and its daughter Th^{228} have been studied to some extent.[3,4] A few studies have been made of the uranium concentrations in the body,[5] but little has been found, although studies on rabbits and rats indicate that activities comparable to that of Ra^{226} may be deposited in the body.[6] Potassium-40 accounts for a large fraction of the internal absorbed dose, but its importance is reduced considerably if an estimated relative biological effectiveness for alpha particles of four is assumed.

The RaDEF series has been studied little, but Dudley[7] has estimated the radiation dose to be about equal to that of Ra^{226}. A more accurate estimate of this contribution is very important in the study of low level radiation effects on human populations.

In such a study it is necessary to compare certain aspects of population groups receiving a high radiation dose to those aspects in otherwise identical groups receiving a lesser radiation dose. Studies at this Laboratory have shown radiation levels, as represented by Ra^{226}, to vary by more than a factor of 10 from one geographical region to another.[8] However, the variation in total dose rate is considerably less when account is taken of radiation originating outside the body[7] and might be further reduced to less than a factor of 2 if some radioactive series, such as RaDEF, were uniformly distributed in the population at a concentration such as to produce an effective dose level equal to that of the higher Ra^{226} concentrations in humans. This would make an epidemiological study particularly difficult, since the amount of data needed is an inverse function of the range of radiation levels.

The location of RaD in the biosphere might be expected to differ from that of the shorter lived daughters of Ra^{226} because of its long half-life and chemistry. Moreover, its precursor, Rn^{222}, is a noble gas of radioactive life long enough to permit appreciable translocation with respect to the parent Ra^{226}.

II. Technical Discussion

RaD (Pb^{210}) decays with a 20-year half-life and by a low energy beta-emission to RaE (Bi^{210}) which in turn decays with 5.0-day half-life and 1.17-Mev beta particle to RaF (Po^{210}). The latter decays with a 138.4-day half-life emitting a 5.3-Mev alpha particle.

Surgical bone and tooth specimens were obtained from medical sources, mainly through the efforts of Dr. A. J. Finkel and Mr. H. F. Lucas. The subjects were mostly from Illinois, although many had resided in other areas. Localities with both high and low Ra^{226} content in the drinking water are represented. The Ra^{226} content was determined by the radon emanation method.

The specimens were analyzed for RaD and RaF according to the procedures in Appendix I, usually within 6 months of surgery, and as a result, the radioactive decay equilibrium between RaD and RaF is to be taken into account.

The RaD content of a sample is determined by removal of RaF and subsequent measurement of the RaF grown back within a known time interval. The original RaF at the time of removal of the specimen from the subject at time t = 0 is determined from the RaD content, the known amount of RaF removed in the first analysis, and the time between this first analysis and the time t = 0.

If the RaF in the specimen is initially at greater than 50% of radioactive equilibrium with RaD and the specimen is over 3 months old, the error in the RaD determination is not large. However, as the sample ages and radioactive equilibrium is approached, the error in the determination of the RaF originally present increases. This error is essentially that of the dose, and, therefore, it is important in dose determinations. In order to obtain maximum accuracy in the determination of RaD, the time between the RaF analyses must be long, at least one half-life, whereas to secure maximum accuracy in the determination of the initial RaF present, the first analysis must be done as soon after removal of the specimen as possible (t_1 small).

The degree of radioactive equilibrium between RaD and RaF was determined by analyzing a few of the specimens soon after surgery, and again analyzing the same samples several months later. The RaD was determined from the equation

$$A_0(\text{RaD}) = \left[-A_2(\text{RaF})\, e^{-\lambda t_2} + A_3(\text{RaF})\right]\left(1-e^{-\lambda t_2}\right)^{-1} \qquad (1)$$

where $A_0(RaD)$ = RaD activity of the sample.

$A_3(RaF)$ = RaF activity measured in the second analysis.

t_2 = time between 1st and 2nd analyses.

$A_2(RaF)$ = activity of RaF remaining in sample after the first analysis.

λ = decay constant of RaF

The RaF originally in the sample may then be determined from the equation

$$A_0(RaF) = \frac{A_1(RaF) - A_0(RaD)\left(1-e^{-\lambda t_1}\right)}{e^{-\lambda t_1}} \qquad (2)$$

where in addition to the above definitions:

$A_0(RaF)$ = RaF concentration at the time the specimen is removed from the subject.

$A_1(RaF)$ = RaF concentration at the time of the first analysis.

t_1 = time between removal of the specimen from the subject and the time of the first analysis.

$A_2(RaF)$ is assumed to be 8% of $A_1(RaF)$, based on a yield of 92% as discussed in Appendix I.

The results shown in Table 15 indicate that the ratio of RaF to RaD cannot be predicted in general. The errors indicated are the 0.9 confidence limit based on counting statistics. However, the values obtained overlap within statistical errors so that, as a first approximation, it will be assumed that the ratio RaF/RaD = 1.0 ± 0.2 in the rest of the specimens (Table 16).

Table 15

Radioactive equilibrium between RaD and RaF in bone specimens

Sample No.	Type of tissue	Ratio RaF/RaD
	Human bone specimens	
115B	Iliac crest	0.81
131B	Rib	0.77
135B	Vertebra	0.79
140B	Joint	1.00
186B	Rib	1.43
245B	Rib	1.17
Average		1.0 ∓ 0.2

Table 16

Ra^{226} and RaD concentrations in human bone

Sample identification	Age (tissue removed)	Sex	Type of bone	Ra^{226}, $\mu\mu g/g$ ash	RaD, $\mu\mu c/g$ ash
41B5	68	M	Teeth	0.019 ± 0.003	0.018 ± 0.004
279B	3	M	Femur	0.021 ± 0.005	0.037 ± 0.015
42B4	43	F	Jaw	0.028 ± 0.002	0.049 ± 0.004
284B	75	M	Femur	0.033 ± 0.004	0.054 ± 0.006
277B	66	M	Femur	0.023 ± 0.003	0.058 ± 0.009
76T	30	F	Teeth	0.062 ± 0.007	0.063 ± 0.006
221B	56	F	Rib	0.017 ± 0.003	0.063 ± 0.010
43B3	52	F	Joint	0.027 ± 0.003	0.071 ± 0.007
146B	25	M	Tibia	0.042 ± 0.003	0.074 ± 0.006
280B	9	M	Femur	0.012 ± 0.003	0.075 ± 0.009
43B4	52	F	Jaw	0.030 ± 0.003	0.077 ± 0.006
43B1	52	F	Tibia	0.026 ± 0.002	0.078 ± 0.006
185B	48	M	Rib	0.024 ± 0.005	0.078 ± 0.008
42B3	43	F	Joint	0.025 ± 0.002	0.083 ± 0.008
243B	45	M	Rib	0.023 ± 0.005	0.084 ± 0.006
42B1-2	43	F	Tibia	0.025 ± 0.002	0.090 ± 0.009
41B4	68	M	Jaw	0.012 ± 0.003	0.093 ± 0.005
207B	36	M	Vertebra	0.018 ± 0.003	0.094 ± 0.006
186B	55	M	Rib	0.059 ± 0.011	0.098 ± 0.010
231B	63	M	Vertebra	0.022 ± 0.004	0.106 ± 0.006
120B	-	M	Femur	0.100 ± 0.008	0.11 ± 0.01
238B	-	-	Vertebra	0.023 ± 0.007	0.113 ± 0.009
276B	48	M	Talus	0.030 ± 0.004	0.120 ± 0.012
78T	52	M	Teeth	0.075 ± 0.006	0.120 ± 0.011
42B2-2	43	F	Skull	0.051 ± 0.002	0.131 ± 0.009
281B	65	M	Talus	0.067 ± 0.006	0.138 ± 0.011
245B	61	M	Rib	0.028 ± 0.007	0.150 ± 0.007
131B	50	M	Rib	0.010 ± 0.002	0.150 ± 0.010
232B	50	M	Rib	0.014 ± 0.004	0.150 ± 0.007
41B3	68	M	Joint	0.016 ± 0.001	0.152 ± 0.007
239B	-	-	Vertebra	0.015 ± 0.003	0.160 ± 0.014
135B	55	M	Vertebra	0.019 ± 0.003	0.17 ± 0.01
232B	50	M	Sternum	0.014 ± 0.004	0.174 ± 0.015
278B	59	M	Tibia	0.050 ± 0.002	0.182 ± 0.010
269B	-	M	Rib	0.027 ± 0.005	0.191 ± 0.012
41B2-1	68	M	Skull	0.070 ± 0.004	0.201 ± 0.015
191B	69	M	Rib	0.191 ± 0.016	0.211 ± 0.015
140B	75	M	Rib	0.029 ± 0.005	0.239 ± 0.050
41B1-2	68	M	Tibia	0.012 ± 0.003	0.269 ± 0.013
208B	36	F	Rib	0.064 ± 0.007	0.280 ± 0.011
115B	62	M	Iliac crest	0.067 ± 0.003	0.29 ± 0.02
140B	75	M	Joint	0.036 ± 0.006	0.337 ± 0.030
43B2-2	52	F	Skull	0.032 ± 0.003	0.366 ± 0.019
41B2-2	68	M	Skull	0.070 ± 0.004	0.419 ± 0.015
43B2-1	52	F	Skull	0.027 ± 0.003	1.33 ± 0.03

It is possible that the yield varies greatly from the assumed 92% (see Appendix I) in some cases, although a large amount of data indicates the improbability of such occurrences.

III. Results and Discussion

The results of the analyses of the RaD and Ra^{226} content of the bulk of the specimens are shown in Table 16. An effort has been made to determine whether any correlation exists between the RaD and Ra^{226} concentrations in various types of bone; thus, a plot of RaD and Ra^{226} values in ribs shown in Figure 39 indicates that they fall into two groups which roughly follow the curves

$$y = 3x + 0.11 \quad (3)$$

or

$$y = 0.8x + 0.05 \quad (4)$$

where y = RaD concentration in $\mu\mu c/g$ ash

x = Ra^{226} concentration in $\mu\mu g/g$ ash.

Figure 40, a plot of RaD vs Ra^{226} concentration in teeth and cortical bone, indicates that most of these fall into the lower group. A large scatter of data in the skull bones is observed. In some cases there is a variation of a factor of 2 in both Ra^{226} and RaD concentrations between two specimens of the same subject.

Figure 41 shows the RaD vs Ra^{226} concentrations of miscellaneous bones. These again appear to fall into two groups with a very large scatter.

Figure 42, the plot of the number of samples in a given RaD range vs the RaD concentration, indicates again that there are 3 groups of concentrations, one around 0.080 $\mu\mu c/g$ ash, one sharp peak at 0.150 $\mu\mu c/g$ ash, and a third group, those values above about 0.2 $\mu\mu c/g$ ash. This suggests that several types of sources of intake of RaD may be available and that people might tend to use only one or the other. Vegetarians, for instance, may ingest more RaD than individuals who consume meat as a large part of the diet.

Table 17 is a listing of the RaD concentrations in specimens of bone (rib, except for an iliac crest and a section of tibia as noted) of subjects who were life-long residents of Chicago and vicinity. It is suggested that the large range of values may be due to individual biological variations, such as amount of activity consumed and absorption through the gut. In the latter case evidence of this is seen in studies of the metabolism of lead.(9)

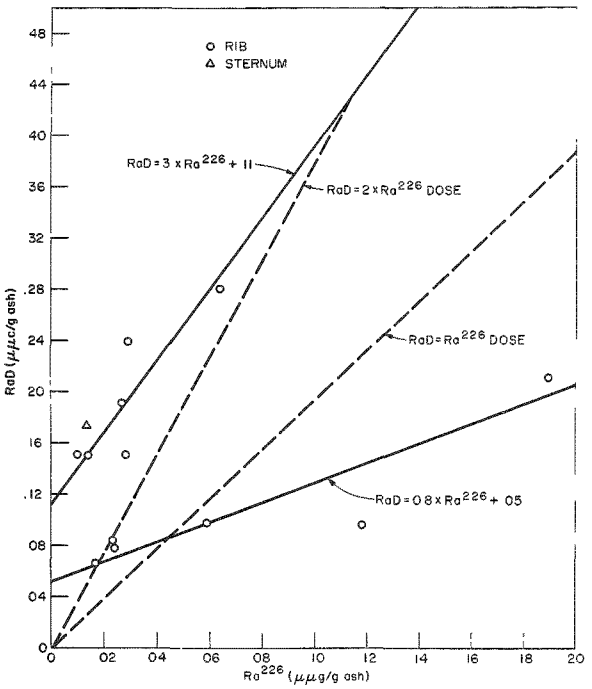

Fig. 39. RaD vs Ra^{226} concentrations in rib specimens.

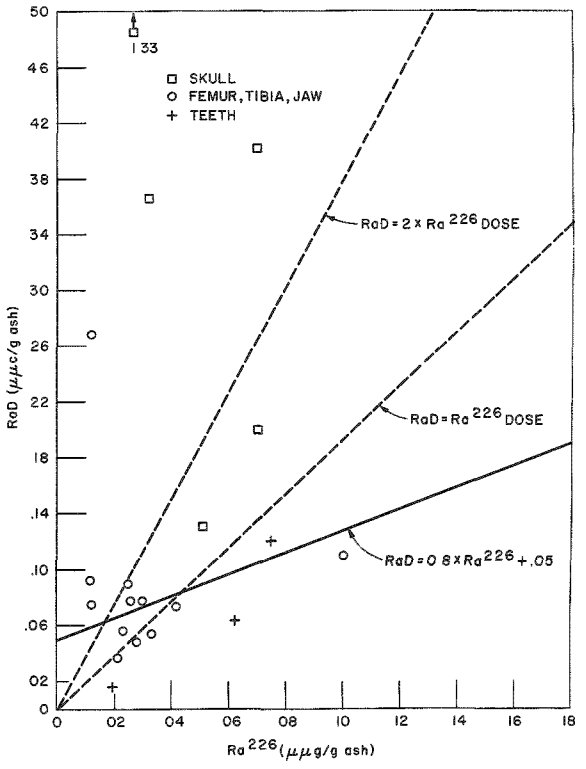

Fig. 40. RaD vs Ra^{226} concentrations in cortical bones and teeth.

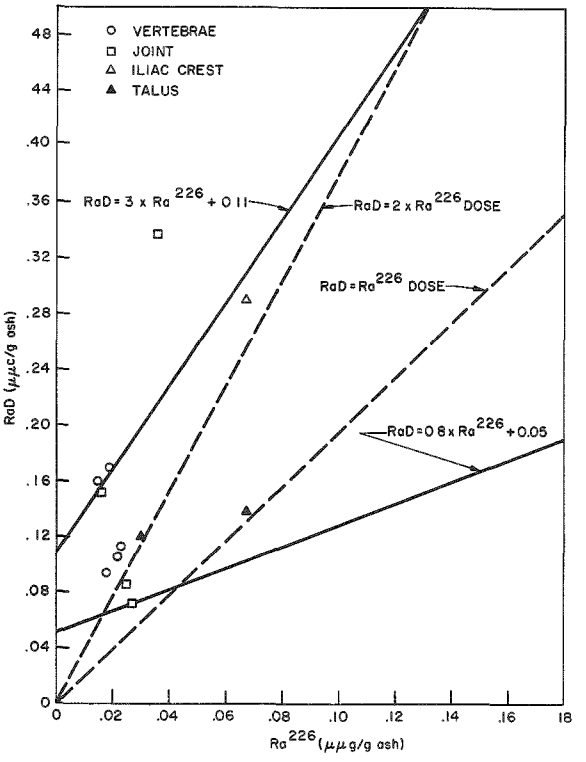

Fig. 41. RaD vs Ra^{226} concentrations in trabecular bones.

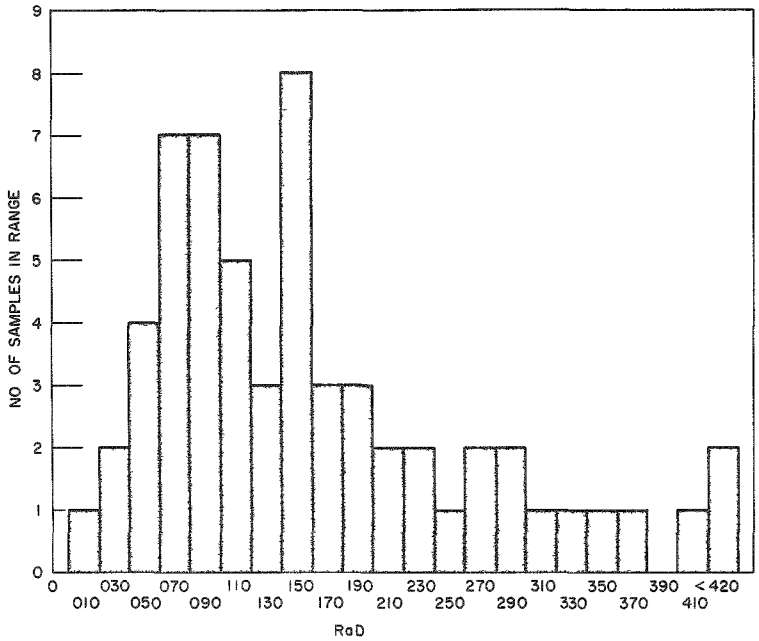

Fig. 42. Frequency of occurrence of a given concentration of RaD in the bone samples as a function of RaD concentration in $\mu\mu c/g$ ash.

Table 17

RaD content of bone from residents of Chicago and vicinity

Sample identification	Age	Sex	RaD	Specimen
146B	25	M	0.074 ± 0.006	Tibia
243B	45	M	0.084 ± 0.006	Rib
233B	47	M	0.096 ± 0.007	Rib
222B	72	M	0.134 ± 0.013	Rib
210B	46	M	0.190 ± 0.015	Rib
115B	62	M	0.29 ± 0.02	Iliac crest
219B	54	M	0.435 ± 0.047	Rib

Figure 43 is a plot of the RaD concentration in the trabecular bone samples as a function of age at the time of surgery. There is a tremendous scatter of the data, but there is some indication that the RaD concentration in the trabecular bones increases with age. However, taking the cortical bones and teeth, except for skull, as a group (Fig. 44), the RaD concentration appears to remain fairly constant throughout life.

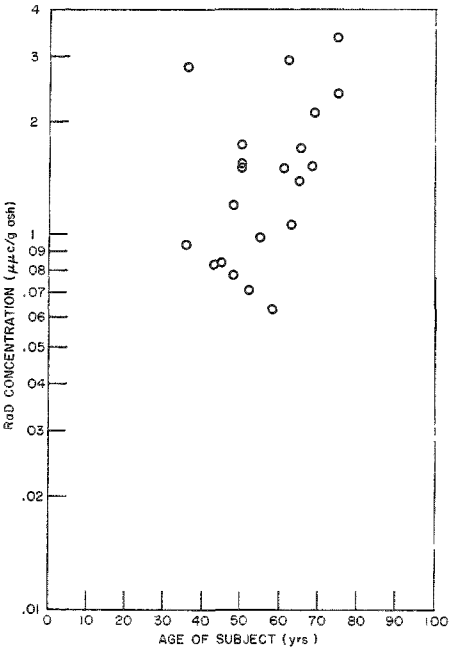

Fig. 43. RaD concentration in trabecular bone as a function of age of the person at the time of surgery.

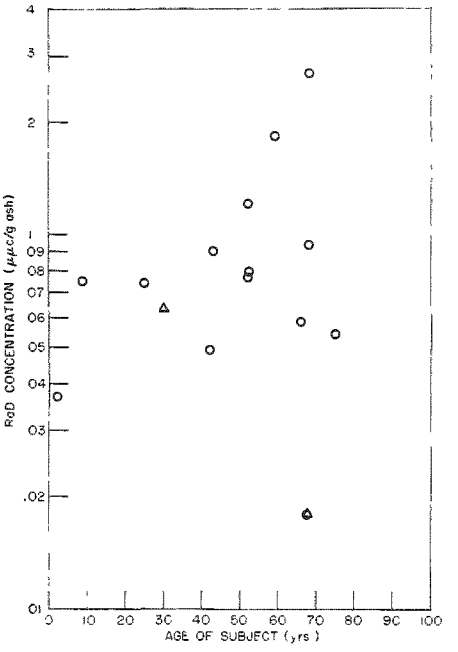

Fig. 44. RaD concentration in cortical bones and teeth as a function of the age of the person at the time of surgery. Δ , teeth; 0, cortical bones.

These results indicate that, in the more trabecular bones (rapidly metabolizing), the RaD accretion rate is higher than that of combined excretion and radioactive decay rates. This results in an increase of RaD concentration with time. On the other hand, these rates are about equal in the teeth and cortical type bones resulting in a fairly constant RaD level throughout life.

While RaD in the body should be metabolized like lead, these results appear to disagree with those of one of the latest studies[10] in which no variations of lead concentration with age were found in the bones of subjects with no known lead exposure. These results also differ from those of Ra^{226} in which little or no variation with age is observed.[1]

IV. Conclusions

The results obtained here are in substantial agreement with those of Black,[11] but are somewhat higher, on the average, than those obtained by Hursh[12] on whole skeletons which had been ashed about 7 years previous to measurement. These differences could be due to regional and individual biological variations.

The data show that the internal dose due to RaD and its decay product RaF is wholly comparable to, if not higher than, that due to Ra^{226}. In fact, neglecting the extreme high value of RaD in 42B2-1, the average concentrations in the specimens of Table 16 are 0.037 $\mu\mu$g Ra^{226}/g ash and 0.14 $\mu\mu$c RaD/g ash. Assuming an RBE of 4 for alpha particles, the dose equivalence of the RaD is 1.0 $\mu\mu$c(RaD + RaE + RaF) = 0.53 $\mu\mu$g [Ra^{226} + 0.3(Rn^{222} + RaA + RaB + RaC + RaC')]. These findings suggest that, if RaF is in equilibrium with RaD, the Ra(D + E + F) dose is twice that due to Ra^{226} and its daughters.

The RaD concentration appears to be more or less independent of the Ra^{226} values, particularly in the case of low Ra^{226} concentration. In areas in which the population has a higher Ra^{226} content, there is some indication that the RaD concentrations roughly equal those of Ra^{226}.

The origin of RaD in the body is not well known, but possible sources are Ra^{226} in the skeleton, Rn^{222} dissolved in the body fluids, and RaD in potable waters, the atmosphere, and food. The contribution of each of these sources has been estimated for equilibrium conditions, i.e., in which the uptake equals the excretion rate and under the assumption that the subject has lived under constant conditions for about 35 years.

Ra^{226} in the body decays through its daughters to RaD, which at equilibrium equals the Ra^{226} concentration multiplied by the radon retention factor. The actual RaD activity retained must be corrected also for an effective biological half-life, T_e, in bone by the ratio T_e/T_r, where T_r is the radioactive half-life. If the Ra^{226} concentration is 0.037 $\mu\mu$g/g ash (an average value derived from the subjects in Table 16), the radon retention is 0.3, T_e is 2400 days[13] and T_r is 7300 days, a value of 0.004 $\mu\mu$c/g ash of RaD is derived from the Ra^{226} body content.

The RaD activity due to Rn^{222} in the body can be estimated from the Rn^{222} dissolved in the body fluids contingent to the following physiologic and metabolic assumptions:

a) the body contains Rn^{222} equivalent to that in 50 liters of air (at 3 $\mu\mu$c Rn^{222}/l.);

b) 28% of the RaD formed[14] enters a skeleton containing 2800 g of ash and,

c) T_e and T_r are as mentioned above.

With these assumptions, the RaD to be expected from this source is only 0.005 $\mu\mu$c/g ash, even though the value assumed for the Rn^{222} concentration in the air is 10 times that usually found.[15]

The RaD in the skeleton derived from potable waters may be estimated from the formula for the effective half-life of RaD in the body:[13]

$$T_e = \frac{0.693\ m\ C}{I\ f} \qquad (5)$$

where $T_e = 2.4 \times 10^3$ days for RaD,

m = mass of skeletal ash (2800g).
C = $\mu\mu$c/g ash of RaD
f = fraction of the RaD fixed in the skeleton
I = $\mu\mu$ c of RaD ingested per day.

If the highest measured RaD concentration in water is used, i.e., 0.4 $\mu\mu$c/l., and it is assumed that 1.5 l. of water is ingested per day, then I = 0.6 $\mu\mu$c/day. Since f = 0.02,[13] RaD in water may provide a maximum of C = 0.015 $\mu\mu$c/g ash to the RaD body concentration.

The RaD in the air may also contribute to the deposition of RaD in the body. If a concentration of 0.03 $\mu\mu$c/m^3[16] and an average breathing rate for man of 20 m^3 per day are assumed,[13] then I = 0.6 $\mu\mu$c/day. Moreover, about 25% of the RaD in the air is removed by the lungs[17] and of this about 28% is taken up by the skeleton, so that f = 0.07. Use of these factors in equation (5) leads to a contribution from this source of 0.052 $\mu\mu$c/g ash.

Finally, the RaD intake from food remains to be evaluated: the intake may be assumed to be of the order of 1.8 $\mu\mu$c/day on the basis of a fecal analysis from a Chicago boy and 2 analyses of urine from Stateville subjects * If the same values of f, m, T_r and T_e used above are retained, the food contribution to the RaD concentration in the skeleton is 0.045 $\mu\mu$c/g ash.

These calculations, summarized in Table 18, show that Ra^{226} and Rn^{222} in the body are definitely not the major sources of RaD in the body and that the contribution of RaD in potable waters is also likely to be minor. The atmosphere and food appear to be the major supply of the RaD in the skeleton, although the sum of our estimates is somewhat low compared to the average measured value. Because the assumptions in the calculations for absorption of RaD from air[17] appear to be substantiated better than those for absorption from food, it appears the air values are more nearly correct. The source of the large variations in the RaD content of various subjects will, therefore, most likely be found in the food.

Further work is planned to determine the nature and cause of the variations observed here.

*In the latter two cases, it was assumed that the RaD content of the urine was 10% of the total RaD excretion (and uptake).

Table 18

The contributions of various sources to the RaD content of the human skeleton (for assumptions see text)

Source	Contribution to RaD concentration ($\mu\mu$c/g ash)
Measured RaD concentration	0.14
Ra^{226} in bones	0.004
Rn^{222} dissolved in body (equivalent to 50 ℓ. of air)	0.005
Potable water (Maximum observed RaD concentration 0.4 $\mu\mu$c/ℓ.)	0.015
RaD in atmosphere	0.052
Food	0.045

Special thanks are due to Mr. H. F. Lucas and Dr. A. J. Finkel for obtaining the specimens and information about them. Thanks are also due Mr. Ronald Burke for many of the Ra^{226} measurements.

References

1. Muth, H., Rajewsky, B., Hantke, H. J., and Aurand, K. The Normal Radium Content and the Ra^{226}/Ca Ratio of Various Foods, Drinking Water, and Different Organs and Tissue of the Human Body. Health Physics 2 239 (1960). Contains many references to the literature in this field as does: Stehney, A. F. Radioisotopes in the Skeleton: Naturally Occurring Radioisotopes in Man ed. Caldecott, R. S. and Snyder, L. A. Minneapolis: Radioisotopes in the Biosphere, Univ. Minn. Press, 1960. pp. 366-381.

2. Stehney, A. F., Norris, W. P., Lucas, H. F., Jr., and Johnston, W. H. A Method for Measuring the Rate of Elimination of Radon in Breath. Am. J. Roentgenol. 73 774 (1955)

3. Lucas, H. F. and Krause, D P. Preliminary Survey of Radium-226 and Radium-228 (MsThI) Contents of Drinking Water. Radiology 74 114 (1960).

4. Wallace, D. E., Stehney, A. F. and Ilcewicz, F. H. Th^{228}, Ra^{228}, and Ra^{226} in Bone. Radiological Physics Division Semiannual Report ANL-5967 (May 1959). pp. 107-110.

5. Hofmann, J. Uranium Concentration of Related Organs: Hypophysis, Thyroid, Generative Glands, Adrenal Gland, and Pancreas. U.S. Atomic Energy Commission Translation, AEC-tr-2817.

6. Ferretti, R. J. and Schwartz, S. Uranium Distribution Studies. pp. 274. Toxicology of Uranium, ed. A. Tannenbaum. New York: McGraw-Hill Book Co., Inc., 1951. pp. 274-282.

7. Dudley, R. A. Natural and Artificial Radiation Background of Man. Low Level Irradiation, Washington, D. C.: American Association for the Advancement of Science, 1959.

8. Stehney, A. F. and Lucas, H. F. Studies on the Radium Content of Humans Arising from Natural Radium in their Environment, Proceedings of the International Conference on the Peaceful Uses of Atomic Energy, Geneva, 1955. New York: United Nations, 1956. Vol. 11 pp. 49-51.

9. Kehoe, R. A., Cholak, J., Hubbard, D. M., Bambach, K. and McNary, R. Experimental Studies on Lead Absorption and Excretion and their Relation to the Diagnosis and Treatment of Lead Poisoning, J. Ind. Hyg. Toxicol. 25 71 (1943).

10. Kehoe, R. A. Exposure to Lead. Occupational Med. 3 156 (1947).

11. Black, S. C., Low Level Polonium Determination of Tissue and Urine. University of Rochester Report UR-463 (1956).

12. Hursh, J. B. Private Communication to A. F. Stehney.

13. ICRP Committee II on Permissable Dose for Internal Radiation (1959) with Bibliography for Biological, Mathematical and Physical Data. Health Physics 3 1-380 (1960).

14. Hamilton, J. G. The Metabolic Properties of Various Materials. Univ. of Calif. Radiation Lab. Report, Medical and Health Physics Quarterly Report; January, February, and March, 1951, UCRL-1282. p. 32.

15. Moses, H., Stehney, A. F. and Lucas, H. F. The Effect of Meteorological Variables Upon the Vertical and Temporal Distributions of Atmospheric Radon. J. Geophys. Research 65 1223 (1960).

16. Lockhardt, S. B., Baus, R. A., Patterson, R. L. and Blifford, I. H. Some Measurements of the Radioactivity of the Air During 1957. Naval Research Laboratory Report NRL-5208.

17. Bale, W. F. and Shapiro, J. V. Radiation Dosage to Lungs from Radon and its Daughter Products. Proceedings of International Conference on Peaceful Uses of Atomic Energy, Geneva, 1955. New York: United Nations, 1956. Vol 13, p. 233.

Appendix I

ANALYSIS OF TISSUE SAMPLES FOR POLONIUM-210 (RaF)

Richard B. Holtzman

Polonium-210 (RaF) in tissues was determined by dissolving the samples in nitric and perchloric acids, destroying the nitrates and then plating the Po^{210} onto silver disks for counting. The dissolution of the tissue in oxidizing acids, or wet ashing, is necessary to prevent loss of the volatile polonium which occurs when dry ashed at 600°C.

The procedures used were those developed by Minto et al., and Black[1-3] with minor modifications. The sample is placed in a 500-ml erlenmeyer flask, 25 ml of 15.8M HNO_3 is added, and the flask is covered by a watch glass. The flask is allowed to stand overnight and then warmed slightly until most of the material is dissolved. The flask, covered by a watch glass, is then heated to just below the boiling point for several hours, adding more acid as necessary. The solution is cooled, and 72% perchloric acid is added, 20 ml for samples containing less than 10g of ash and 30 ml for larger samples. Perchloric acid is used instead of sulfuric acid since the presence of sulfate would precipitate the calcium in samples larger than 1g of ash per 200 ml of volume. The sample is heated to fuming; if it turns brown, it is cooled and 5 ml of HNO_3 is added, and the sample is again fumed. This procedure is repeated until a clear or straw-colored solution is obtained. The solution is cooled, 10 ml of 12M HCl is added, and the solution is fumed carefully to minimize the escape of $HClO_4$ vapors. After a total of 4 additions of HCl with subsequent fuming to destroy any nitrate present, the flask is cooled and the volume brought to about 150 ml. The pH of the solution is adjusted to about 0.3 by means of 4 M NaOH and 12 M HCl. Any insoluble residue may be dissolved by the addition of a few drops of 48% HF and slight heating. Little effect from this small amount of HF is detected on the glassware. The solution is cooled, diluted to 200 ml in a volumetric flask and a 5-to 10-ml aliquot removed for calcium analysis. The reagent blank is also determined.

The pH is again adjusted to 0.3 and the solution is placed in a plating cell described by Black.[3]

The cell consists of a Pyrex baby bottle from which the bottom has been removed. A Neoprene rubber gasket in the screw-cap forces a $1\frac{1}{2}$-inch diameter 5-mil silver disk against the mouth of the bottle to form a water-tight seal. The bottle with the disk serving as a bottom is then placed in a 90 to 100°C water bath. The solution is covered to prevent evaporation and stirred for about 7 hours. To prevent interference with the plating procedure from Fe^{+3}, about 30 mg of ascorbic acid is dissolved

in the solution. After plating, the solution is removed and the disk dried at a temperature below 100°C. The disk is then counted in a low background (0.02 to 0.04 c/m) Nuclear Measurements Corporation, PC-1 proportional alpha counter. The over-all efficiency of the counter is 0.51, including geometry, backscatter, and self-absorption corrections. Samples containing about 0.04$\mu\mu$c of Po^{210} may be readily analyzed with an accuracy of 25% with counting times of 16 to 24 hours.

A total yield of 91.9 ± 0.6% was found in samples of cow bones spiked with a 55.6 c/m standardized RaDEF solution. These data, shown in Table 19, demonstrate the quite consistent yield from 0.65 to 22 grams of ash from bone samples ranging from 1 to 34 grams.

Table 19

Yield of Po^{210} in plating procedure
(Cow bone)

Weight of bone, g	Counts per min. observed	Counts per min. in bone	Counts per min. due to spike	Yield, %
1.045	52.2 ± 0.5	0.3	41.9	93.3
5.308	51.8 ± 0.9	1.8	50.0	89.9
0.712	55.2 ± 0.7	3.7	51.5	92.5
20.956	58.9 ± 0.4	7.6	51.3	92.2
33.985*	66.0 ± 0.5	15.3	50.7	91.2
			Average	91.9 ± 0.6

No RaDEF Added

Weight of bone	Po^{210}, $\mu\mu$c/g
5.967	0.306
11.646	0.292
19.5016	0.331
Average	0.310 ± 0.015

*Specimen of different origin than other bones so that different correction is necessary for Po^{210} content of bone.

Equivalence of the Ash and Calcium Contents of Calcified Tissues

The concentration of natural radioelements is most frequently reported per unit ash weight. However, since a wet ashing procedure is required for Po^{210} analysis, the ash cannot be determined directly. This difficulty can be circumvented by determining the $Ca_3(PO_4)_2$ content in the solution (vide infra), assuming it is shown to be equivalent to the ash content of normal bones. The soundness of this approach seems to be justified by the following considerations.

Shohl[4] gives the mineral composition of the total skeleton in terms of the elements, except oxygen. Table 20 shows this composition with the addition of oxygen to give the expected compounds and proper charge balance. Table 21 shows the relation between ash, calcium, and $Ca_3(PO_4)_2$ content of various types of calcified tissues as given by Mitchell et al.[5] and Hawk.[6,7] To these data are added results obtained here from some cow bones and 25 samples of human calcified tissues. In the latter analyses, a piece of the specimen was dry ashed and weighed while another piece was wet ashed and the calcium content determined. The average value for the ratio $Ca_3(PO_4)_2$/ash of the various bones and teeth is 1.001 ± 0.012. Thus, Tables 20 and 21 show that, due to various compensating factors, the $Ca_3(PO_4)_2$ content is equal to the ash content in calcified tissue with errors of less than 3%.

Table 20

Mineral composition of skeleton*

Cation or Anion	Weight in skeleton, g
Na^+	18.7
K^+	6.4
Ca^{++}	1150
Mg^{++}	11.0
Cl^-	20.0
$PO_4^{\equiv}$	1640
$SO_4^{\equiv}$	48
$O^=$	45
Total mineral content (ash)	2939
$Ca_3(PO_4)_2$ equivalent	2974
Ratio $\frac{Ca_3(PO_4)_2}{ash}$	1.011

*Derived from data in Shohl.[4] Oxygen was added to obtain the form of the ions in ash and the amounts were adjusted for ionic balance.

Table 21

Ratio of calcium content as $Ca_3(PO_4)_2$ to ash content of mineralized tissues

	Ash, %	Calcium, %	$Ca_3(PO_4)_2$, %	$\frac{Ca_3(PO_4)_2}{ash}$	Reference
Human skeleton	28.91	11.02	29.3	1.012	(5)
Dog femur	61.5	23.3	61.9	1.005	
	61.7	23.2	61.5	0.997	(6)
Human teeth: Enamel	97.0	35.8	94.8	0.977	
Dentine	72.0	265.0	70.4	0.978	(7)
Cow Bone	69.2		68.8	0.995	this report
	67.8		68.0	1.001	
Average of 25 samples of calcified human tissues (rib, sternum, iliac crest, vertebra, joint, tallus, femur, tibia, teeth)				1.003 ± 0.015	this report
Over-all average				1.001 ± 0.012	

Calcium Determination

Calcium was determined either by the precipitation of calcium oxalate in hot oxalic acid solution at pH 4 or by the volumetric (ethylenedinitrilo)-tetraacetic acid (EDTA) titration of the calcium, i.e., the procedure of Yalman et al.[8] In this latter method, an aliquot containing about 20 mg of calcium is titrated with an excess of EDTA standardized against calcium. The pH is then raised to 12 with 4 M NaOH, and a calcium indicator, Calcon,* is added. The solution is then back-titrated to the indicator end point with a standardized calcium solution. The calcium content of the sample aliquot is then the difference in calcium equivalence between the EDTA and calcium titrating solutions.

*Fisher Scientific Co., Chicago, Illinois.

References

1. Minto, W. L. Digestion of Tissues and Excreta. Biological Studies with Polonium, Radium, and Plutonium, Robert M. Fink, Ed. New York: McGraw-Hill Book Company, Inc., 1950 pp. 15-18.

2. Vittum, E. K., Minto, W. L. and Fink, R. M. Plating Procedure. Op. cit., pp. 18-27.

3. Black, S. C., Low Level Polonium Determination of Tissue and Urine. University of Rochester Report, UR-463 (1956).

4. Shohl, A. T. Mineral Metabolism. New York: Reinhold Publishing Corporation, 1939, p. 19.

5. Mitchell, H. H., Hamilton, T. S., Steggerda, F. R., and Bean, H. W. The Chemical Composition of the Adult Human Body and its Bearing on the Biochemistry of Growth. J. Biol. Chemistry 158 625 (1945).

6. Hawk, P. B., Oser, B. L. and Summerson, W. H. Practical Physiological Chemistry, 13th Ed. New York: The Blakiston Company, Inc., 1954. p. 25.

7. Ibid, p. 256.

8. Yalman, R. G., Bruegemann, W., Baker, P. T., and Garn, S. Anal. Chem. 31 1230 (1959).

Appendix II

THE DISTRIBUTION OF THE RaD CONCENTRATION AS A FUNCTION OF BONE TYPE IN THREE UNEXPOSED SUBJECTS

Richard B Holtzman

In the study of the naturally occurring RaD body burden it is essential to know the variation in concentration with the type of bone in order that body content may be determined with fair accuracy from measurements on single bones, such as ribs or vertebrae, which are the most readily available.

Specimens from three humans were obtained from Dr. J. B. Hursh of the University of Rochester. Tibia, skull, joint bone, and mandible from each were supplied, and teeth from subject 41B were also available. The available information on these individuals is given in Table 22.

Table 22

Age, sex, and residence history of subjects

Identification	Age	Sex	Residence history
41B	68	M	Nebraska, birth- ?; Rochester, N.Y. to age 68?
42B	43	F	Conn., birth- ?; returned from England at 14; Rochester, N.Y. at ages 14-43.
43B	52	F	Florida, birth to age 49; Rochester, N.Y. to ages 49-52.

The samples had been prepared by ashing at 600° for 16 hours, dissolving in nitric acid and storing in polyethylene bottles about a year previous to these measurements. They were, therefore, close to equilibrium even though much of the RaF (about 30 percent) had been lost in ashing. The samples were evaporated to about 200 ml volume, and the nitric acid in the solutions was destroyed by adding 1 ml of formic acid at a time to the hot solution. About 25 ml 12 M HCl was also added to keep the pH of the solution low enough for the formic acid-nitric acid reaction to proceed. After the pH was adjusted to 0.3 with HCl in a volume of 200 ml, the RaF was determined. Since this isotope is essentially in equilibrium with the RaD, it represents the RaD concentration. The results are shown in Table 23.

Table 23

Concentration of Ra^{226} and RaD in bones

Subject	41B		42B		43B	
Bone	Ra^{226}, $\mu\mu g$/g ash	RaD, $\mu\mu c$/g ash	Ra^{226}, $\mu\mu g$/g ash	RaD, $\mu\mu c$/g ash	Ra^{226}, $\mu\mu g$/g ash	RaD, $\mu\mu c$/g ash
Tibia	0.012 ± 0.003	0.296 ± 0.013	0.025 ± 0.002	0.090 ± 0.009	0.026 ± 0.002	0.078 ± 0.006
Skull	0.070 ± 0.004	0.201 ± 0.015	0.051 ± 0.002	0.131 ± 0.009	0.032 ± 0.003	0.366 ± 0.019
	0.070 ± 0.004	0.419 ± 0.014	0.100 ± 0.007	- -	0.027 ± 0.003	1.33 ± 0.021
Joint (bone)	0.016 ± 0.001	0.152 ± 0.007	0.025 ± 0.002	0.083 ± 0.008	0.027 ± 0.003	0.071 ± 0.007
Jaw	0.012 ± 0.001	0.093 ± 0.005	0.028 ± 0.002	0.049 ± 0.004	0.030 ± 0.003	0.077 ± 0.006
Teeth	0.019 ± 0.003	0.018 ± 0.004	- -	- -	- -	- -

These results show great distinctions between Ra^{226} and RaD concentrations with bone type. The Ra^{226} is relatively constant in all the bones of a given individual, except for the skull which deviates by factors of two to five from the rest in two of the subjects. In subject 42B two samples of skull vary by a factor of two. These results are at variance with those of Walton et al.[1] who found concentrations in the skull to be slightly lower than the average for the other bones, and general uniformity throughout the skeleton, with the exception of a few subjects in whom extreme variations of more than a factor of two were seen between bones.

The RaD levels found here vary greatly from bone to bone, and in the cases where two samples of skull were analyzed, factors of 2 to 3.6 are found. In 43B all the bones have the same levels of RaD except the skull, which is much higher. The teeth in 41B have a very low level, due possibly to the small RaD turnover after the appearance of permanent dentition, namely ten years. Any RaD originally present would have decayed for 2.8 half-lives to a value one-seventh the original. If this original value is assumed to have been equal to the present average of the bones, 0.17 $\mu\mu c$/g ash, the value for the teeth, excluding skull, should now be 0.024 ± 0.012 $\mu\mu c$/g ash, in good agreement with the observed 0.018 ± 0.004 $\mu\mu c$/g ash.

The results suggest that perhaps analysis of the RaD concentration in trabecular bone, such as that present in a joint, may be used to give a value closer to the average of the body. The jaw may be used to estimate a minimum body burden. On the other hand, the values obtained for levels in the skull may be used to estimate the maximum body burden. A more extensive survey is needed, however, to establish these suggestions on a firmer basis.

These results do indicate that, due to variations in metabolism of various bones, and in intake rates with time, the RaD content of the whole body cannot be established with great assurance from the measurements on teeth or single bones.

The unusual variation in Ra^{226} content of the occipital bones of 41B and 42B indicate a residence history that is not typical of the specimens measured by Walton et al.,[1] who found little variation between the values of skull and other bones in 11 subjects. The pattern in 43B, however, is in full agreement. The causes of these anomalies remain to be discovered.

Reference

1. Walton, A., Kologrivov, R. and Kulp, J. L. The Concentration and Distribution of Radium in the Normal Human Skeleton. Health Phys. 1 409 (1959).

Appendix III

THE RaD CONTENT OF SOME POTABLE WATERS IN ILLINOIS

Richard B. Holtzman

The RaD (Pb^{210}) content of some potable waters from Illinois communities was determined and compared to the Ra^{226} content. Although RaD is a member of the Ra^{226} decay series, one would not expect it to be in equilibrium with Ra^{226} because of their different chemical properties. One- or two-liter samples of water were obtained from various towns. The Ra^{226} concentration was determined by H. F. Lucas using the radon emanation method.(1) To determine the RaD and RaF content, the samples were evaporated to a small volume and fumed with 25 ml of 72% $HClO_4$. Forty milliliters of HCl were added, 10 ml at a time between fumings, to remove nitrates present. The samples were then prepared, plated on silver disks, and counted for α-ray activity according to the procedure in Appendix I.

The Bateman equation for the growth of a daughter RaF from RaD and Ra^{226} was used to determine the RaD present at the time the water was drawn from the well, namely at time t = 0:

$$A_3 = A_1^0 \left[\frac{\lambda_2 \lambda_3 \, e^{-\lambda_1 T}}{(\lambda_2 - \lambda_1)(\lambda_3 - \lambda_1)} + \frac{\lambda_2 \lambda_3 \, e^{-\lambda_2 T}}{(\lambda_1 - \lambda_2)(\lambda_3 - \lambda_2)} + \frac{\lambda_2 \lambda_3 \, e^{-\lambda_3 T}}{(\lambda_1 - \lambda_3)(\lambda_2 - \lambda_3)} \right]$$

$$+ \frac{\lambda_3 A_2^0 \left(e^{-\lambda_2 T} - e^{-\lambda_3 T} \right)}{(\lambda_3 - \lambda_2)} \qquad (1)$$

where the subscripts 1, 2, and 3 refer to Ra^{226}, RaD and RaF, respectively and:

A_i^0 = activities at time t = 0

A_i = activities at time of measurement t = T

λ_i = decay constants

The growth and decay of the short-lived intermediate products are neglected and $e^{-\lambda_1 t} \sim 1$. Solving for the initial RaD activity A_2^0 one obtains:

$$A_2^0 = \left\{ A_3 - A_1^0 \lambda_2 \lambda_3 \left[\frac{1}{(\lambda_2 - \lambda_1)(\lambda_3 - \lambda_1)} + \frac{e^{-\lambda_2 t}}{(\lambda_1 - \lambda_2)(\lambda_3 - \lambda_2)} + \frac{e^{-\lambda_3 t}}{(\lambda_1 - \lambda_3)(\lambda_2 - \lambda_3)} \right] \right\}$$

$$\left\{ \frac{\lambda_3 \quad \lambda_2}{\lambda_3 \left(e^{-\lambda_2 t} - e^{-\lambda_3 t} \right)} \right\} \qquad (2)$$

The value of Ra^{226} must be adjusted for the loss of Rn^{222} from the sample during storage prior to measurement; this value is obtained by multiplying A_1^0 by the fraction of Rn^{222} retained in the sample.

The minimum radon retention in stored water, expected from the partition coefficient between air and water, is about 90% under the following conditions:

1. The air and water volumes are equal.
2. Thermodynamic equilibrium is attained between the gas and liquid phases.
3. Radon leakage from the container is negligible.

In the actual samples, however, confinement of the radon to the neck of the nearly filled storage bottles caused it to remain in the liquid phase in the absence of stirring.

In order to make a limiting estimate as to the equilibrium state of Rn^{222} continually emanating from a solution under non-mixing conditions, a 550-ml round-bottom flask was half filled with water containing Ra^{226} and allowed to stand quietly until the attainment of radioactive equilibrium between Ra^{226} and Rn^{222}. Measurement of the Rn^{222} in the gas and liquid phases showed that only 73% of the radon was in the gas phase, rather than the 90% expected under conditions of good mixing. Hence, 73% may be considered to be an upper limit of the fraction escaping the liquid in the storage bottles since conditions were more favorable to retention in the bottles than the flask. On the other hand, the sample storage bottles were sealed by bakelite plastic caps with coated paper inserts which, like many other organic materials, may be permeable to radon. This would displace the equilibrium toward increased radon loss.

The data from the Cuba sample indicate a maximum radon retention of about 20 ± 10%. This was derived from calculations in which various retention values were assumed during the storage time. Higher retention values would have given negative concentrations for the original RaD contents of the water at the time of collection. As a compromise, a value of 25% Rn^{222} retention was assumed in all our calculations. Fortunately, most of the results are not sensitive to the Rn^{222} retention value because either the time between collection and measurement was short or the Ra^{226} concentration was small.

The results of the measurements are given in Table 24. There appears to be some correlation between the Ra^{226} and RaD contents of the waters as shown in Fig. 45, except that Peoria No. 2 and LaSalle are somewhat high, and Cuba is low in RaD. Additional extensive data are currently accumulating.

Table 24

RaD content of some potable waters

Origin (Illinois towns)	Time between collection and measurement (T), yrs.	Ra^{226}, $\mu\mu g/l.$	RaD (A_2^0), $\mu\mu c/l.$
Chicago, tap (filtered)	0	0.03(2)	0.003 ± 0.005
Argonne	0	0.08 ± 0.02	0.020 ± 0.010
Hennepin	2.5	0.19 ± 0.02	0.072 ± 0.017
Keithsburg	2.5	0.28 ± 0.02	0.072 ± 0.014
Peoria No. 12	0	~0.5	0.010 ± 0.010
Peoria No. 2	2.0	0.47 ± 0.04	0.24 ± 0.04
LaSalle	2.5	0.55 ± 0.02	0.23 ± 0.02
LaGrange No. 1	1.5	0.95 ± 0.02	0.075 ± 0.015
DeKalb	1.5	3.16 ± 0.06	0.051 ± 0.013
Rockford	2.5	3.65 ± 0.08	0.12 ± 0.05
Ottawa	2.0	6.60 ± 0.15	0.09 ± 0.02
Joliet	1.0	7.00 ± 0.14	0.04 ± 0.03
Lockport No. 2	1.0	11.4 ± 0.2	0.15 ± 0.03
Shannon	2.5	17.5 ± 0.3	0.39 ± 0.03
Cuba	2.0	23.2 ± 0.1	-0.09 ± 0.014

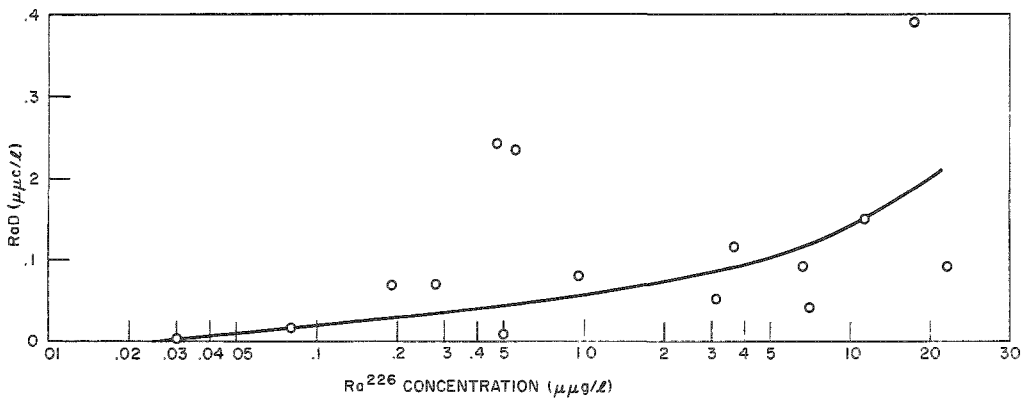

Fig. 45. RaD concentration in potable waters of Illinois as a function of Ra^{226} concentration.

References

1. Lucas, Henry F., and Ilcewicz, Frank H. Natural Radium-226 Content of Illinois Water Supplies. J. Am. Water Works Assoc. 50 1523 (1958).

2. Hursh, J. B. Radium Content of Public Water Supplies. J. Am. Water Works Assoc. 46 43 (1954).

CONVECTIVE TURBULENCE WIND TUNNEL PROJECT

G. H. Strom* and E. J. Kaplin**

Introduction

The current series of wind tunnel experiments, a continuation of earlier studies,[1,2,3] has the objective of developing apparatus and techniques for performing scale model smoke diffusion experiments with varying thermal stability and correlating the results with full-scale data obtained at the Argonne National Laboratory. These studies were conducted at New York University under Argonne subcontract #31-109-39-743.

Results of earlier experiments showed the need for further modifications and additions to wind tunnel apparatus. These have been made, and a substantial improvement in test results has been obtained through the reduction of side effects, lengthening of the period over which constant test conditions can be maintained, and the introduction of additional control over airstream turbulence.

Apparatus

The test section of the wind tunnel is shown schematically in Fig. 46.

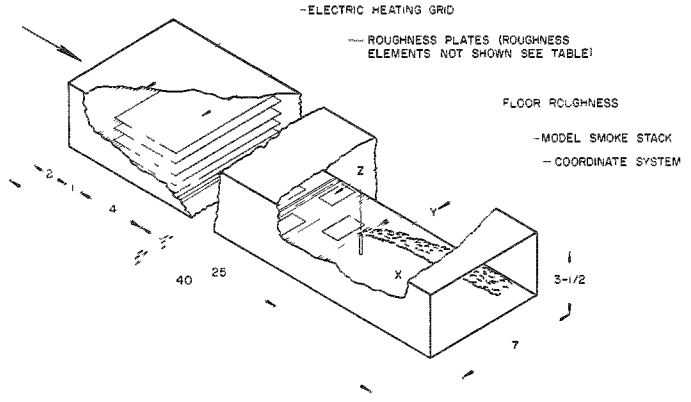

Fig. 46.
Wind tunnel test section.

---

*Resident Research Associate, Argonne National Laboratory, summer 1955-58, 1960. Professor of Aeronautics, New York University, New York.

**Resident Research Associate, Argonne National Laboratory, summer 1959. Associate Research Scientist, New York University, New York.

Other characteristics of the wind tunnel are given in references (1), (2), and (3). The various parts of the wind tunnel upstream of the test section serve to produce an airstream uniform in velocity and temperature where it enters the test section. In the test section the air first passes through a heating grid which produces the desired initial temperature profile. Control of the profile is obtained through adjustment of the electrical input to the individual wires of the grid. The air then passes through an array of roughness plates which control the velocity and turbulence profile. The plates are $\frac{1}{8}$-inch aluminum alloy sheets 4 feet wide (in the direction of air motion) which span the airstream. A sheet of $\frac{1}{2}$-inch plywood rests on the floor and forms under the plates a floor surface $\frac{1}{2}$ inch above the permanent floor of the test section. The roughness elements are rectangular in shape, span the airstream and are located on the upper surface of each plate. They are equally spaced with the first and last elements at the upstream and downstream edges of the plate. On the two upper plates the single element is located 11 inches from the downstream edge. Various dimensions are given in Table 25.

Table 25

Dimensions of roughness plates*

Plate No.	Vertical distance from test section floor to top surface of plate	Number of roughness elements	Cross-section dimensions of roughness elements	
			Width	Height
0 (Floor surface under plates)	0.5	-	coarse sand paper	
1	1.7	96	0.19	0.19
2	3.8	18	0.5	0.5
3	6.9	7	0.5	0.85
4	11.9	3	0.75	1.3
5	17.7	2	0.75	1.8
6	25.2	1	0.75	2.5
7	33.1	1	0.75	1.3

*All dimensions are given in inches.

Further control of velocity and temperature of the airstream is obtained with adjustment of floor roughness(2) and temperature. Surface temperature of the floor, ceiling, and first third of walls is controllable. Temperature was measured with thermocouples and velocity with a hot wire anemometer.(2)

Two Crown Graphic 4 x 5 cameras were used to photograph the smoke plume from the side and from above. They were located outside the test section as described in reference (2). Several 24-inch tubular type electronic flash lamps were used to illuminate the smoke plume. They were placed in diagonally opposite corners of the test section.

The model smoke stack was constructed to a scale of 1 inch = 8 feet (1:96). Its height is 13.75 inches and inside diameter is 0.182 inch. The corresponding full-scale dimensions are 110 feet and 17.5 inches, respectively.

Test Procedure

The sizes and arrangement of the roughness plates was determined with a series of velocity profile experiments. The plates serve to control the initial (upstream) velocity and turbulence profiles through the size and number of roughness elements and spacing of the plates. In selecting the roughness elements it was assumed that the scale of turbulence was dependent primarily on the size of roughness elements and the intensity on the number of elements. In order to obtain an increase in turbulence scale with elevation, larger elements were used on the upper plates. To obtain greater intensity at the lower elevations, a greater number of elements was used on the lower plates. This arrangement tends to produce a turbulence distribution similar to that of the atmosphere. Plate spacing is another variable which affects the number of elements exposed to a given section of the airstream. Developmental work leading up to the use of roughness plates is given in reference (3). The procedure described therein was extended to include size of roughness elements as an additional variable.

Plate spacing was used primarily to give the desired velocity profile and was adjusted by trial to give a power law variation in accordance with the following equation:

$$\frac{u}{u_0} = \left(\frac{z}{z_0}\right)^{\frac{n}{2-n}} \qquad (1)$$

where u is the velocity at elevation z and n is a turbulence index. Field experiments were shown to have an average value of n in the range of 0.3 to 0.35 for neutral conditions (see Fig. 47) and the plates were adjusted to give this result. The value of n changes with stability, but only one arrangement was used in this series since the adjustment procedure was time consuming and little was known about how effective would be the use of roughness plates in smoke diffusion experiments.

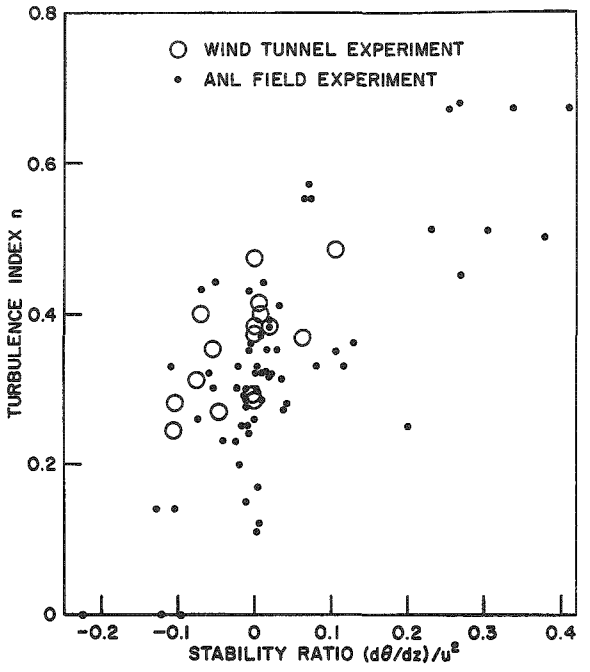

Fig. 47
Comparison of model and prototype turbulence index at station x = 0.

In the diffusion experiments a run consisted of measuring the velocity and temperature profiles at a number of stations (Table 26) and photographing the smoke plume emitting from the model stack(Figs. 48-50).

Table 26

Diffusion experiment test results*

Run No.	$\frac{dT}{dz}$** °C/100 m, x = 0	x = - 439 m		x = 0		Plume half width in vertical plane, m, at x = 100 m	Plume half width in horizontal plane, m, at x = 50 m
		u, m/sec, z = 36.6 m	$\frac{n}{2-n}$	u, m/sec, z = 36.6 m	$\frac{n}{2-n}$		
1	-0.94	3.41	0.235	3.44	0.260	9.9	7.4
2	-1.00	3.79	0.180	3.94	0.230	10.8	7.1
3	-1.00	2.60	0.102	2.39	0.170	16.3	9.6
4	-2.14	4.90	0.185	4.60	0.215	19.0	9.4
5	-1.76	3.28	0.190	3.26	0.250	26.8	13.0
6	-1.77	3.88	0.140	4.00	0.155	17.3	9.6
7	-2.90	4.54	0.130	4.30	0.165	20.3	9.2
8	-1.72	3.10	0.200	3.11	0.185	23.4	9.8
9	-1.73	2.54	0.165	2.63	0.140	23.1	11.8
10	+0.06	3.17	0.190	3.14	0.320	7.1	5.6
11	-0.93	2.75	0.240	2.96	0.250	8.3	6.0
12	-0.81	2.63	0.165	2.84	0.235	11.4	6.8
13	-0.13	3.49	0.170	3.67	0.225	6.3	4.9
14	-1.00	3.34	0.220	3.44	0.310	13.8	7.5
15	-1.00	3.88	0.215	3.88	0.240	14.0	6.6
16	-0.94	5.25	0.170	5.44	0.166	8.7	4.7

*All quantities are given in terms of full scale equivalents.

**u = velocity at elevation z.

$\frac{dT}{dz}$ = the temperature gradient.

x = see Fig. 46.

n = a turbulence index.

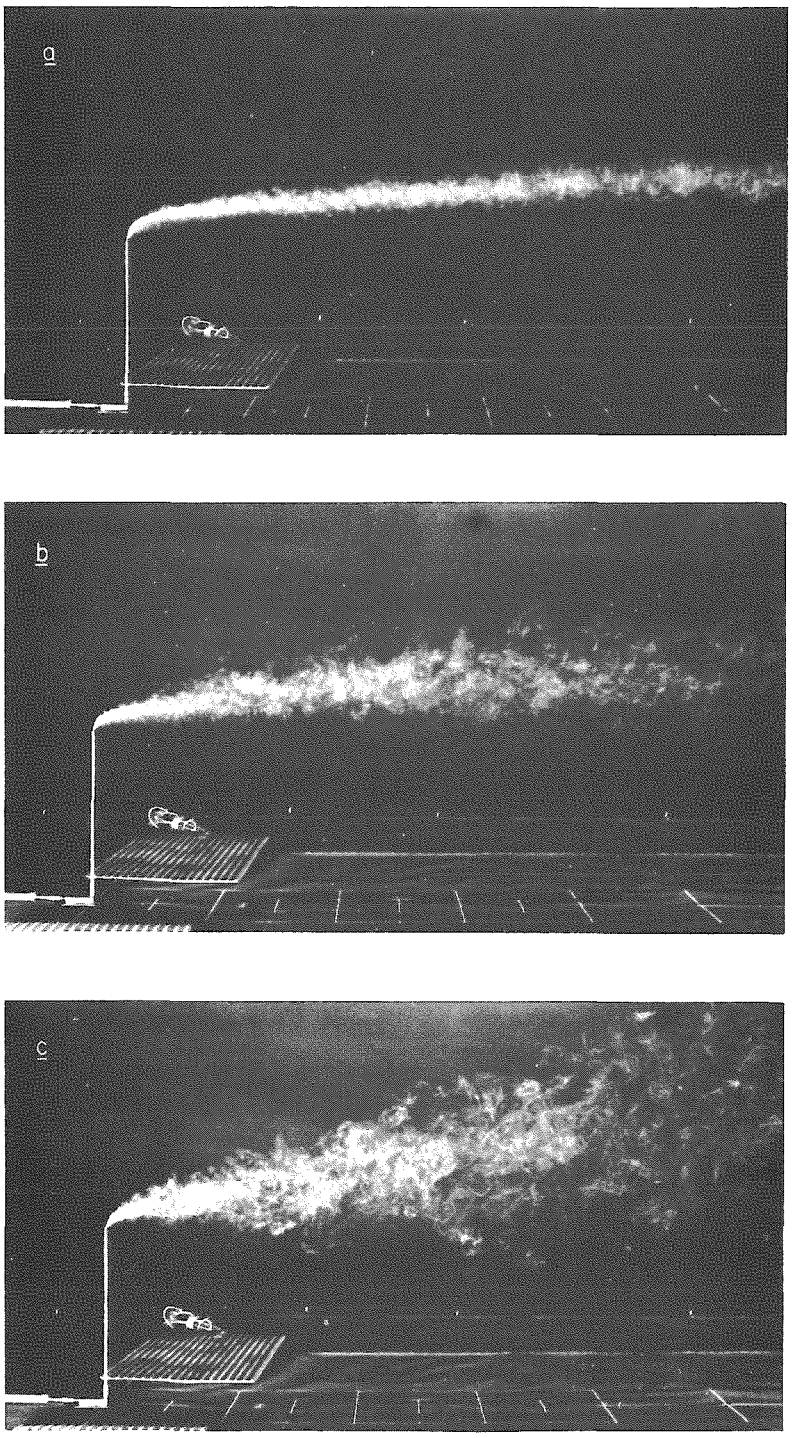

Fig. 48. Multiple exposure photographs of smoke plume taken from the side. a) Stable, b) neutral and c) unstable thermal conditions, top to bottom (Run numbers 10, 15, and 7).

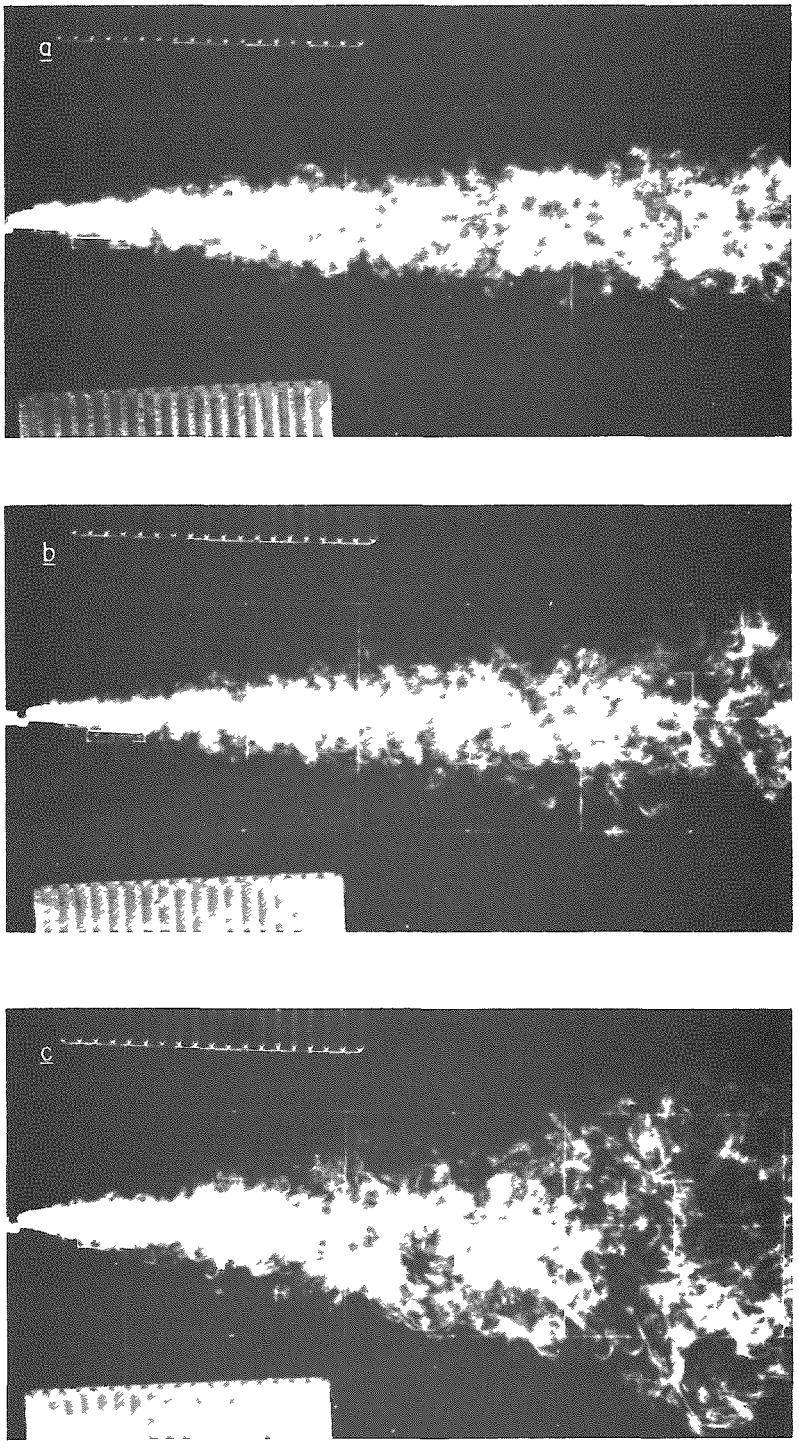

Fig. 49. Multiple exposure photographs of smoke plume taken from above. a) Stable, b) neutral and c) unstable thermal conditions.

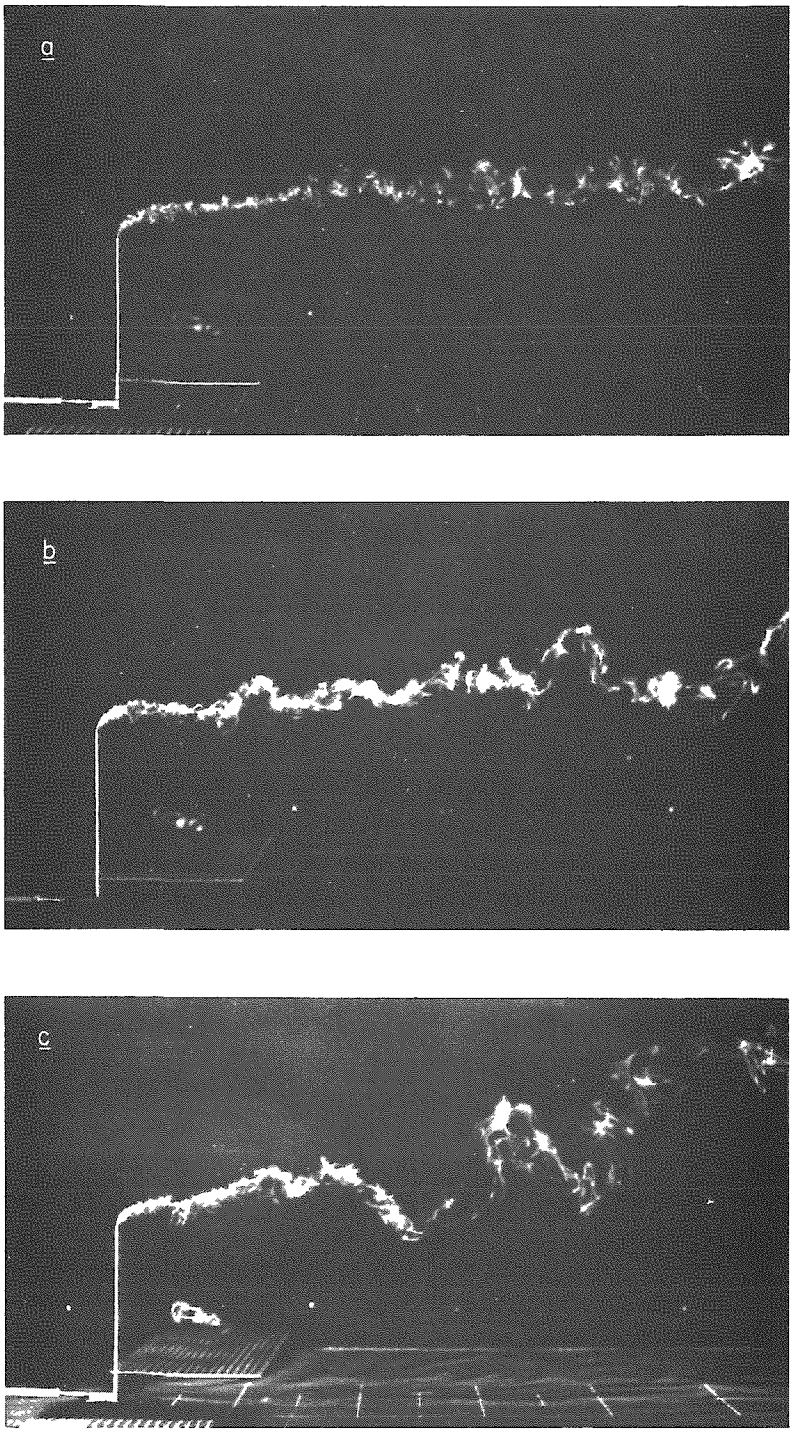

Fig. 50. Single exposure photographs of smoke plume taken from the side. a) Stable, b) neutral and c) unstable thermal conditions.

Floor, ceiling, wall and heating grid temperatures, and air speed were adjusted to give the desired flow conditions. The objective was to obtain a given temperature profile at a certain velocity level. Since the adjustment procedure was quite intricate and time consuming, the run was started when equilibrium conditions reasonably close to the desired values were reached. Floor temperatures were set to be the same as that of the adjacent airstream as it left the upstream control apparatus. The ceiling temperature was set to be a little higher than that of the adjacent airstream in order that the top layer be stable and not induce undesired convective air currents.

The measurement of temperature and velocity profiles was started with the first upstream station and continued in the downwind direction. After the last downstream station was completed, the x = -10-foot station was retested as a check on whether conditions had changed. The elapsed time for a complete test run was approximately three hours.

Multiple exposure photographs were taken of the smoke plume (Figs. 48 and 49) to record its geometric characteristics. These were obtained by giving each film 16 flash exposures at two-second intervals (the minimum interval obtainable with this equipment). Single exposure photographs were also taken (Fig. 50). Photographs were taken three times during a run; first near the beginning, after the measurement of a profile showed that the flow had reached equilibrium, then near the middle of the run, and finally at the end. For all experiments the stack gas ejection speed was set at 4.08 feet per second which is equivalent to a full scale value of 40 feet per second. The helium-to-air ratio was set at a value which gives a stack gas density equivalent to that obtained at a gas temperature of 140°F with ambient air temperature of 80°F.

Test Results

Various temperature, velocity and smoke plume characteristics are summarized in Table 26. Graphs of test measurements and smoke plume photographs shown in Figs. 51-53, and 48-50 are representative of three conditions of thermal stability. In Table 26 the data are given in terms of full scale values which were obtained from the model measurements by means of the following scaling equations:[1,2,4]

$$l_p = 96\, l_m \tag{2}$$

$$V_p = \sqrt{96}\, V_m \tag{3}$$

$$\left(\frac{dT}{dz}\right)_p = \frac{1}{96}\left[\left(\frac{dT}{dz}\right)_m + \Gamma\right] - \Gamma \tag{4}$$

where l is a linear dimension, V a speed (wind speed or stack gas ejection speed), dT/dz the temperature gradient and Γ the adiabatic lapse rate (expressed as a positive number). The subscripts p and m refer to prototype and model, respectively.

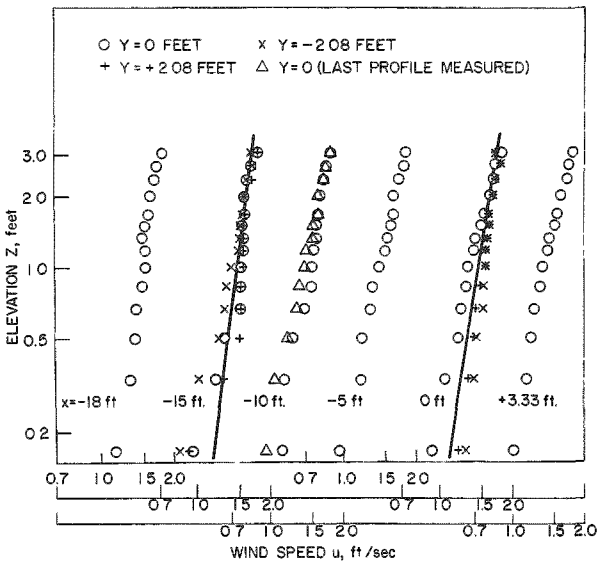

Fig. 51a. Wind speed profiles for unstable thermal condition. Run No. 7.

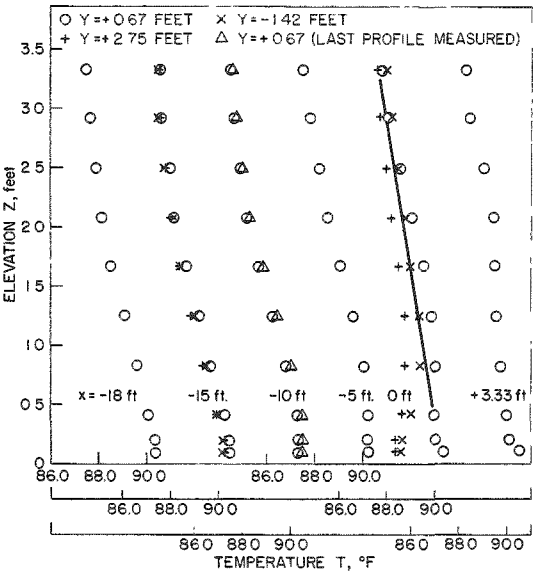

Fig. 51b. Temperature profiles for unstable thermal condition. Run No. 7.

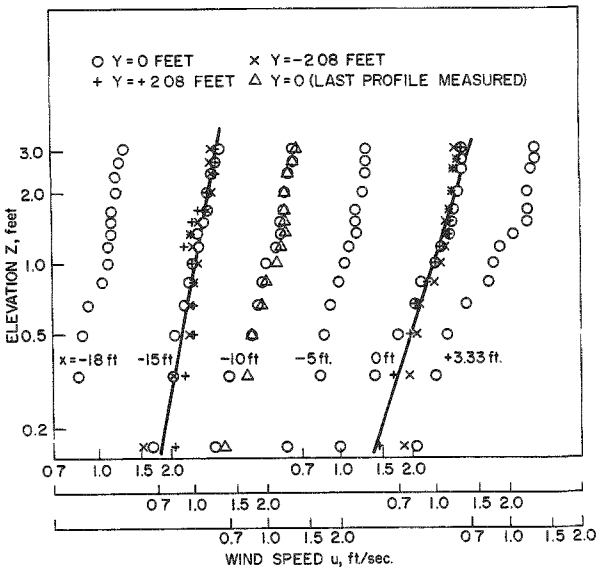

Fig. 52a. Wind speed profiles for stable thermal condition. Run No. 10.

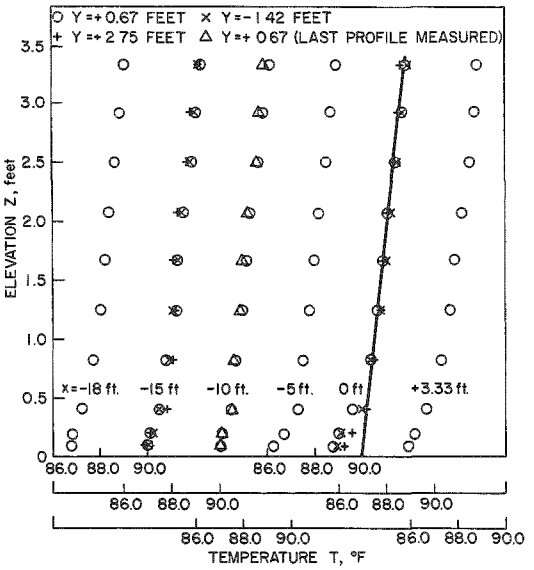

Fig. 52b. Temperature profiles for stable thermal condition. Run No. 10.

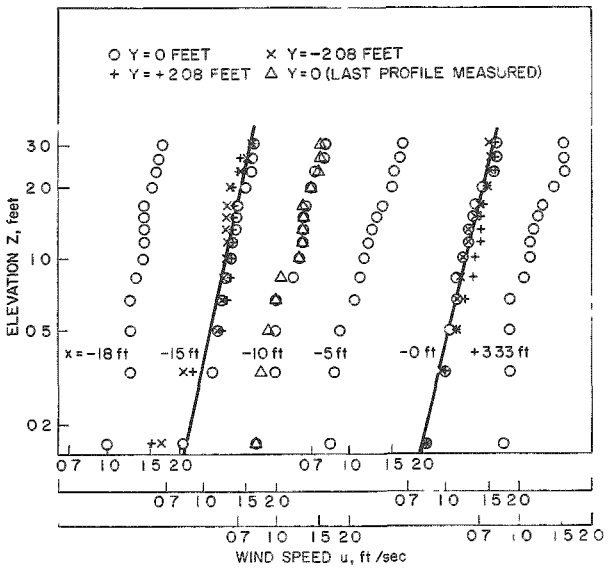

Fig. 53a. Wind speed profiles for neutral thermal condition. Run No. 15.

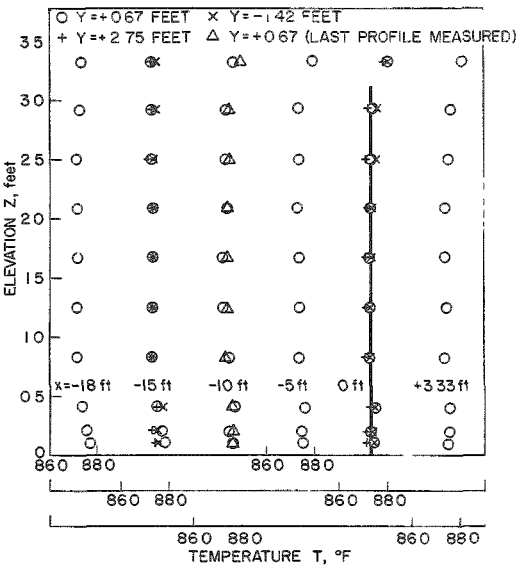

Fig. 53b. Temperature profiles for neutral thermal condition. Run No. 15.

The various temperature and velocity profile characteristics are taken from faired curves as shown in Figs. 51, 52, and 53. In drawing the temperature curves emphasis was placed on that part of the airstream between elevations of 1 foot and 2.5 feet, where the plume was usually located. Anomalies in floor surface temperature caused irregular features in the lowest part of the temperature profile which made it unsuitable for determination of temperature gradient.

Plume half widths were obtained from the multiple exposure photographs. Outlines of the plume were drawn on the negatives at the outer edge of the visible image and plume widths were measured. Suitable transformation was made to model scale. Plume widths were taken at downwind distances corresponding to 50 and 100 m (full scale) for the horizontal and vertical planes, respectively, since these were near the maximum distances covered on the negatives. Results obtained from the three negatives taken during a given run were averaged. There were only small differences among the three.

Discussion of Results

One of the more important results of this investigation is the comparison of plume half widths between model and prototype found in Figs. 54 and 55. Since thermal stability was one of the significant variables in these experiments, it was deemed valuable to use some measure of stability as

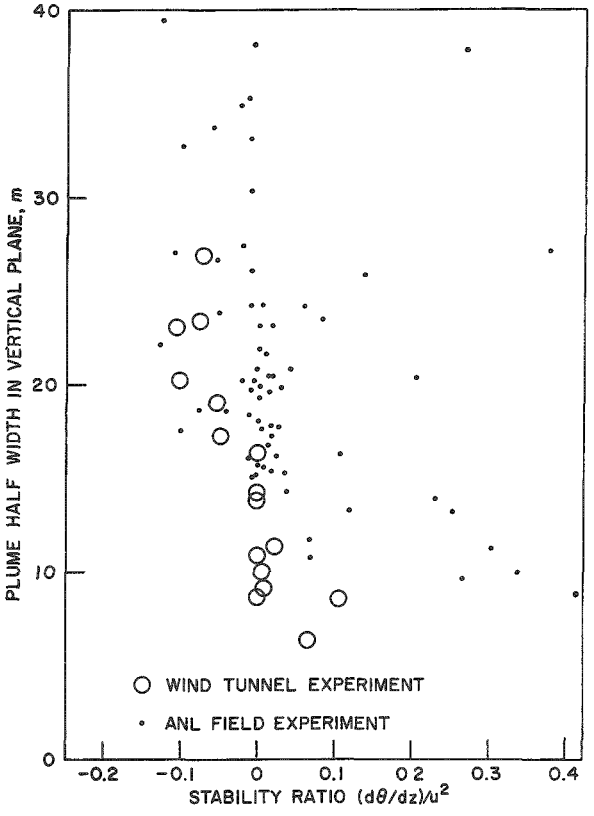

Fig. 54. Comparison of model and prototype plume half width in vertical plane at downwind distance of 100 m.

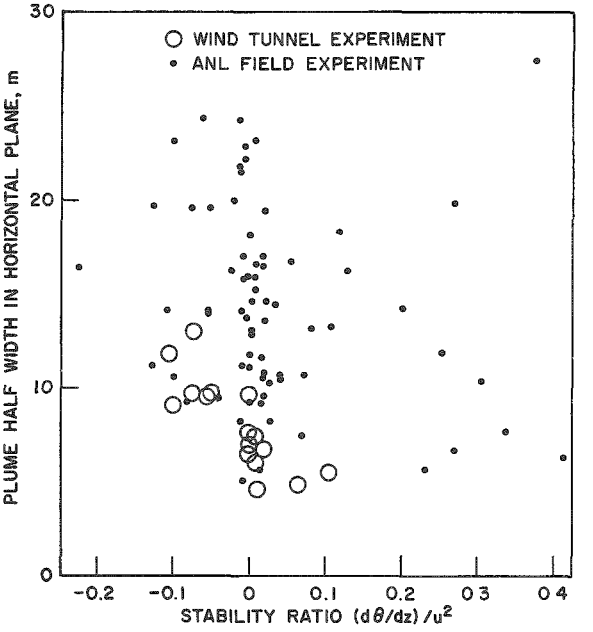

Fig. 55. Comparison of model and prototype plume half width in horizontal plane at downwind distance of 50 m.

the independent variable in the comparison graphs. Three variables were considered, namely, temperature gradient, Richardson number (based on velocity gradient), and stability ratio. Stability ratio is here defined as $(d\theta/dz)/u^2$ where $d\theta/dz$ is the potential temperature gradient and u is wind speed at 36.6 m elevation. The smoke plume is usually in the vicinity of this elevation. Of the three variables the best correlation was obtained with stability ratio although temperature gradient gave almost as good a result. Some of the low speed prototype test points had values outside the range of stability ratio shown in the figures.

There is a difference in the methods by which temperature gradient is defined for model and prototype. This may partially account for differences in results. In contrast with the model experiments where temperature gradient was obtained from the graphs of temperature profile at higher elevations, full scale temperature gradients are based on the temperature difference between the 144-foot and 5.5-foot elevations. The full scale temperatures do not usually show a linear variation with elevation, thus the gradient will depend on the elevation at which it is evaluated. Full scale

temperatures were not measured at the higher elevations used to evaluate the model gradients thus making direct comparison impossible. On the other hand, the model gradients could not be expressed in terms of readings at the lower elevations corresponding to those used in full scale because of spurious values caused by anomalies in floor surface temperatures.

Figures 54 and 55 show that for a given stability ratio the model plume widths are generally smaller than prototype with the greatest difference occurring in the horizontal plane. The minimum plume widths in the horizontal and vertical planes are approximately the same in model and prototype. This is not evident in Fig. 54 because the minimum prototype values occurred outside of the range of stability ratio shown. These results show improvement over the earlier series[2] where minimum plume width is somewhat smaller than prototype. The improvement is probably due in large measure to the introduction of the roughness plates which gave greater mechanical turbulence and increased the height of the boundary layer. The correlation between model and prototype is also better than in the earlier experiments. While model plume widths are smaller at a given stability ratio, the variation with stability is similar. Further adjustment of the roughness plates may increase model plume width, but there is a limit due to the finite dimensions of the wind tunnel airstream and the resulting suppression of any tendency to form long period and high amplitude fluctuations in air motion.

With the roughness plates the boundary layer was made sufficiently high to completely envelope the smoke plume. At the highest elevation of velocity measurement, approximately 3 feet (0.5 feet from the ceiling), the velocity was still increasing with elevation in most runs. In the earlier series where the boundary layer was allowed to develop naturally, the height at the smoke stack location was between 1.0 and 1.5 feet, which reached only the lower portion of the plume.

The velocity profiles show some evidence of a systematic influence of stability. As expressed in terms of a power law relationship (equation 1), the atmosphere shows the turbulence index n and the power law exponent $n/(2-n)$ to increase as stability increases. For proper simulation of velocity profiles in the wind tunnel a different arrangement of roughness plates should be used for each different stability condition so that appropriate initial upwind profiles may be obtained. In these experiments only one arrangement of plates was used, but the downwind profile at station $x = 0$ showed variations which correlate with stability as evidenced by the variation of turbulence index, n, in Fig. 47. There were, however, variations in the profiles at the upwind station $x = -15$, but these did not show any correlation with stability ratio. To minimize the effect that variation in the upwind profile may have on the downwind profiles, the ratio of downwind to upwind power law exponents are plotted in Fig. 56 where the effect of stability is still evident. Thus the airstream tends to change its profile in

the direction appropriate to the stability being simulated. The turbulence index n versus stability ratio in Fig. 47 also shows similar trends for model and prototype.

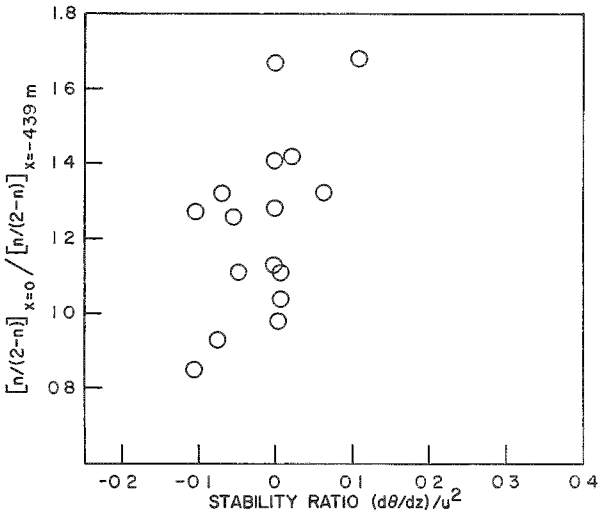

Fig. 56. Effect of stability ratio on development of power law exponent.

In most test runs there were only small variations of velocity in the crosswind direction as measured at stations x = -18 and 0. Runs number 3 and 7 showed at station x = 0 lower velocity near the center of the test section, while run number 13 showed higher velocity near the center. There was considerable variation in uniformity of profiles (smooth linear variation with z) as plotted on log-log coordinates. Such correlation with test variables as did exist showed more uniform profiles at higher wind speeds and, to a lesser extent, with stable conditions.

Temperature profiles remained nearly constant over the length of the test section except near floor and ceiling where surface temperatures had a marked influence. While the objective during a test run was to adjust floor surface temperature so as to maintain the local airstream temperature produced upstream at the heating grid and roughness plates, the large thermal lag in surface temperature control made this difficult. In the previous series of experiments[2] much difficulty was encountered with cold air currents which originated at the walls and flowed over the floor toward the center of the tunnel. This has been largely eliminated with the addition of wall temperature control in the upstream portion but there is still some evidence of this action in runs number 6, 7, and 8.

Conclusions

Convective turbulence significant to smoke plume diffusion can be obtained in scale model wind tunnel experiments with proper use of thermal and mechanical boundary controls. An array of roughness plates

located at the beginning of the test section raises the turbulence level sufficiently to obtain diffusion comparable in magnitude with that obtained in the atmosphere. Control of thermal boundary conditions affects convective turbulence in a manner which produces changes in plume diffusion similar to that found in the atmosphere.

Further development of techniques is expected to improve the correlation between model and prototype. Additional investigation of detailed experimental characteristics is needed for a better understanding of the phenomena involved and as an aid to theoretical studies. Measurement of turbulence characteristics should be carried out. Additional experiments should be conducted to broaden the range of test variables and increase the supply of information.

References

1. Strom, G. H. and Moses, H. Model Smoke Diffusion Experiment, Argonne National Laboratory, Radiological Physics Division Semiannual Report; ANL-5829 (February 1958). pp. 211-217.

2. Strom, G. H. and Kaplin, E. J. Convective Turbulence Wind Tunnel Project, Argonne National Laboratory, Radiological Physics Division Semiannual Report, ANL-5967 (May 1959) pp. 195-209.

3. Weiss, R. F. Atmospheric Boundary Layer Simulation Techniques for Smoke Diffusion Experiments. Argonne National Laboratory, Radiological Physics Division Semiannual Report, ANL-6104 (December 1959) pp. 116-124.

4. Strom, G. H. Scale Model Wind Tunnel Studies on Atmospheric Diffusion Phenomena. Proceedings of the Seventh Hydraulics Conference, State University of Iowa, 1959, Studies in Engineering, Bulletin 39, pp. 91-110.

COMPARISONS OF CALCULATED AND OBSERVED PLUME RISE

H. Moses, E. J. Kaplin,* and G. H. Strom**

I. Introduction

Information on the height to which the plume from a stack will rise in the atmosphere is of importance in calculating the resulting concentrations at ground level. There are at least six theoretical or empirical formulas one may use.(1-6) Unfortunately these yield results which may differ by an order of magnitude. Up to the present time there have been too few reliable measurements under varying stack and meteorological conditions to test these formulations adequately. This paper describes a comparison of three such formulas, those of Sutton, Holland, and Davidson and Bryant, with experimental data obtained by the Meteorology Group (7)

II. Equipment and Technique

Smoke plumes are obtained by injecting fog-oil particles into the air-stream of the 111-foot Meteorology Experimental Stack with a 4500 CFM $7\frac{1}{2}$ hp blower. The flow rate and fog-oil concentration are controlled by louvered dampers. A continuous record of the flow rate is obtained by a Hagan Ring Balance pressure differential recorder measuring the pressure drop across an orifice plate.

The effluent air-smoke temperature is measured by two pencil-type copper constantan thermocouples inserted into the stack, one at 31 feet above the base, and the other $\frac{1}{2}$ foot from the top. During each minute the temperature near the top of the stack is recorded for 20 seconds and that at 31 feet for 40 seconds, alternately on a Minneapolis-Honeywell potentiometer recorder

Speed and Crown Graphic cameras are used to photograph the plume, one located 40 feet from the foot of the stack points vertically; the other 1000 feet from the plume photographs its side. The vertically pointing camera is equipped with a 127-mm f4.7 Kodak Ektar lens the other with a 38-cm f5.6 Graflex Tele-Optar lens, both using Kodak Tri-X film. Sixteen exposures per film (one every 15 seconds) are made to observe the plume for 4 minutes.

---

*Resident Research Associate, Argonne National Laboratory, summer 1959; Assistant Research Scientist, New York University, New York.

**Resident Research Associate, Argonne National Laboratory, summers 1955-58; Professor of Aeronautical Engineering, New York University, New York.

The associated meteorological equipment used for this study is described elsewhere.(8) Wind speed and direction are measured by Aerovanes; temperature and stability are measured by copper constantan thermocouples, both mounted on the Meteorology Tower located 225 feet from the Meteorology Experimental Stack. The Esterline-Angus recorders for wind and Electronik Potentiometers for temperature are located in the Meteorology Building.

III. Analysis of the Data

From the photographs obtained by the two cameras it was possible to obtain the position in space of the top and bottom of the plume to a maximum distance of about 300 feet downwind from the stack. The center line of the plume at any distance from the stack was assumed to be at the average of the top and bottom plume heights. These values of the height of the plume's center line are used for comparison with the plume rise formulas. Samples of the data are presented graphically in Figs. 57a through 57d.

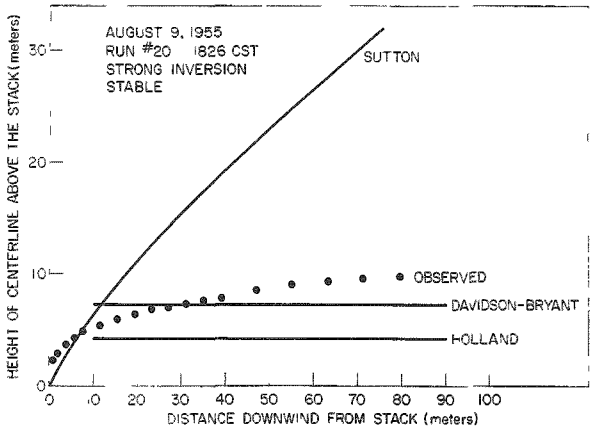

Fig. 57a

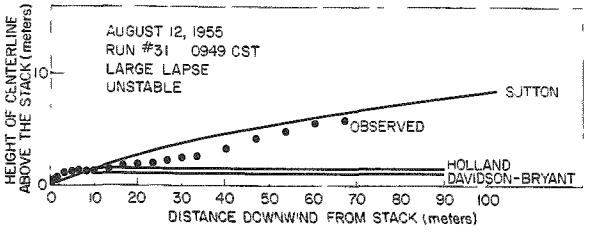

Fig. 57b

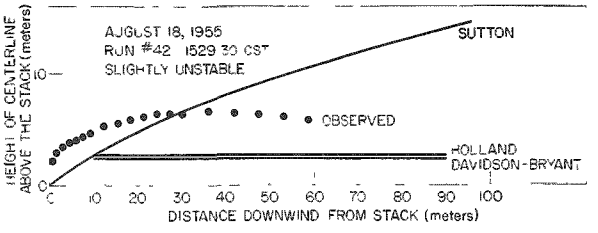

Fig. 57c

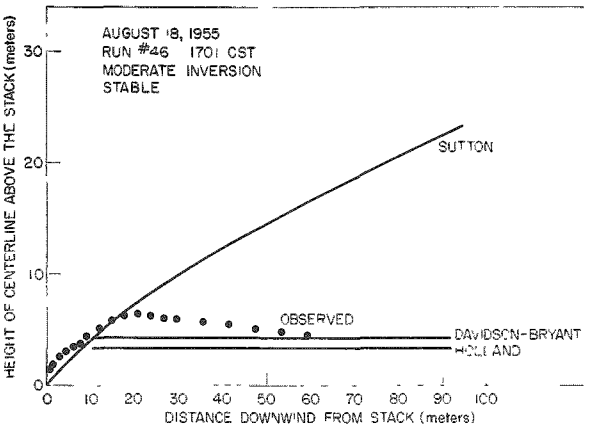

Fig. 57d

Fig. 57a-d. Height of plume rise

Wind speed values used in this study were obtained by plotting 5 readings (from 79 inches to 150 feet) on log-log paper and interpolating the 120-foot wind speed. Stability was obtained by measurements of the temperature difference between 144 and 5.5 feet above ground.

Meteorological and stack parameters for each run are shown in Table 27.

Table 27

Meteorological and stack parameters

Run No.	Date	Time CST	Meteorological Parameters			Emission Rate (CFM)	Stack Parameters		Effluent Gas Density lb./ft^3
			Wind Speed (MPS)	Lapse Rate °C/100M	Air Temp. (°K)		Stack Vel. (MPS)	Effluent Temp. (°K)	
18	8/ 9/55	1750	1.0	+ 2.8	297.9	4020	11.7	314.7	0.0704
19		1801-1/2	1.0	+ 3.6	298.2	3460	10.0	316.3	0.0702
20		1826	1.6	+ 4.7	297.6	4110	12.0	311.9	0.0709
26	8/10/55	1816	1.4	+ 0.5	298.2	2130	6.1	326.9	0.0693
27		1822	1.2	+ 0.5	298.2	1580	4.6	320.8	0.0717
28		1835-1/2	1.4	+ 2.4	297.8	2520	7.3	315.2	0.0706
30	8/12/55	0940-1/2	5.9	- 1.2	297.6	4140	12.2	309.7	0.0714
31		0949	5.2	- 1.2	297.6	3140	9.1	316.9	0.0703
32		0955	4.0	- 1.2	297.6	2010	5.8	324.7	0.0700
33		1001-1/2	4.5	- 1.4	297.5	1550	4.4	330.7	0.0699
42	8/18/55	1529-1/2	3.4	- 0.9	304.7	4160	12.0	319.7	0.0692
43		1535-1/2	3.8	- 0.7	304.8	3180	9.1	325.2	0.0686
44		1550	3.0	- 0.7	304.8	2060	5.9	322.4	0.0704
45		1622-1/2	2.2	0.0	304.0	4220	12.2	321.9	0.0689
46		1701	2.4	+ 0.5	303.2	4030	11.6	342.7	0.0682
101	9/ 7/55	1103	7.0	- 1.4	291.5	3450	10.0	314.7	0.0706
102		1108-1/2	6.2	- 1.7	291.4	2530	7.3	319.7	0.0703
103		1114	7.3	- 1.4	291.5	2530	7.3	319.7	0.0703
104		1119-1/2	6.2	- 1.4	291.5	1600	4.6	327.4	0.0703
111	9/12/55	0542-1/2	3.7	+12.3	280.1	4230	12.8	292.4	0.0755
112		0552	4.0	+11.0	281.0	4250	12.8	295.2	0.0747
113		0602	4.5	+13.0	281.4	4250	12.8	295.8	0.0746
115		0655-1/2	3.4	+ 6.4	282.1	4280	12.8	299.1	0.0738
116		0706	2.8	+ 5.2	282.7	4290	12.8	300.8	0.0734
117		0712-1/2	2.1	+ 3.6	283.2	4290	12.8	301.3	0.0732
118		0725	1.3	+ 0.5	282.2	4310	12.8	304.1	0.0726

IV. Discussion of Sutton's Plume Rise Equation

Sutton[1] presented the following expressions for calculating the height of plume rise:

$$w^3 = w_1^3 s \tag{1}$$

$$Z = \frac{3}{2}\frac{w_1}{u^3}\left[\cot\psi \csc\psi - \ln(\cot\psi + \csc\psi)\right] \tag{2}$$

where

$$w_1^3 = \frac{7}{3}\left\{\frac{g\ \Delta T\ r_0^2\ v_s}{T\ C}\right\} \tag{3}$$

from which it follows that

$$X = \frac{w_1^3}{u^3}\left[\frac{\cot^2 \psi - 2}{\sin \psi} + 2\right] \tag{4}$$

The origin of the cartesian coordinate system is taken at the top of the stack with:

X	distance downwind in meters
s	distance along the plume axis in meters
w	vertical velocity in meters per second
Z	vertical distance in meters
ψ	angle made by the tangent to the plume axis with the X axis
g	acceleration of gravity assumed to be 9.8 meters/sec^2
ΔT	temperature difference between the stack gas and the atmosphere (°K)
r_0	internal radius of the stack in meters
v_s	stack velocity in meters per second
T	ambient air temperature (°K)
C	Sutton's diffusion parameter in (meters)$^{\frac{n}{2}}$ where n is another diffusion parameter
u	wind in meters per second

For the computations, C and n were assigned the values shown in Table 28 based on the recommendations of "Meteorology and Atomic Energy"[9] for a level of 110 feet.

Sutton derives the expression for the radius of the plume, r, as:

$$r = 1.5C\ Z^{\frac{2-n}{2}} \tag{5}$$

A virtual origin was assumed at a distance, Z_0, below stack top for which r equalled r_0, the stack radius. The distance of virtual origin below the stack top (Z_0) was calculated from the equation

$$Z_0 = \left(\frac{r_0}{1.5C}\right)^{\frac{2}{2-n}} \tag{6}$$

Table 28

Selected Sutton parameters

Stability		$C(\text{meters})^{\frac{n}{2}}$	n
Large lapse	$\frac{\partial T}{\partial z} \leq -1°C/100$ meters	.20	.20
Isothermal or small lapse	$0 \geq \frac{\partial T}{\partial z} > -1°C/100$ meters	.11	.25
Moderate inversion	$0 < \frac{\partial T}{\partial z} < 2°C/100$ meters	.07	.33
Strong inversion	$\frac{\partial T}{\partial z} \geq 2°C/100$ meters	.06	.50

If the theoretical plume were plotted from the virtual origin, the plume axis would cross the level corresponding to the stack top, the zero level, a distance downwind from the stack. This, of course, was unreal. The entire theoretical plume was translated upwind so that it crossed the top of the stack. This correction still presents inherent difficulties since its inclination at the stack top differs from the virtual inclination of the actual plume. Nevertheless, this correction provides a better fit for the data.

V. Discussion of Holland's Plume Rise Equation

Holland[2] presented the following expression for calculating the height above the stack, Δh, to which a plume will rise:

$$\Delta h = \frac{1.5\, v_s d + 4 \times 10^{-5} Q}{u} \qquad (7)$$

where

v_s is the stack velocity in meters per second

d is the inside stack diameter in meters

Q is the heat emission rate in calories per second

and u is the wind speed in meters per second.

This formula is a modification of one presented by Rupp, Beall, Bornwasser and Johnson[3] based on wind tunnel tests aimed at predicting the behavior of the Oak Ridge X-10 reactor cooling air exhaust. The

formula by Rupp et al. contained a momentum term only. Based on height of rise data from three stacks, two operated by Oak Ridge and a third by the Tennessee Valley Authority, Holland introduced an empirical buoyancy term, $\frac{4 \times 10^{-5} Q}{u}$, to reduce the scatter in his data. Since the height of plume rise depends on atmospheric stability as well as the factors in his equation, Holland suggests that stability can be taken into account by adding to the mean height 10 to 20 per cent in lapse conditions and subtracting a like amount in inversions. This correction was applied to the calculations used to plot the Holland curves in Figs. 57a to 57d.

VI. The Davidson-Bryant Formula

Using data obtained from Bryant's wind tunnel experiments,[10] Davidson derived the following empirical expression:[4]

$$\Delta h = d\left(\frac{v_s}{u}\right)^{1.4} \left(1 + \frac{\Delta T}{T}\right) \qquad (8)$$

where

- Δh rise of the plume above the stack in meters
- d inside stack diameter in meters
- v_s stack velocity in meters per second
- u wind speed in meters per second
- ΔT temperature excess of effluent gas over ambient temperature (°K)
- T ambient air temperature (°K).

This expression, like that of Holland, does not consider stability, and the calculated values are too low.[2] Nevertheless, it has been used widely, probably because it is simple to apply.

VII. Discussion of Results

There is no clear agreement among the authors concerning a definition of plume rise. Sutton[1] implies that the plume may be considered horizontal when its inclination is less than 10 degrees. Holland[2] indicates his value for height of rise in "the height at which the plume levels off." Similarly, Davidson and Bryant[4] indicate that the height of rise refers to the rise a short distance from the stack where the plume levels off.

In this study it was attempted to define the height of rise as the height at which the plume inclination falls to 5 or 10 degrees. Such a criterion was found to be unrepresentative since the center line has minor perturbations on it as may be seen in Figs. 57a to 57d. It was, therefore, decided to make the comparisons with the observed heights at both 30 and 60 meters from the stack.

Only 19 of the 26 cases were measured to 60 meters; in these cases the slope of the plume in the 30 to 60 meter interval was less than 10 degrees and in 13 of these the slope was less than 5 degrees. Of the 7 runs in which the plumes were not measured to 60 meters, the slope at 30 meters was less than 10 degrees in 5 runs but somewhat greater in the other two.

To compare calculated with observed plume rises, scatter diagrams were drawn for the data at both 30 and 60 meters (Figs. 58 through 63). The atmospheric stability which prevailed during each run was denoted by the symbol used for the plotted points and the wind speed by the number appearing next to each symbol. Also plotted is the line through the origin of the graph inclined 45 degrees to the horizontal. The scatter of the points about this line is a measure of the validity of a formula since they would all lie on this line if the formula were perfect. Also appearing on the scatter diagrams is the least squares regression line with the formula value as the independent variable. Because the scatter of points about this line is smaller than that about any other line it may be used as a practical tool to calculate plume rises based on the formula with improved accuracy.

The graphs show that there is a considerable scatter of points and that the scatter at 60 meters exceeds that at 30 meters. It is also evident from these figures that the 45-degree line provides a rather poor fit of the data

At both 30 and 60 meters the root mean square deviations about the 45-degree line are largest for the Sutton formula and smallest for the Davidson-Bryant formula. The dispersion about the regression line is substantially smaller, as seen from Table 29. Although the values for the standard error of estimate (the dispersion about the regression line) are smallest for the Davidson-Bryant expression, the values obtained by the Holland formula are not significantly different. It remains to be seen whether for a wider range of experimental conditions, such as different stack diameters, wind speeds, and stack speeds, the difference in the standard error of estimate of the two formulas will become significant.

The histograms of Figs. 64 through 69 represent another way of comparing the observations with the computed values. As seen from the histograms and Table 29, at both 30 and 60 meters the Davidson-Bryant values provide the smallest mean difference between computed and experimental values. Nevertheless, these values are too low, as are those of the

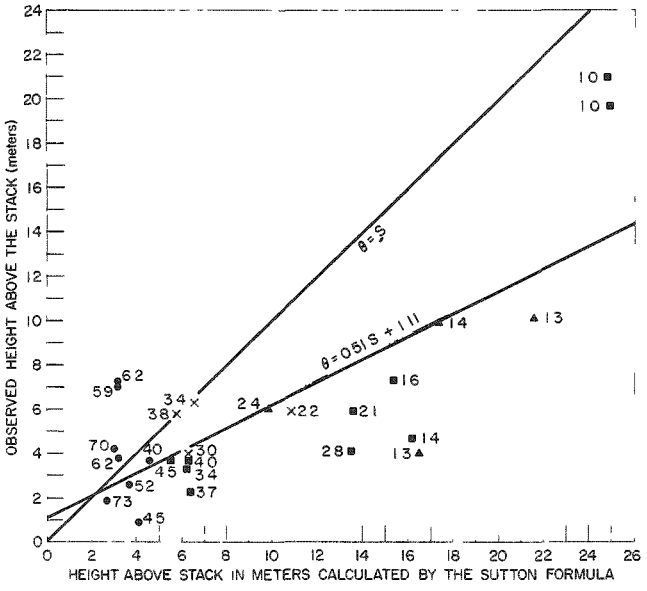

Fig. 58

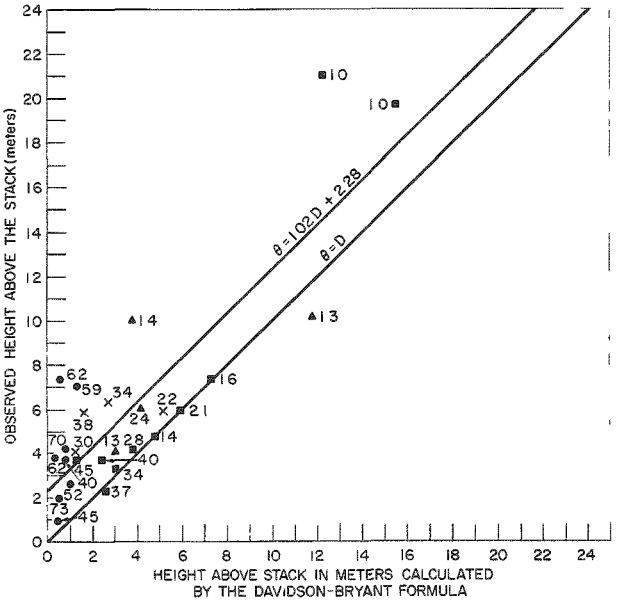

Fig. 59

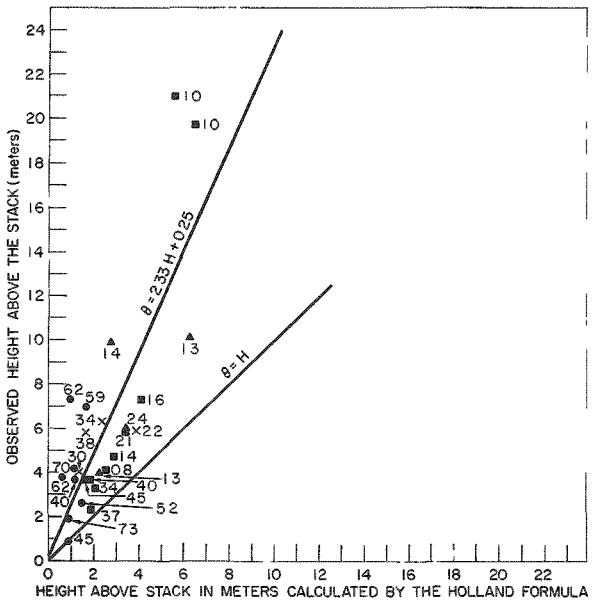

Fig. 60

Figs. 58, 59, and 60. Observed height at 30 meters versus calculated height. ● large lapse; x isothermal or small lapse; ▲ moderate inversion; ■ strong inversion; θ ordinate, the dependent variable; S, Sutton value; D, Davidson-Bryant value; H, Holland value. Numbers at points refer to wind speed in meters per second.

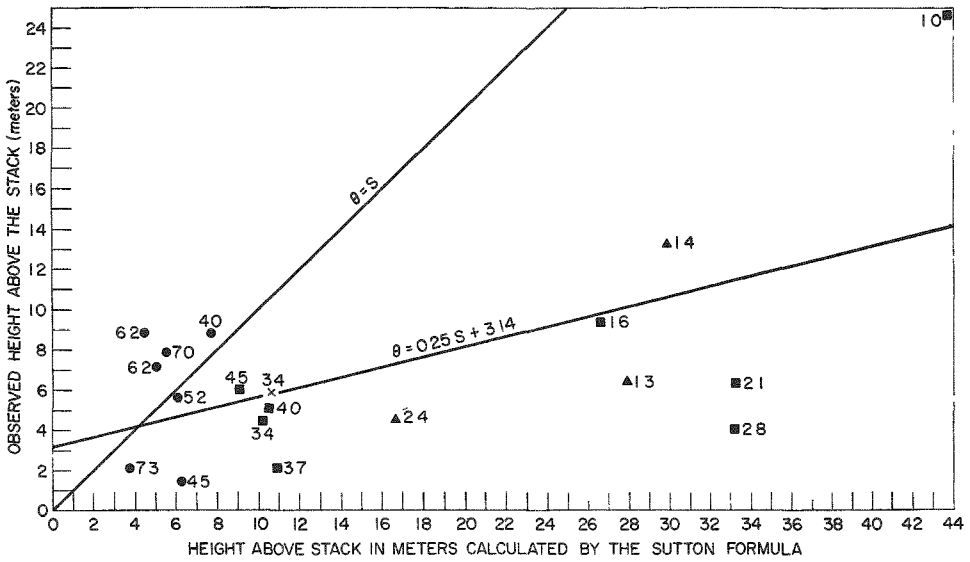

Fig. 61

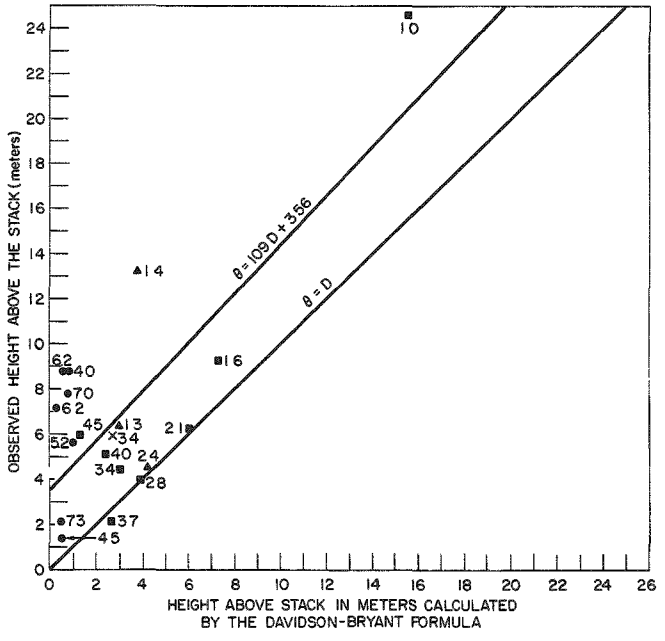

Fig. 62

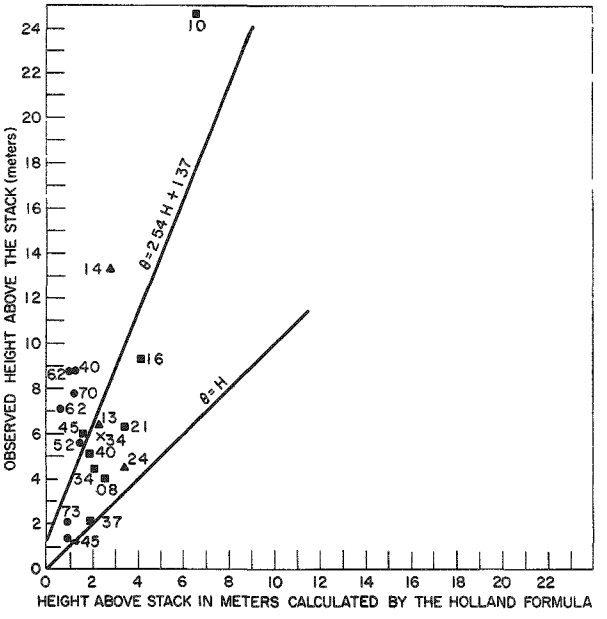

Fig. 63

Figs. 61, 62, and 63. Observed height at 60 meters versus calculated height. ● large lapse; x isothermal or small lapse; ▲ moderate inversion; ■ strong inversion; θ ordinate, the dependent variable; S, sutton value; D, Davidson-Bryant value; H, Holland value. Numbers at points refer to wind speed in meters per second.

Table 29

Statistical Summary of Calculated and Observed Plume Heights

Parameter Units are in meters	At 30 Meters from Stack Number of cases = 26				At 60 Meters from Stack Number of cases = 19			
	Sutton	Davidson-Bryant	Holland	Observed	Sutton	Davidson-Bryant	Holland	Observed
Mean height	9.8	3.8	2.6	6.1	15.8	3.2	2.2	7.0
Standard deviation	6.8	3.9	1.6	4.6	12.0	3.5	1.4	5.0
Calculated minus observed values								
Average Difference	3.7	-2.4	- 3.6		8.8	-3.8	- 4.8	
Maximum Difference	12.5	-8.8	-15.4		29.1	-9.4	-18.1	
Correlation coefficient [calculated vs. observed values]	0.75	0.85	0.80		0.59	0.76	0.71	
Root mean square deviation of observed heights about 45° line (σ_{45})	5.7	3.4	5.0		13.2	5.0	6.3	
Standard error of estimate, $S\theta$ (Root mean square deviation of observed heights about regression line)	3.1	2.5	2.8		4.0	3.2	3.5	
$1 - \frac{S_\theta}{\sigma_{45}}$	0.47	0.28	0.44		0.70	0.37	0.44	

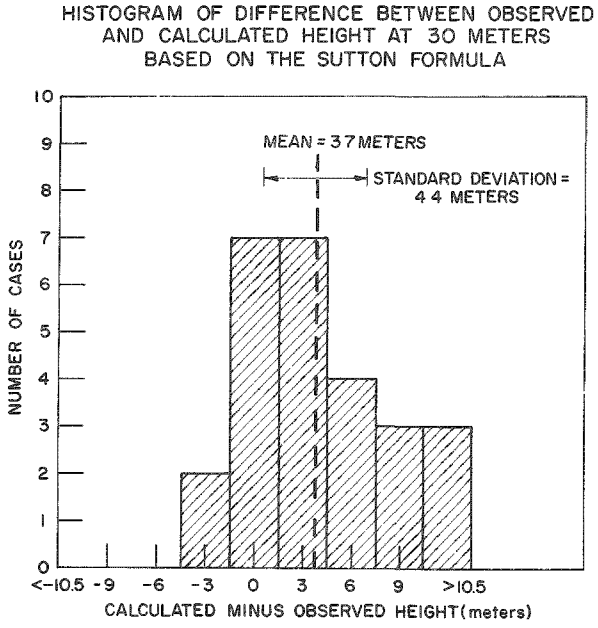

Fig. 64

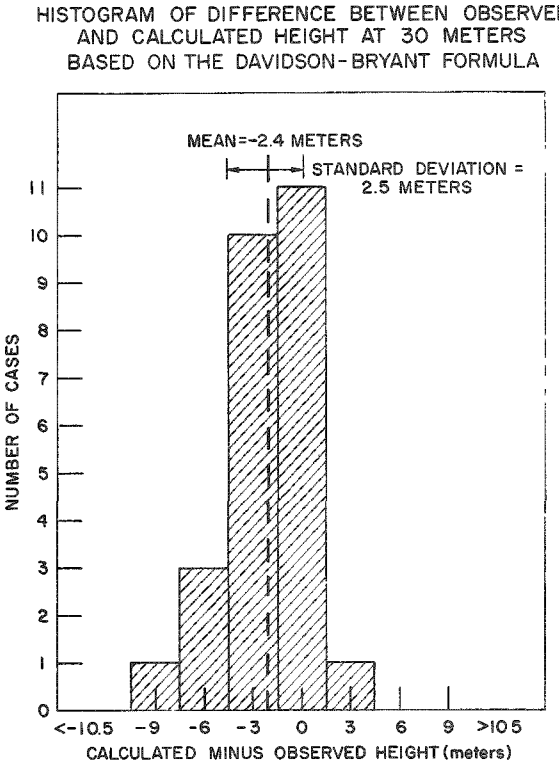

Fig. 65

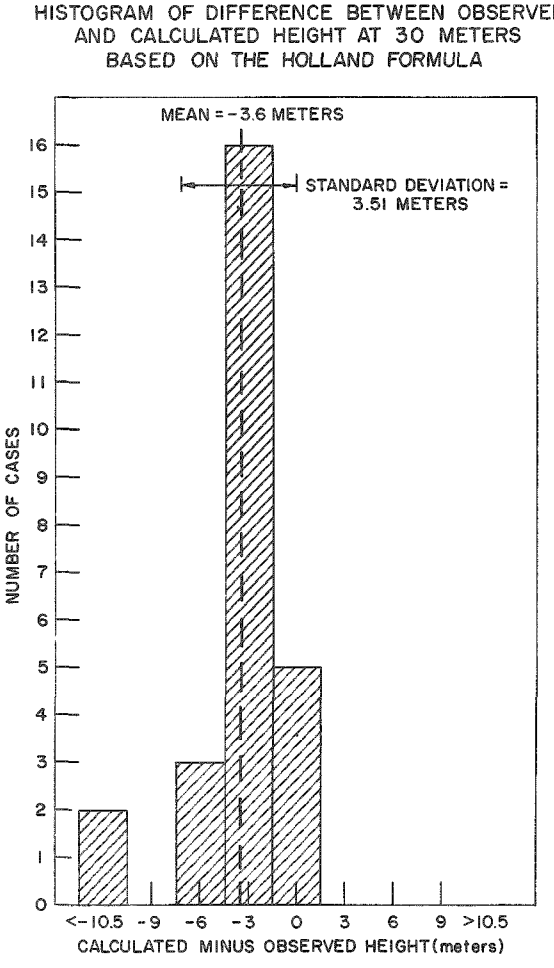

Fig. 66

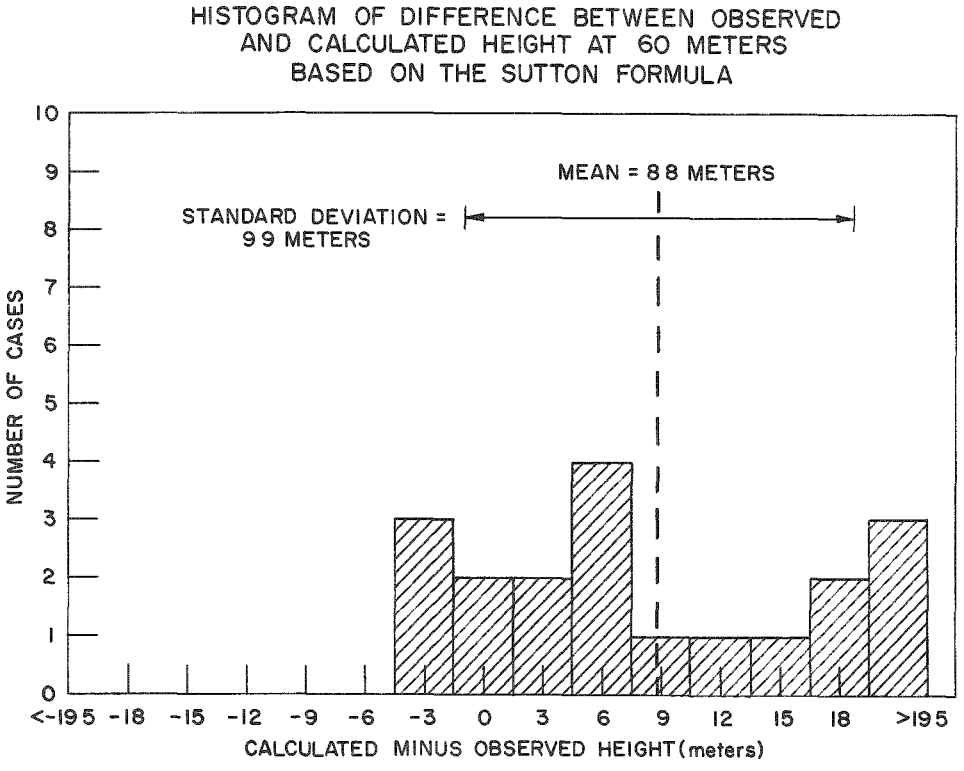

Fig. 67

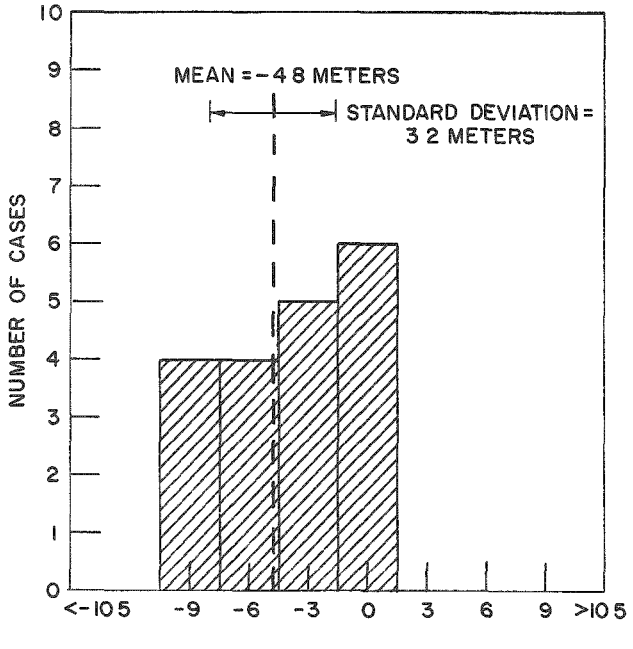

Fig. 68

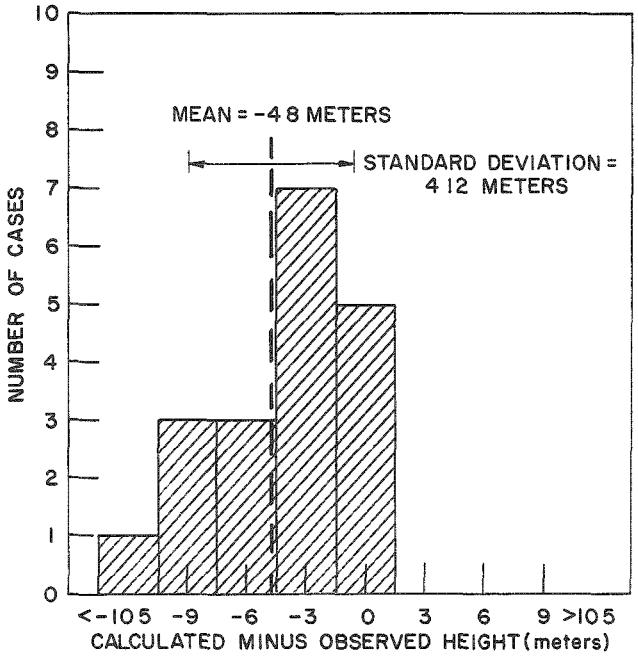

Fig. 69

next best formula, the Holland formula. Holland[2] also found the Davidson-Bryant values too low when applied to his data. Sutton's values are too high. The maximum error for any observation was least with the Davidson-Bryant data.

An examination of the scatter diagrams discloses that during runs made under unstable conditions, the correlation between computed and observed heights is smaller than in those made under stable conditions. A possible explanation may be that the unstable runs were made under higher wind conditions. This point bears further investigation requiring additional data.

The scatter of all of the points is, no doubt, due in part to the brevity of the 4-minute observing period. Evidence for this is the variation in plume height in consecutive runs only a few minutes apart. Eddies with time scales greater than 4 minutes would influence the plume height more than some of the variables that appear in the formulas.

VIII. Conclusions

At both 30 and 60 meters the Davidson-Bryant formula provides the best fit of the data, but the values average too low (2.4 meters at 30 meters and 3.8 meters at 60 meters). The Sutton values show the greatest discrepancies and are too high.

The forecast of the plume rise may be improved through the use of the following regression equations:

For 30 meters

$$\Delta h = \frac{3.49\, v_s d + 9.32 \times 10^{-5} Q}{u} + 0.25 \qquad \text{(Holland)} \qquad (9)$$

$$\Delta h = 1.02 d \left(\frac{v_s}{u}\right)^{1.4} \left(1 + \frac{\Delta T}{T}\right) + 2.28 \qquad \text{(Davidson-Bryant)} \qquad (10)$$

For 60 meters

$$h = \frac{3.81\, v_s d + 10.16 \times 10^{-5} Q}{u} + 1.37 \qquad \text{(Holland)} \qquad (11)$$

$$\Delta h = 1.09 d \left(\frac{v_s}{u}\right)^{1.4} \left(1 + \frac{\Delta T}{T}\right) + 3.56 \qquad \text{(Davidson-Bryant)} \qquad (12)$$

Since these formulas are based on measurements made during a particular range of meteorological conditions and stack parameters, one cannot apply them to all stacks under all conditions. For example, the Meteorology Experimental Stack has an inside diameter of 1.46 feet and an

outside diameter of 1.5 feet. It ,therefore,cannot be recommended that the formulas be applied to stacks having a significantly different diameter, e.g. 10 feet.

Since the standard error of estimate for the Holland and Davidson-Bryant regression formulas are not significantly different, either equation will provide an equally good forecast.

The assistance of Hugh G. Daubek and Janet Park in drawing the graphs and making computations is gratefully acknowledged.

References

1. Sutton, O. G. The Dispersion of Hot Gases in the Atmosphere. J. Meteorol. 7 (5) 307-310 (1950).

2. Holland, J. Z. A Meteorological Survey of the Oak Ridge Area, U.S. Atomic Energy Commission Report ORO-99 (1953).

3. Rupp, A. F., Beall, S. E., Bornwasser, L. P., and Johnson, D. F. Dilution of Stack Gases in Cross Winds. U. S. Atomic Energy Commission Report, AECD-1811, (1948).

4. Davidson, W. F. The Dispersion and Spreading of Gases and Dust from Chimneys, Trans. Conf. on Industrial Wastes, 14 Ann. Meeting, Ind. Hygiene Found. Am. Nov. 18, 1949. pp. 38-55.

5. Bosanquet, C. H., Casey, W. F. and Halton, E. M. Dust Deposition from Chimney Stacks. Proc. Inst. Mech. Eng. 162 355-367 (1950).

6. Priestly, C. H. B. A Working Theory of the Bent-Over Plume of Hot Gas. Quart. J. Roy. Meteorol. Soc. 81 139-43, 1956.

7. Clark, R. D. M. Photographic Techniques for Measuring Diffusion Parameters. Fourth AEC Air Cleaning Conf. Held at Argonne National Laboratory. U. S. Atomic Energy Commission Report, TID-7513, Pt. I (1955) pp. 186-200.

8. Moses, H. and Willett, J.H. Five-Year Climatological Summary, July 1949-June 1954, Argonne National Laboratory, DuPage County, Illinois, ANL-5592 (1957).

9. Meteorology and Atomic Energy. U. S. Weather Bureau. U. S. Atomic Energy Commission Report, AECU-3066 (July 1955).

10. Bryant, L. W. The Effects of Velocity and Temperature of Discharge on Shape of Smoke Plumes from a Funnel or Chimney in a Wind Tunnel. National Physical Laboratory (Great Britain), 1949.

PUBLICATIONS

January - July 1960

Bowe, J. C. Drift Velocity of Electrons in Nitrogen, Helium, Neon, Argon, Krypton and Xenon. Phys. Rev. 117 1411-1415 (1960).

Bowe, J. C. Transport Collision Cross-Sections from Electron-Drift-Velocity Data. Phys. Rev. 117 1416-1420 (1960).

Bowe, J. C. Transport Cross-Sections from Electron Mobility Data in the Noble Gases and in Nitrogen. Bull. Am. Phys. Soc. 5(2): 122 (1960). Abstract.

Brues, A. M., H. Auerbach and L. D. Marinelli. Assessment of Fallout Hazards. Science 131 230 (1960). Letter to Editor.

Finkel, A. J., C. E. Miller and J. B. Corcoran. Retention of Continuously Ingested Radium by Mice. Radiation Research 12 434 (1960). Abstract.

Frenzen, P. Turbulent Diffusion. (Mimeographed notes.) Item No. 37 in the Forecasting Seminar Collection, Headquarters 8th Weather Group, AWS (MATS) USAF, Randolph Air Force Base, Texas (1960).

Gill, G. C., H. Moses, and M. E. Smith. Summary of Instrumentation Clinic. Bull. Am. Meteorol. Soc. 41 (3) 154-155 (1960).

Gill, G. C., H. Moses and M. E. Smith. Current Thinking on Meterological Instrumentation for Use in Air Pollution Problems. Proc. 53rd Ann. Meet. of Air Pollution Assoc. (May 1960).

Lucas, H. F., and D. P. Krause. Preliminary Survey of Radium-226 and Radium-228 (MsThI) Contents of Drinking Water. Radiology 74 114 (1960). Abstract.

Lucas, H. F., and C. E. Miller. The Effect of Body Burden on the Radon Partition Ratio in Humans. Radiation Research 12 453 (1960). Abstract.

May, Harold and L. D. Marinelli. Factors Determining the Ultimate Detection Sensitivity of Gamma Scintillation Spectrometry. Radiation Research 12 455 (1960). Abstract.

Miller, C. E. Low Intensity Spectrometry of the Gamma Radiation Emitted by Human Beings. Medical Physics, Vol. 3, Ed. O. Glasser. Chicago: Year Book Publishers, Inc., 1960 pp. 488-492.

Moses, H., A. F. Stehney and H. F. Lucas, Jr. The Effect of Meteorological Variables upon the Vertical and Temporal Distributions of Atmospheric Radon. J. Geophy. Research 65(4) 1223-1238 (1960).

PUBLICATIONS (Cont'd.)

Platzman, R. L. Total Ionization in Gases by High-Energy Particles: An Appraisal of our Understanding. Proceedings of the Conference on Penetration of Charged Particles in Matter. National Research Council Publication 752, Washington, D. C., 1960.

Rowland, R. E. Late Observations of the Distribution of Radium in the Human Skeleton. Symposium on Radioisotopes in the Biosphere, Univ. Minnesota, Oct. 19-23, 1959, Eds. R. S. Caldecott and L. A. Snyder, Minneapolis: University of Minnesota Press, 1960. pp. 339-353.

Rowland, R. E. Quantitative Microradiography of Bone. Medical Physics, Vol. 3 Ed., O. Glasser. Chicago: Year Book Publishers, Inc., 1960. pp. 525-528.

Stehney, A. F. Naturally Occurring Radioisotopes in Man. Symposium on Radioisotopes in the Biosphere, Univ. Minnesota, Oct. 19-23, 1959. Eds. R. S. Caldecott and L. A. Snyder. Minneapolis: University of Minnesota Press, 1960. pp. 366-381.

PAPERS TO BE PUBLISHED

Anderson, W. R., and I. B. Berlman. Light Flux from a Cylindrical Distributed Source. J. Opt. Soc.

Anderson, W. R., and I. B. Berlman A Study of the Light Output from a Cell Containing a Radiation-Damaged Scintillating Solution. Radiation Research.

Berlman, I. B., R Grismore and B. Oltman. An Improved "Twin" Scintillation Fast Neutron Detector. Rev. Sci. Instr.

Berlman, I. B. Luminescence in a Scintillation Solution Excited by Alpha and Beta Particles and Related Studies in Quenching. J. Chem. Phys.

Berlman, I. B. Energy Transfer in a Solution of PPO in Xylene. J. Chem. Phys.

Gill, G. C., H. Moses and M. E. Smith. Current Thinking on Meteorological Instrumentation for Use in Air Pollution Problems. J. Air Pollution Control Assoc and Proceedings of the Air Pollution Control Assoc.

Grismore, R. Radiation. The American People's Encyclopedia Year Book for 1960. Vol. 1.

Gustafson, P. F.* Fallout Transport as Deduced from Measurement of Gamma-Emitting Radioactivity in Air. Health Physics.

Gustafson, P. F.,* and M. A. Kerrigan.* Re-Evaluation of the Radiation Dose due to Fallout. Radiology (Abstract).

Gustafson, P. F.* Assessment of Radiation Dose due to Fallout. Radiology

Gustafson, P. F.,* S. S. Brar* and M. A. Kerrigan.* Variation of Fallout Radioactivity in Soil and Air. Radiation Research (Abstract)

Marinelli, L. D., C. E. Miller, H. A. May and J. E. Rose. Low Level Gamma-Ray Spectrometry: Experimental Requirements and Biomedical Applications. Advances in Biological and Medical Physics, Vol. 8, Eds. C. A. Tobias and J. H. Lawrence. New York: Academic Press.

Marinelli, L. D., C. E. Miller, H. A. May and J. E. Rose. The Use of Low Level Gamma Scintillation Spectrometry in the Measurements of Activity in Humans. Proc. Symposium on Radioactivity in Man, Whole Body Counting and Effects of Internal Gamma Ray Emitting Radioisotopes, Vanderbilt University, Nashville, Tenn., April 18-19, 1960.

---

*Division of Biological and Medical Research

PAPERS TO BE PUBLISHED (Cont'd.)

Marshall, J. H. Radioactive Hotspots, Bone Growth, and Bone Cancer: Self-Burial of Calcium-Like Hotspots. Proc. Council International Organization Medical Sciences Meeting, Princeton, New Jersey, Aug. 28-Sept. 3, 1960.

Marshall, J. H. and M. P. Finkel. Comparison of Microdosimetry and Tumour Production for Ca^{45}, Sr^{90}, and Ra^{226} in Mice. International Atomic Energy Report on Oxford Conference on Relation of Radiation Damage to Radiation Dose in Bone, Oxford, England, April 1960.

May H. A., and L. D. Marinelli. Factors Determining the Ultimate Detection Sensitivity of Gamma Scintillation Spectrometry. Proc. Total Absorption Gama Ray Spectrometry Symposium, Gatlinburg, Tenn., May 10-11, 1960.

May, H. A. Supplement to the Use of Low Level Gamma Scintillation Spectrometry in the Measurements of Activity in Humans, by L. D. Marinelli et al. Proc. Symposium on Radioactivity in Man, Whole Body Counting and Effects of Internal Gamma Ray Emitting Radioisotopes, Vanderbilt University, Nashville, Tenn., April 18-19, 1960.

Miller, C. E. Identification, Location and Measurement of Radioactivity in the Human Body. Proc. Symposium on Radioactivity in Man, Whole Body Counting and Effects of Internal Gamma Ray Emitting Radioisotopes. Vanderbilt University, Nashville, Tenn., April 18-19, 1960. Abstract

Moses, H., and H. Daubek. Errors in Wind Measurements Associated with Tower-Mounted Anemometers. Bull. Am. Meteorol. Soc.

Platzman, R. L. Probabilité d'ionisation par transfert d'énergie d'atomes excites a des molécules. J. phys. radium.

Platzman, R. L. Total Ionization in Gases by High-Energy Particles. Int. J. Applied Radiation and Isotopes.

Rowland, R. E. The Deposition and Removal of Radium in Bone by a Long-Term Exchange Process. Clinical Orthopedics.

Rowland, R. E. Radiation Damage and Radiation Dosimetry in Human Bone Containing Ra^{226}. Report on Conf. Relation of Radiation Damage to Radiation Dose in Bone, Oxford, England, April 10-14, 1960. Abstract

Wasko, P., and H. Moses. Photogrammetric Technique for Studying Atmospheric Diffusion. Photogrammetric Engr.